



UNIUNEA EUROPEANĂ



GUVERNUL ROMÂNIEI
MINISTERUL MUNCII, FAMILIEI,
PROTECȚIEI SOCIALE ȘI
PERSOANELOR VĂRSTNICE
AMPOSDRU



Fondul Social European
POSDRU 2007-2013



Instrumente Structurale
2007-2013



Study of transverse momentum spectra of charged hadrons at high multiplicities and azimuthally isotropic events in p-p collisions at 7 TeV using the ALICE experimental setup

Andrei Ionuț Herghelegiu

Scientific advisor: Prof. Dr. Mihai Petrovici

Thesis submitted for the degree of
Doctor of Philosophy



University of Bucharest
Romania
2013

Contents

1	Introduction	1
2	Theoretical overview	5
2.1	Proton-proton collisions	6
2.2	Multi-parton interactions	7
2.3	Relativistic hydrodynamics	11
2.4	Relativistic thermodynamics	11
2.5	Soft physics observables	11
2.6	Collective phenomena in high energy collisions	14
2.7	Blast Wave models	15
2.7.1	Cooper-Frye formalism	16
2.7.2	Boltzmann-Gibbs blast-wave	16
2.7.3	Tsallis blast wave	16
2.8	Model predictions	17
2.8.1	EPOS	18
2.8.2	Pythia 8	18
2.9	Discussion	19
3	Experimental setup	21
3.1	The Large Hadron Collider	21
3.2	ALICE experimental setup	22
3.2.1	Central Barrel Detectors	23
3.2.2	Inner Tracking System	23
3.2.3	Time Projection Chamber	25
3.3	Analysis and computational framework	26
3.3.1	Virtual Monte Carlo	28
3.3.2	Event generators	28
3.3.3	GEANT	29
3.3.4	Event reconstruction	30
4	Analysis details	31
4.1	Data selection	31
4.1.1	Period selection	31
4.1.2	Event Selection	33
4.1.3	Trigger selection	33
4.1.4	Vertex selection	33
4.1.5	Pileup rejection	34

4.1.6	Track selection	34
4.2	Multiplicity estimation	36
4.2.1	Global Tracks multiplicity	37
4.2.2	Combined multiplicity estimator	37
5	Event shape observables	41
5.1	Directivity	42
5.2	Thrust	43
5.3	Sphericity	44
5.4	Recoil	46
5.5	Fox-Wolfram moments	46
5.5.1	General properties of Fox-Wolfram moments	47
5.5.2	Modified Fox-Wolfram moments	47
5.5.3	Correlation between FWM and other Event Shape Observables	48
5.6	Examples based on Pythia	48
5.7	Comparison with data	51
5.8	Study of multiplicity - event shape correlation	51
5.8.1	Comparison with Pythia	52
5.8.2	Multiplicity dependence of the Fox-Wolfram moments distri- butions	53
5.8.3	Trigger dependence	54
5.9	Event topology selection performance	57
5.10	Evaluation of the event shape selection performance for the modified Fox-Wolfram moments	58
5.10.1	Two particle correlations	58
5.11	Transverse momentum spectra dependence on the event shape selection	61
5.11.1	Isotropic events in Pythia	77
5.11.2	Multiple jets	79
5.12	Discussion	82
6	Efficiency corrections	85
6.1	Trigger efficiency	85
6.2	Vertex efficiency	85
6.3	Acceptance and tracking efficiency corrections	86
6.3.1	Multiplicity dependence	86
6.3.2	High multiplicity bins efficiency	90
6.3.3	Efficiency dependence on event shape observables	90
6.4	Feed down correction	99
6.4.1	Distance of closest approach studies	99
6.5	Systematic uncertainties	102
6.5.1	Acceptance and tracking efficiency	102
6.5.2	Fake tracks and multiple track reconstruction	103
6.5.3	Feed-down correction uncertainty	104

7	Results	107
7.1	Transverse momentum spectra	107
7.1.1	Minimum Bias spectra	107
7.1.2	Transverse momentum spectra - multiplicity dependence . . .	109
7.2	Event Shape selected spectra	109
7.2.1	Minimum Bias trigger	109
7.2.2	High Multiplicity trigger	110
7.2.3	Mean transverse momentum - multiplicity dependence	115
7.3	Towards isotropic events	118
8	Conclusions and perspectives	123
	Bibliography	127
9	Acknowledgements	143
A	ALICE coordinate system	145

In the memory of Tiberiu Ţugui.

*“Better than a thousand days of diligent study
is one day with a great teacher.”
Japanese proverb*

Chapter 1

Introduction

High energy physics offers the possibility to study strongly interacting matter in extreme temperature and barionic density conditions similar to those found in the very early Universe or in the neutron stars. Studying the hot dense matter generated in hadron colliders is the best method to study in the laboratory the Equation Of State of the strongly interacting matter. The Large Hadron Collider, at CERN, is the man-made particle accelerator with the highest energy per nucleon presently available. Particle accelerators allow us to have a glimpse of the early universe. The high temperatures reached in heavy ion collisions at LHC are similar to those characterizing the universe only microseconds after the Big Bang as shown in Figure 1.1.

The work presented in this thesis focuses on data obtained with the ALICE experimental setup, one of the four major experiments at LHC, at 7 TeV. ALICE is dedicated to heavy ion collisions with high particle multiplicities and low interaction rates. The Inner Tracking System and the Time Projection Chamber of the experiment allow the study in the low transverse momentum range ($\gtrsim 0.15$ GeV/c). Accessing this low p_T region enables a more accurate study of the spectra shape and evaluation of the mean transverse momentum based on data rather than on theoretical extrapolations.

Theoretical predictions and experimental results indicate that at high temperatures, as found in the systems formed during hadronic collisions, the deconfinement of hadronic matter takes place. In this deconfined state, partons may develop a hydrodynamical behaviour leading to collective phenomena. The system evolution in the heavy ion collisions is well described by hydrodynamic models [Huovinen2006], [Gale2013]. Later developments in the hydrodynamic approach take into account the non-uniformity of the energy density distribution in the transverse plane generated by the nucleon distribution in the colliding nuclei. In order to better understand the hot spot (high energy density region) dynamical evolution, the proton-proton collisions are studied. The chapter dedicated to the theoretical motivation presents several arguments why the high multiplicity azimuthally isotropic proton-proton events are the focus of the present thesis.

A transition from hadronic matter to a deconfined state was suggested by Hagedorn [Hagedorn1971]. Quantum Chromo-Dynamics - QCD - predicts a transition from barionic to a deconfined phase at a critical temperature of ≈ 170 MeV. While

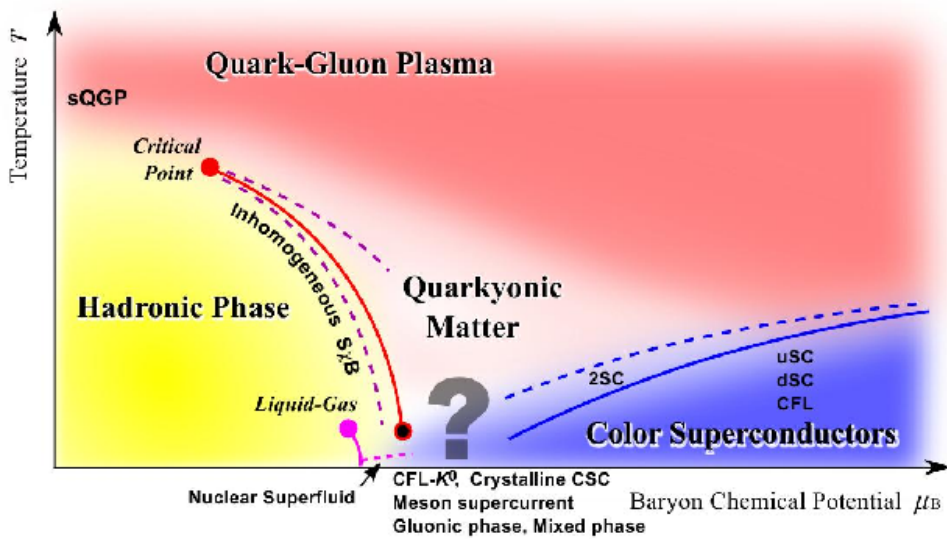


Figure 1.1: Phase space diagram of strongly interacting matter.

the experimental conditions for obtaining a deconfined state in high energy physics are available, the properties of the new phase of matter are not yet understood.

Glauber simulations show that, in a heavy ion collision, hot spots with high energy densities are created. Understanding the processes involved in proton-proton collisions will help clarify the more complicated phenomena in heavy ion collisions. High energy densities can be created in p-p collisions by multi-parton interactions producing events with high particle multiplicities. Such events are comparable with the corona region of the heavy ion collisions where the incoming partons from the two colliding nuclei have a large probability to suffer an interaction. Therefore, collective phenomena specific to the heavy ion collisions are more probable to be found in high multiplicity p-p events.

One method used for collectivity studies relies on the transverse momentum spectra. The shape and the mean value of this spectra could indicate a common expansion velocity of the deconfined matter. Such an expansion could be falsely exhibited by the presence of hard jets. Therefore, selecting events without jets is mandatory in collectivity studies. The analysis presented in this thesis investigates the transverse momentum spectra of charged particles at high multiplicities for events obtained with the ALICE experimental setup at CERN. The transverse momentum spectra have two regions, traditionally called “soft” and “hard”. The present analysis focuses on soft phenomena. Therefore, the first step was to evaluate if the two components could be separated by using several event shapes observables. The hard component is generally represented by jets which are emissions of high energy particles confined in a narrow cone and is well described by the perturbative Quantum Chromo-Dynamics. On the other hand, the soft part of the spectrum is represented by low transverse momentum particles and is described phenomenologically. The two components are not clearly separated and the energy range is overlapping. In the same event one can find both hard and soft processes and the way these two components interact is not trivial to describe.

In this thesis, the soft/hard separation is done based on the jets property of being confined in a narrow region of space, while the soft particle emission is azimuthally isotropic. Several event shape observables are investigated due to their property of evaluating the energy distribution in the event. Sphericity, thrust, directivity and transverse modified Fox-Wolfram moments were the event shape observables used for event topology characterization. Their event selection capabilities are studied using Pythia 8 simulations and specially designed toy models.

The thesis is structured in eight chapters. The first chapter discusses general aspects of the physics motivation for the present studies. The second chapter describes the theoretical and previous experimental results that motivated the analysis presented in this thesis.

At the beginning of Chapter 3, a short presentation of the Large Hadron Collider is made, followed by a description of the ALICE experimental setup, focused on the detectors used in the analysis presented in this thesis. The chapter ends with a general description of the analysis framework developed for the ALICE experiment.

Chapter 4 presents the details of the analysis. Data selection criteria based on the acquisition period, trigger and pileup probability are described along with the event and track cuts used. Two multiplicity estimators are also discussed and their performance evaluated.

The first part of the analysis, focused on the event shape observables - ESO - used to separate azimuthally isotropic events, is presented in Chapter 5. In the literature there are many event shape observables defined, but not all are *a priori* well suited for the purposes of the present analysis. Sphericity, thrust, directivity and transverse modified Fox-Wolfram moments were selected and evaluated in the present thesis. Their event selection capabilities are studied as a function of the multiplicity. The selection performance is tested on real events, but also on Pythia Monte Carlo simulations and toy model events. A model was developed to investigate what is the effect of event selection based on ESO.

Chapter 6 is dedicated to the tracking and acceptance efficiency corrections due to the detectors performance and on secondary particle contaminations from weak decays and material interactions. Systematic uncertainties are considered and evaluated for the effects that have the largest contribution.

The fully corrected transverse momentum spectra are shown in Chapter 7. The invariant yield for minimum bias is presented, followed by the multiplicity dependent spectra of charged particles. The chapter ends with the p_T spectra obtained for all the event shape cuts in all the multiplicity bins. A shape variation from low to high multiplicity events is evidenced. Event shape cuts in each multiplicity bin are applied and the corresponding spectra show a clear shape difference between the events labeled as azimuthally isotropic and non-isotropic. The difference is present for all the event shape observables used. The mean transverse momentum was evaluated from the spectra using several fit functions, Levy-Tsallis, Bylinkin and Boltzmann blast wave. The minimum bias value is compared with the CMS results. Boltzmann blast wave fit results for the high multiplicity events selected as azimuthally isotropic with the Fox-Wolfram moments are compared with the results from the Pb-Pb data from ALICE in terms of freeze-out temperature and mean transverse velocity.

The chapter dedicated to the conclusions summarizes the thesis and discusses the perspectives of the analysis.

Results of the present analysis have been included in seven ALICE internal notes. The results presented in this thesis are not yet ALICE official results. Therefore, they are labeled as "This thesis".

Chapter 2

Theoretical overview

*“It is a capital mistake to theorize before one has data.
Insensibly one begins to twist fact to suit theories,
instead of theories to suit facts.”
Arthur Conan Doyle*

In this chapter the main theoretical aspects that motivated the work conducted within this thesis are presented. A comparison between the heavy ion and proton-proton collisions is made. Arguments for the study of high multiplicity events are discussed in the context of hydrodynamical formalism. The use of event shape observables is motivated by comparing the hard and soft components from experiments at lower energies.

During high energy collisions of p+p, p+A or A+A, a high energy density is produced in the initial phase, characterized by very high temperatures. The intrinsic scale of QCD being $\Lambda_{QCD} \sim 200$ MeV, it is expected that a QCD phase transition to a matter formed by freely interacting quarks and gluons takes place at such high temperatures (≈ 170 MeV, e.g. [Karsch2000]). The estimated lifetime of the de-confined bulk of matter is of the order of fm/c. The dynamics of this piece of deconfined matter, in the case of heavy ion collisions is rather successfully described by phenomenological models using the hydrodynamic approach [Huovinen2006], [Gale2013]. Applying hydrodynamic methods in proton-proton collisions is not *a priori* allowed. The system size at freeze-out is estimated from HBT studies.

In recent studies, the hydrodynamic approach takes into account the initial state non-uniformities generated by the nucleon distribution in the colliding nuclei [Schenke2012], [Alver2010]. These non-uniformities are estimated using the Glauber model. In Figure 2.1 an example of Glauber calculation for a central Au-Au collision at 200 AGeV shows large energy density variation across the transverse plane. A random distribution of hot spots rather than a homogeneous distribution within a large area seems to be characteristic of the initial state of the collision. High energy densities are found in the central region of the collision called "core". The region with low energy density is called "corona" and it corresponds mostly to nucleon-nucleon collisions where the nucleon density is relatively small. The interplay between the core and corona regions depends on the collision geometry.

Peripheral collisions have a larger contribution from the corona region while for central and ultra-central collisions the core becomes more important.

In p+p collisions at LHC energy, high multiplicity events with nearly azimuthal isotropy could originate from an initial state with similar properties as those of the hot spots mentioned above, populated in A+A or in p+A collisions. Therefore, it is rather natural to study in detail the properties and dynamics of matter produced in high multiplicity and nearly isotropic events in p+p collisions in order to understand the phenomena taking place in p+A and A+A collisions where a large piece of deconfined matter, if it is produced, is the result of dynamics and fusion of the hot spots

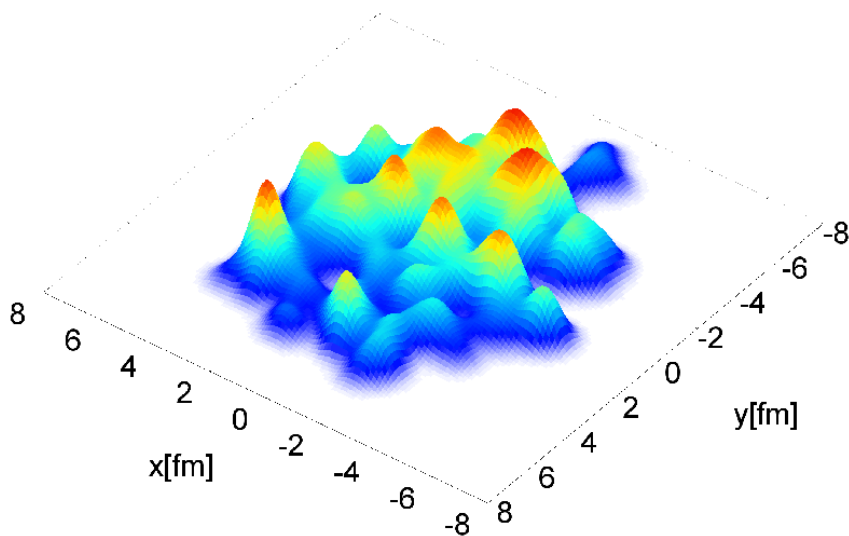


Figure 2.1: Initial energy density estimation in a central Au-Au collision. On the z axis, the energy density is represented. The calculation was performed based on the Glauber model [Schenke2012].

2.1 Proton-proton collisions

Studies of proton-proton collisions began at the Intersecting Storage Rings - IRS (CERN) [Aner1985] and continued at the Super Proton Synchrotron - SPS [Anson1986], Tevatron [Alexopoulos1993] and, more recently, at the Large Hadron Collider - LHC [LHC]. The transverse momentum spectra of the particles produced in proton-proton collisions have been studied using the statistical model introduced by Fermi in 1951 [Fermi1951]. The results from the ISR confirmed the trend of the mean transverse momentum as function of incident energy predicted by models based on statistical equilibrium [Aner1985].

The main characteristic of the mean transverse momentum for different species is the constant slope as a function of center of mass energy (\sqrt{s}). This is plotted

in Figure 2.2 for energies below 100 GeV. Later studies, performed by the E735 Collaboration for energies up to 1800 GeV, showed a clear deviation from the linear extrapolation based on previous results from ISR (the last four points on Figure 2.2). The slope of the mean transverse momentum was found to be particle dependent and clearly deviating from the trend at lower energies. Such a trend cannot be explained by using thermal models.

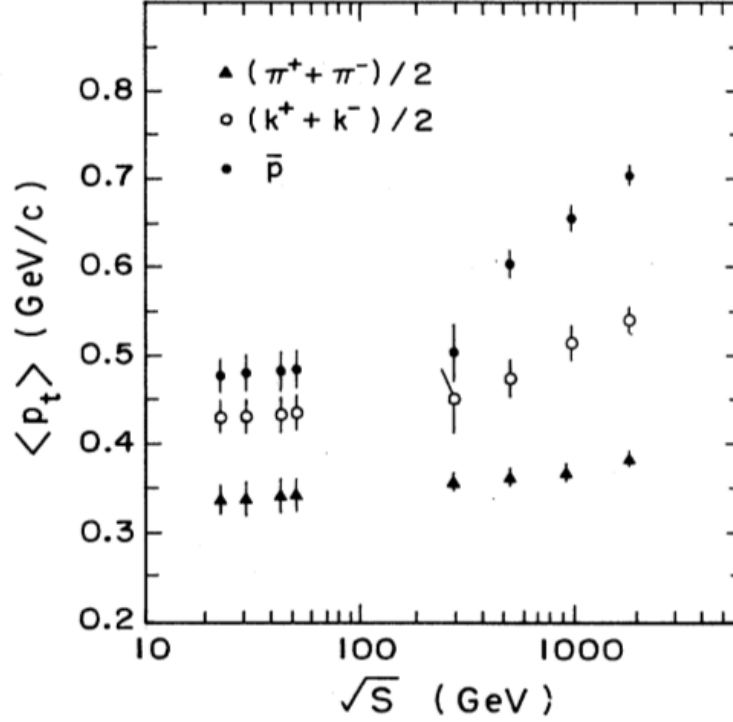


Figure 2.2: Mean transverse momentum as a function of \sqrt{s} . The results at 300, 450, 1000 and 1800 GeV are reported by E735 Collaboration [Alexopoulos1993].

Previous collectivity studies in p-p collisions (see Figure 2.3) demonstrated that the temperature remains almost constant while the transverse velocity increases with the center of mass energy [Kagiyama1989].

2.2 Multi-parton interactions

In hadron-hadron collisions, multiple (independent) pairs of constituent partons may interact. This is called multi-parton interactions - MPI [Bartalini2011]. A schematic view of a double parton interaction is depicted in Figure 2.4.

Since each parton carries a fraction of the incident energy, MPI will generate higher energy densities in the colliding region. Therefore, more particles can be produced during the process. This allows the development of MPI studies based on multiplicity distribution [Walker2004].

In heavy ion collisions, MPI are highly probable, especially in the region with high nucleon density. The reason is that in a high partonic density medium like

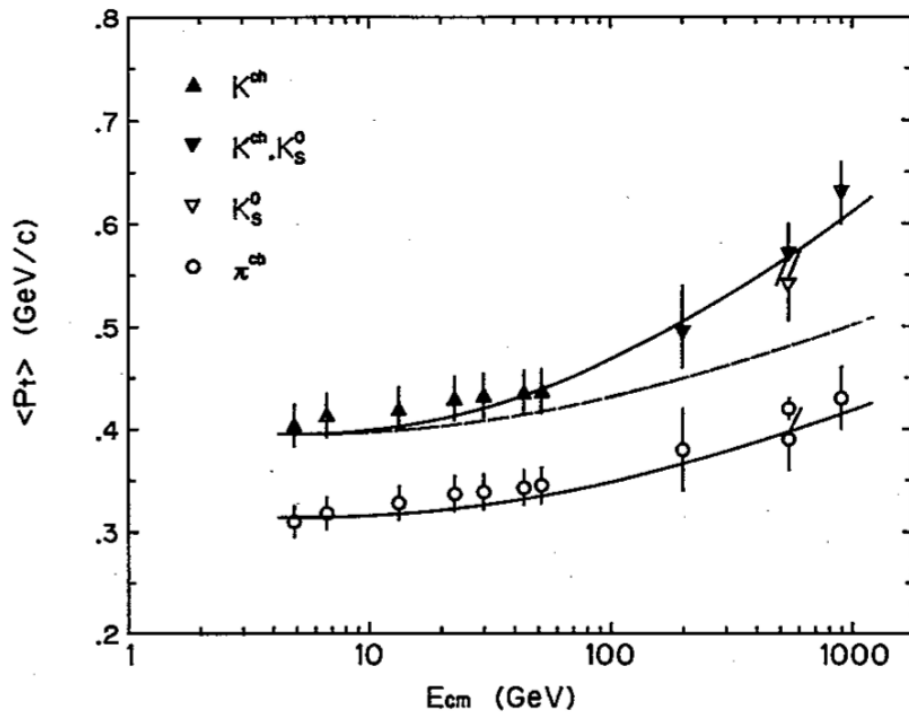


Figure 2.3: Mean transverse momentum as a function of incident energy for pions (circles) and kaons (triangles). Calculations for solid lines include collective expansion. Dashed line is the theoretical prediction without transverse velocity [Kagiyama1989].

the one found in heavy ion collisions, each parton has a better chance to encounter another parton from the other nuclei. The Glauber model [Glauber1959] [Broniowski2009] predicts the existence of a "core" region with a large number of participating nucleons. In this region it is reasonable to assume that most of the partons from the colliding nucleons are participants in the sense that partons from the nucleons of one nucleus interact with partons from the nucleons of the other nucleus.

Multi parton interactions in the core region of heavy ion collisions generate large number of particles. This is an indication that the comparison of heavy ion and proton-proton data must be done using the results obtained for proton-proton events with large number of produced particles.

Estimations for multiple partonic interactions are plotted in Figure 2.5 as a function of incident energy. The contribution of double and triple parton-parton interaction increases with the \sqrt{s} . Therefore, many parton-parton scatterings are highly probable to occur in each event at LHC.

Multi-parton interactions create the conditions for enhanced particle production. This allows the development of methods aiming to investigate the multi-parton interactions using the multiplicity distribution [Walker2004].

The mean free path of partons inside the deconfined matter is essential in defining the properties of the matter created in a collision. Both thermal and hydrodynamical descriptions used in high energy physics are conditioned by the number of collisions suffered by the system constituents. This number depends on the value of the mean free path of the partons: $\lambda = 1/\rho\sigma$, where ρ is the medium density and σ is the total cross section of the parton-medium interaction. Phenomenological models were able to reproduce flow observables at RHIC energy estimate a mean free path (λ) in central collisions of the order of 0.3 - 0.35 fm [Lacey2009].

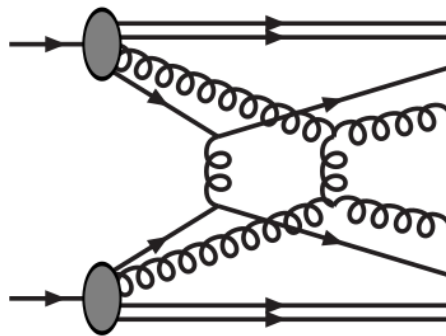


Figure 2.4: Schematic view of a double parton-parton interaction. Picture from [Sjöstrand2004].

The mean free path depends also on the density of the medium. The highest medium density is achieved in high multiplicity events. Under the assumption that Bjorken's formula for the estimation of the energy density can be used for proton-proton collisions, one can evaluate the energy density as a function of multiplicity

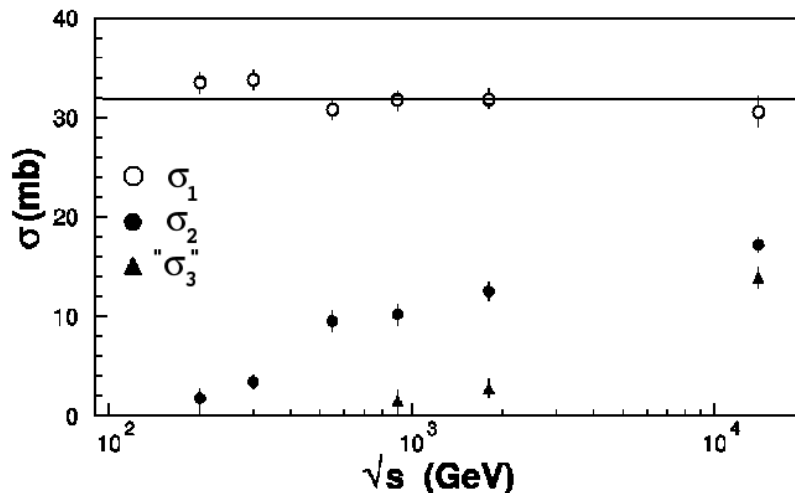


Figure 2.5: Multi-parton cross section as a function of collision energy. σ_1 , σ_2 and σ_3 represent the cross section for one, two and three multiparton interactions. Picture from [Walker2004]. Quality of the picture has been enhanced for clarity.

[Bjorken1983]:

$$\epsilon_{Bj} = \frac{1}{\tau A} \frac{dE_T}{dy} = \frac{1}{\tau A} \frac{dN}{dy} \langle m_T \rangle \quad (2.1)$$

where, τ is the formation time, estimated at less than $1fm/c$. E_T and m_T are the transverse energy and mass, respectively. dN/dy is the multiplicity per unit of rapidity. In the geometrical approach, A is considered equal to the inelastic cross section.

The multiplicity per unit rapidity in high multiplicity events can reach values up to ≈ 50 (for events with 80 particles in $|\eta| < 0.8$).

The value obtained for $\epsilon_{Bj} \cdot \tau$ in high multiplicity events is similar with its value for Pb+Pb central collisions at 2.76 TeV.

At high multiplicities, the mean transverse momentum is higher than for low multiplicity events (see Figure 2.7). This indicates that additional energy is pumped into the system during the collision where more particles are produced. Therefore, in high multiplicity events, the number of collisions suffered by the partonic constituents could be sufficiently high for thermal equilibrium of highly compressed de-confined matter to be reached and a hydrodynamical description of its expansion becomes applicable. These arguments motivated the investigation of collective phenomena in high multiplicity proton-proton events.

2.3 Relativistic hydrodynamics

The hydrodynamical approach in heavy ion collisions was first suggested by Landau [Landau1953], [Landau1955]. Hydrodynamics can be applied in thermalized systems where the mean free path is relatively small in comparison with the size of the system. The constituents must suffer a high number of collisions while inside the considered region. The probability to find a thermalized system in p-p collisions is higher for the events with high density of partonic constituents. These events will produce a high number of particles detected by the experiments. Therefore, high multiplicity events are the best candidate for studies of collective type phenomena in proton-proton collisions at LHC.

The necessary conditions for hydrodynamic evolution are reached only if the constituents suffer re-scattering processes after the initial multi-parton interactions. Without re-scatterings, the MPI are basically reduced to two (or three) independent single partonic interactions. Until now, there is no complete theoretical description able to estimate the number of re-scatterings during the p-p collisions.

2.4 Relativistic thermodynamics

Thermalization requires a relatively high number of collisions between the constituents. The partons from the deconfined matter created in proton-proton collisions may suffer several rescatterings before hadronization takes place. After hadronization, particles interactions are inelastic, and the particle ratios are modified. The moment when inelastic collisions stop is called chemical freeze-out. The kinematic (thermal) freeze-out occurs when the elastic interactions between the hadrons stop. This is what is measured by detectors.

A thermalized source at rest radiates particles with the following invariant momentum distribution:

$$E \frac{d^3 N}{dp^3} = \frac{dN}{p_T dp_T d\phi dy} = \frac{gV}{(2\pi)^3} E e^{-(E-\mu)/T} \quad (2.2)$$

The mean transverse momentum is given by [Hagedorn1971]:

$$\langle p_T \rangle = \sqrt{\pi m T / 2} \frac{K_{5/2}(m/T)}{K_2(m/T)} \quad (2.3)$$

2.5 Soft physics observables

Parton-parton interactions are usually labeled as "hard" or "soft" depending on the momentum transfer [Ansari1987], [Sjöstrand1987], [Wang1989]. The separation between the two classes of events is not rigorously defined and the boundary is specific to each analysis. There is no golden rule describing the recipe for a clear soft/hard separation. The general used definition is that low transverse momentum particles are specific to the "soft" region. The soft region is regarded as the thermal component of the spectrum.

The hard component is represented by the high energy parton-parton scatterings. The signature of hard processes is the presence of jets (e.g. [Butterworth2012]). Jets represent high energy particle emissions confined in a narrow region in the (η, φ) plane. The soft component can also be defined as "everything that is not part of a jet". This definition was introduced by the CDF Collaboration [Affolder2002] under the label of "underlying event". An approach based on exclusion of jets is more or less arbitrary, since it depends on the used jet finding algorithm.

In this thesis, a different approach, based on the event shape observables (ESO), was tested. The event shape observables were introduced at much lower energies [Hanson1975] and are still used at LHC, at energies more than three orders of magnitude higher. The event shape observables have been used extensively for model tuning [Sjöstrand2008]. If proven to be efficient in hard/soft separation, the event shape observables could allow a consistent comparison between experiments operating at different energies.

Transverse momentum spectra of the soft and hard events separated using a cluster finding algorithm [Acosta2002] reported by the CDF collaboration are displayed in Figure 2.6. The results are obtained using proton-proton data at 630 GeV and 1800 GeV. The spectra in the two classes show different shapes for both energies analyzed.

The mean transverse momentum as a function of the number of charged particles is plotted in Figure 2.7. A multiplicity scaling can be observed only for the soft component. Mixing the two classes will affect the shape of the reconstructed spectra and the value of mean transverse momentum extracted from the spectra. Both these observables are sensible to the underlying dynamics of the colliding system.

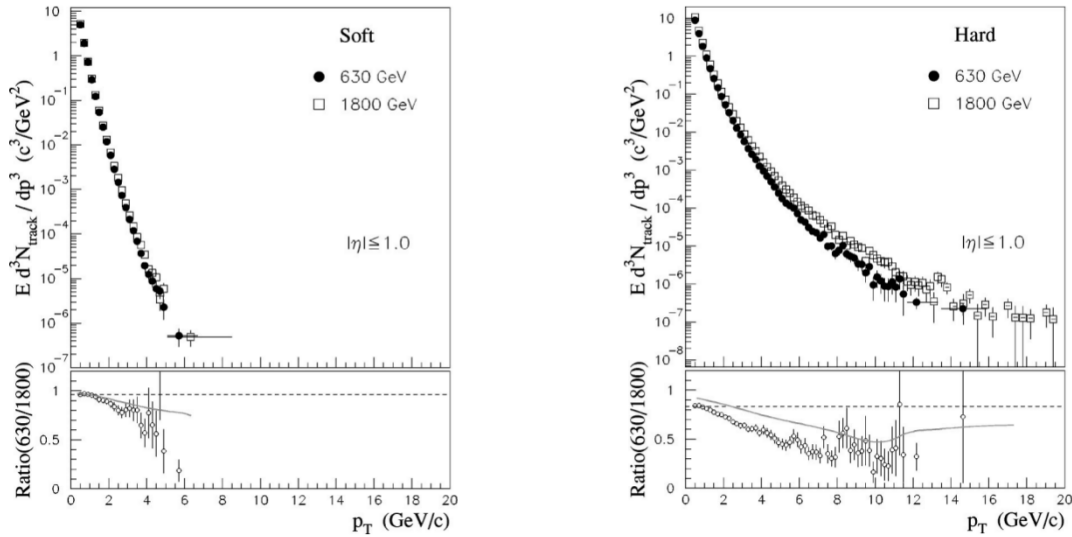


Figure 2.6: Transverse momentum in "soft" (left panel) and "hard" (right panel) events obtained by the CDF collaboration [Acosta2002]. Two energies are shown: 630GeV (full symbols) and 1800GeV (empty symbols).

There is no clear separation of the two regions and definitions are rather adapted to the particular case of each analysis. While low p_T values are regarded as "soft" and

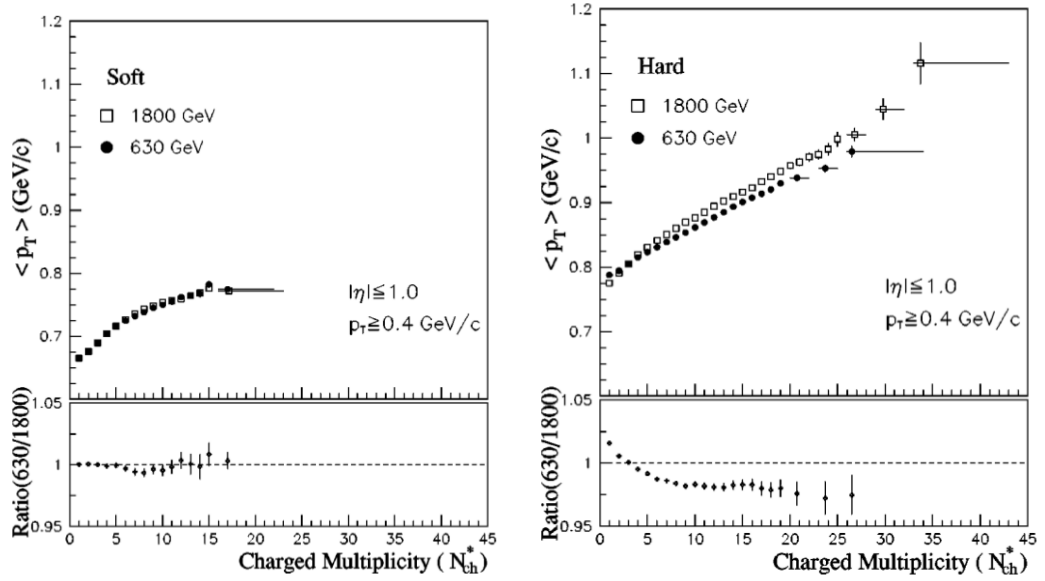


Figure 2.7: Mean transverse momentum in "soft" (left panel) and "hard" (right panel) events obtained by the CDF collaboration [Acosta2002] at 630 GeV (full symbols) and 1800 GeV (empty symbols). Multiplicity scaling can be observed only for the soft events.

high momenta is characteristic to the "hard" component, there is also an overlapping region between the two. One approach used for soft region separation is a cut in the highest transverse momentum of each event. Typically, the value used is $p_T^{cut} < 2$ GeV/c [ALICE2012b]. A low p_T cut eliminates all the high energy jets but it may also reject events with particle momenta allowed by the thermal distribution characteristic to the soft region.

The hard p_T region is well described by perturbative QCD (review in [Sternan2004]). On the other hand, no theory is able to describe the soft region microscopically. A phenomenological approach is more suitable in this case.

In this thesis, a rather different approach was used to discriminate the soft region. It is based on the jets (and minijets) property of being rather well collimated in a narrow region on space [Hanson1975]. On the other hand, soft particle emission in high multiplicity events, if they originate from a thermal equilibrated source, is azimuthally isotropic, since it does not have a preferential direction for the generated particles.

The azimuthal anisotropy property, that led to the discovery of the jets [Hanson1975], is used in this analysis to reject jetty events. The isotropy of the event can be estimated by using event shape observables. The reason why ESO were chosen to be investigated in this thesis is that they reflect the global characteristics of the collision.

All the jet finding algorithms use a set of parameters tuned for each analysis and depend on the incident energy [Cacciari2011]. The algorithm used by the CDF [Acosta2002] was initially implemented in this analysis for a direct comparison. It was found that it is not well adapted to the physics recorded by the ALICE

experiment. At sufficiently high multiplicities, all the events were labeled as hard due to the very low threshold in the cone finding algorithm. Therefore, the analysis focused on the selection capabilities of several event shape observables that were used for a broad energy range.

Furthermore, soft and hard components may also interact. This is an argument in favor of eliminating the events with jets from the data sample instead of analyzing the underlying event.

2.6 Collective phenomena in high energy collisions

In a broad definition, collectivity is defined as a space-momentum correlation between collision products. In this sense, one can argue that jets may also be labeled as collective since a large number of particles are emitted preferentially in a small region of space. As a spatial collectivity, jets can mimic elliptic flow in heavy ion collisions. They can also introduce a boost in the transverse momentum spectra in this way producing a p_T spectra like a thermal distribution on top of a collective motion. Jets are not, in general, considered as collective phenomena because collectivity is regarded as characteristic to the soft region. Therefore, jets contribution have to be eliminated in collectivity studies. The present analysis investigates how jets can be eliminated from the data sample with the help of event shape observables and their values characteristic for events close to azimuthal isotropy.

The definition of collectivity can also be formulated in a hydrodynamical context. If the thermalized region where particles are emitted from is at rest, the particle p_T distribution will be described by the thermal models. If that region expands with a global velocity, all particle velocities will be shifted accordingly. In the high energy physics, the common velocity originates in the expansion process. This is called "flow" in analogy with the classical hydrodynamic case. Particles in a liquid have a thermal velocity distribution. If the liquid is moving, the velocity distribution suffers a shift.

A common velocity boost is translated into a transverse momentum spectra, modification characteristic to each particle species, as each particle is influenced by the collective boost according to its mass. Heavier particles' momentum is more affected due to the higher mass. This differential pattern modifies the shape of the spectra and consequently, the mean transverse momentum. A similar trend can be seen in Figure 2.2.

There are indications that the matter created in heavy ion collisions expands like the early Universe according to Hubble law (i.e. $v_r \propto r$). This is a strong motivation for the study of collective phenomena in high energy physics.

Femtoscopia studies bring more arguments in favor of the multiplicity scaling [ALICE2011]. The correlation function shows a global multiplicity scaling over a CM collision energy range of almost one order of magnitude as can be seen in Figure 2.8. Here, $k_T = |\vec{p}_{T,1} + \vec{p}_{T,2}|/2$ and q is equal to $|\vec{p}_i - \vec{p}_j|$. C_0^0 , C_2^0 and C_2^2 characterize the tree-dimensional structure of the colliding region. All three show a scaling pattern as a function of multiplicity.

The same paper concludes that the system size is growing with multiplicity. This may be an indication for the collective expansion of (at least) the systems where more particles are produced [Bozek2010], [Werner2011]. Nonetheless, jets may also have a contribution [Paic2005].

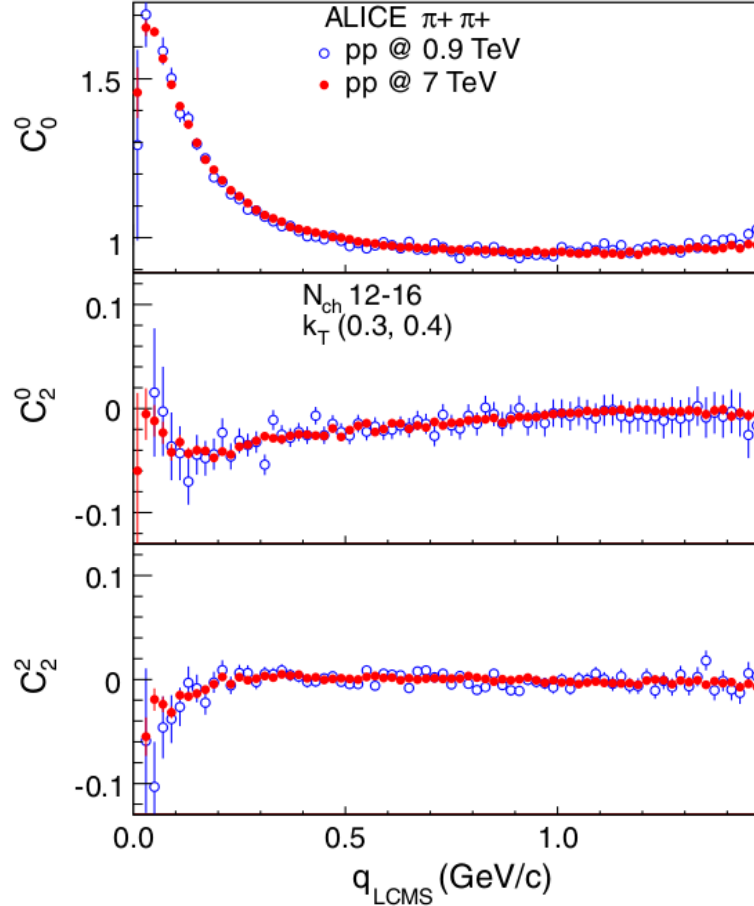


Figure 2.8: Moments of the spherical decomposition of correlation functions for events with $12 < N_{ch} < 16$ with $0.3 < k_T < 0.4$ GeV/c. Collisions at 0.9 TeV are plotted with open symbols; the closed symbols are used for 7 TeV collisions. Figure from [ALICE2011].

Models that predict collectivity signals are described in the subsection 2.8.

2.7 Blast Wave models

Particles seen in the detector are created in the hadronization process. If the region which the particles are emitted from is characterized by a common velocity as discussed in section 2.6, the spectra will be modified differently for each particle species.

2.7.1 Cooper-Frye formalism

The system created in heavy ion collisions is unstable and undergoes an expansion due to pressure gradients. As the expansion takes place, the distance between particles grows larger than the mean free path and particles stop interacting. Chemical freeze-out is the moment when inelastic interactions between particles stop and the hadronic composition remains constant. Thermal freeze-out takes place when the elastic collisions are no longer possible. Particle spectra in the hydrodynamic approach are described by the Cooper-Frye formalism introduced in [Cooper1974].

The momentum distribution of the emitted particles is given by the formula:

$$E \frac{dN}{d^3p} = C \int_{\Sigma} f(p \cdot u) p^{\mu} d\Sigma_{\mu} \quad (2.4)$$

where $d\Sigma_{\mu}$ is the element of the freeze-out hypersurface. p^{μ} and u_{μ} are the particle four-momentum and fluid four-velocity, respectively. The function f is the particle distribution function at freeze-out. It depends only on the scalar product of four-momentum p and four-velocity u . The final particle distribution found in the detector is given by the exact expression of f . Freeze-out is usually considered to take place at a critical temperature T_{fo} . Various freeze-out parameterizations are described in [Florkowski2010].

2.7.2 Boltzmann-Gibbs blast-wave

The first formula for a thermalized radially expanding system was given by Siemens and Rasmussen [Siemens1979].

$$\frac{1}{p_T} \frac{dN}{dp_T} \propto \int_0^R r dr m_T I_0 \left(\frac{p_T \sinh \rho}{T_{kin}} \right) K_1 \left(\frac{m_T \cosh \rho}{T_{kin}} \right) \quad (2.5)$$

Here, ρ represents the velocity profile between the integration limits:

$$\rho = \tanh^{-1} \beta_T = \tanh^{-1} \left[\left(\frac{r}{R} \right)^n \beta_S \right] \quad (2.6)$$

where, $m_T = \sqrt{p_T^2 + m^2}$ is the transverse mass, m is the mass of the particle species considered. I_0 and K_1 are modified Bessel functions of first and second kind, respectively. R is the size of the system, β_T is the parametrization of the transverse expansion velocity. β_S is the transverse velocity at the freeze-out surface. The velocity profile is defined by n . The temperature T_{kin} represents the temperature at kinetic (thermal) freeze-out. As the system created in the collision expands, it cools down. The temperature found with Boltzmann blast wave fits of experimental transverse momentum distributions ($\approx 110 MeV$) is lower than the temperature found with thermal models ($\approx 160 MeV$). The blast-wave models give a good description of heavy ion collisions [Schnedermann1993].

2.7.3 Tsallis blast wave

The use of Boltzmann-Gibbs statistics is based on the assumption that the system formed during the collision reaches extensive thermal equilibrium. This assumption

may not be true for short lived systems created in p-p collisions.

Tsallis non-extensive statistics was introduced in 1988 [Tsallis1988] as a generalization of the Boltzmann statistics. Tsallis statistics requires only local equilibrium. The generalization is obtained by defining the entropy as:

$$S_q \equiv k \frac{1 - \sum_{i=1}^W p_i^q}{q - 1} \quad (2.7)$$

Tsallis distribution introduces a new parameter, $q > 1$, called the non-extensive parameter. p_i is the probability that the system is found in i -th micro-state. At the limit $q \rightarrow 1$, the Boltzmann-Gibbs statistics is recovered [Tsallis1988].

When the Tsallis statistics is used for the freeze-out parameterization, the following blast-wave formula is obtained for the transverse momentum spectra:

$$\frac{dN}{m_T dm_T} \propto m_T \int_{-Y}^{+Y} \cosh(y) dy \int_{-\pi}^{+\pi} d\phi \int_0^R r dr \left(1 + \frac{q-1}{T} (m_T \cosh(y) \cosh(\rho) - p_T \sinh(\rho) \cos(\phi))\right)^{-\frac{1}{q-1}} \quad (2.8)$$

Here Y represents the rapidity. The mean transverse velocity can be analytically calculated from the velocity profile: $\langle \beta \rangle = \frac{2}{2+n} \beta_S$.

The q parameter can be interpreted as the degree of non-equilibrium of the system created in the collision. Another interpretation of the q parameter is given in [Beck2002], [Wilk2009] under the assumption that global thermalization is improbable and the system cannot be described by a single temperature. By allowing the temperature to fluctuate, the system can be characterized by the mean temperature $\langle T \rangle$ and another parameter describing the temperature fluctuations. The authors show that:

$$q = 1 + \frac{Var(T)}{\langle T \rangle^2} \quad (2.9)$$

Equation 2.9 gives a physical interpretation of the non-equilibrium parameter. When thermal equilibrium is achieved temperature fluctuations are small, and $q \rightarrow 1$, the Boltzmann-Gibbs statistics is recovered.

The Tsallis distribution is extensively used in recent high energy physics [Abelev2007], [Adare2011], [Aad2011], [Khachatryan2010], [Chatrchyan2011], [Aamodt2010], [Wong2012], [Claymans2012].

2.8 Model predictions

Several Monte Carlo models used in high energy physics implement the features needed for collective behaviour in proton-proton collisions at 7 TeV. Here, EPOS and Pythia 8 are mentioned. Both models, with the right tuning, manage to reproduce the mean p_T as a function of multiplicity [Pierog2013].

2.8.1 EPOS

The EPOS (Energy conserving quantum mechanical multiple scattering approach, based on Partons (parton ladders) Off-shell remnants, and Splitting of parton ladders) model [Pierog2013] based on Gribov-Regge theory [Gribov1983], [Dreasher2001] reproduces features in the p-p collisions although it was developed for heavy ion collisions and cosmic ray studies [Pierog2013]. The two colliding hadrons interact by exchanging a "parton ladder" (see Figure 2.9). There are two regions produced during the collisions. There is one region with a low parton density and another region with a high density of string segments. This two regions are called corona and core, respectively (like in the Glauber formalism terminology). The EPOS model predicts that the core region exhibits similar dynamics in proton-proton collisions as the core from the heavy ion collisions, including the collective effects.

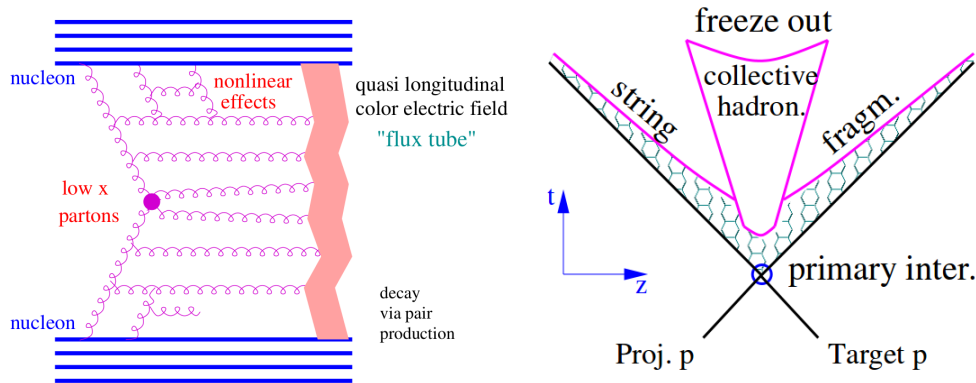


Figure 2.9: Parton ladder mechanism for elementary hadron interaction in EPOS LHC model (left panel). Space time evolution of a hadronic interaction in EPOS (right panel). Pictures from [Pierog2013].

2.8.2 Pythia 8

Pythia 8 includes multi-parton interactions [Sjöstrand2008] and parton re-scatterings. The tunes of Pythia 8 based on results from LHC reproduce the trend in mean p_t [].

A recent paper, [Ortiz2013], argues that the collective type phenomena observed in the mean transverse momentum as a function of multiplicity could have a non-hydrodynamic origin. Using the Pythia 8 generator [Sjöstrand2008], the rising trend in $\langle p_T \rangle$ with multiplicity observed by the CMS collaboration at 7 TeV is reproduced only when the Color Reconnection (CR) is turned on (full symbols in Figure 2.10). Color reconnection, as defined in [Abbiendi2004], represents "a rearrangement of the underlying color structure of an event from its simplest configuration, in which a color flux tube or string is stretched from a quark to an antiquark through intermediate gluons in a manner such that string segments do not cross (a so-called planar diagram [...]), to a more complex pattern in which some segments can either cross or else appear as disconnected entities whose endpoints are gluons". The x

axis represents the mean multiplicity from each multiplicity bin normalized to the minimum bias mean multiplicity. Authors claim that the freeze-out temperature and the average transverse velocity extracted from blast-wave fits of the pion, kaon and proton p_T spectra are similar to the values obtained in heavy ion collisions as a function of multiplicity.

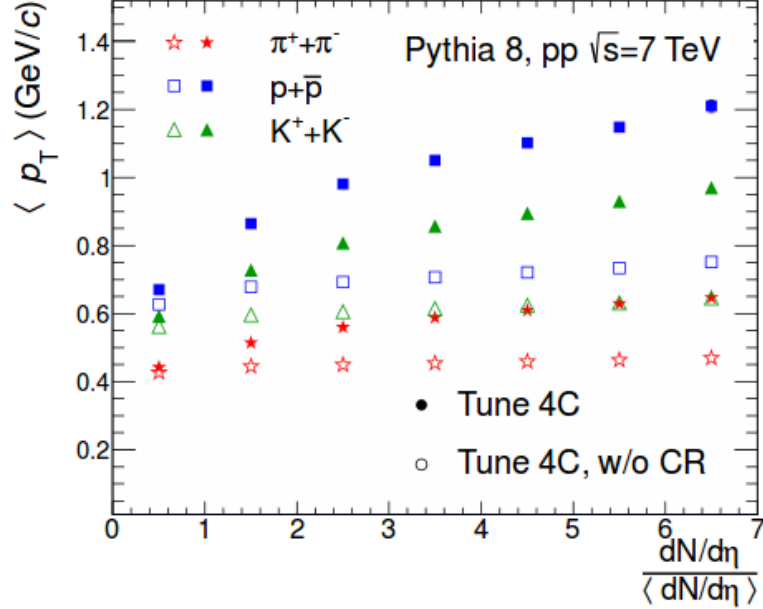


Figure 2.10: Pion, kaon and proton mean transverse momentum vs. multiplicity in Pythia 8 with and without color reconnection (full and, respectively, empty symbols). Picture from [Ortiz2013].

The contribution of color reconnection is not yet understood. Color reconnection is implemented in the current version of Pythia 8 in such a way that its effect is stronger at lower energies. This was not observed in the experimental data. Furthermore, the color reconnection is not limited to proton-proton collisions. What is the effect of color reconnection in heavy ion collisions is not a trivial problem to investigate. If color reconnection is present also in heavy ion collisions, at least a part of the collectivity is not of hydrodynamical origin. This is yet to be understood and studied in detail.

2.9 Discussion

Proton-proton collisions play a key role in understanding the phenomena taking place inside heavy ion collisions. The hot spots of high energy density in the core region of heavy ion collisions must be compared with high multiplicity p-p events where multiple parton-parton interactions play an important role in the production of regions with high energy densities.

In this chapter arguments motivating collectivity studies in proton-proton collisions were discussed. Multi-parton interactions followed by partonic re-scatterings

could justify the use of the hydrodynamical approach. High multiplicities of detected particles are an indication of the high number of partons in the interacting region. Multi-parton interactions followed by several re-scatterings create similar conditions with those found in the core of heavy ion collisions where hydrodynamical description reproduces the experimental results [Huovinen2006], [Gale2013]. Multiple partonic interactions are more likely to occur in high multiplicity events due to high medium density and, therefore, the high multiplicity events are the best candidates for collectivity studies in proton-proton collisions.

Jets were shown to interfere with collective phenomena signals. Investigations of transverse momentum spectra and femtoscopy are strongly influenced by the presence of jets. When collective phenomena are studied, the hard component of the data sample must be eliminated. Therefore, a method capable of rejecting the events containing jets is mandatory. In the present analysis the selection performance of event shape observables is investigated (see section 5). The event shape observables are computed using the transverse momentum of all the particles in the event. Space-momentum correlations are also evidenced by the event shapes and this property is used for the jet rejection.

The algorithm used by the CDF collaboration for soft/hard classification is very simple to implement and the results from FermiLab could be extrapolated at LHC energies. Unfortunately, this algorithm is not well suited for the p-p physics at LHC. At CDF the multiplicity is relatively low in a pseudo-rapidity range ($|\eta| < 1$) slightly larger than the range of the present analysis. The number of particles detected in the ALICE experiment, in $|\eta| < 0.8$, can easily reach values at $\sqrt{s} = 7$ TeV more than 3 times larger than those available at CDF [ALICE2010]. At high multiplicities, in the ALICE acceptance range, there is a very high probability that the CDF algorithm will identify all the events as hard.

The results from CDF [Acosta2002] indicate a multiplicity scaling in terms of transverse momentum spectra and, hence, of the mean transverse momentum for the soft component at two different incident energies. Other studies also indicate that the multiplicity measures the energy pumped into the system.

All this considerations motivated the investigation, in this thesis, of high multiplicity events selected as azimuthally isotropic by the event shape observables.

Chapter 3

Experimental setup

3.1 The Large Hadron Collider

The Large Hadron Collider, operating at CERN near Geneva, is currently the largest and most powerful particle accelerator ever built. The LHC accelerated protons and lead ions at the highest energy ever achieved by human kind. A cascade of accelerators are injecting the protons into the LHC where they are accelerated 8 TeV for the protons and 2.76 TeV per nucleon-pair for lead ions, energies achieved in 2012. Protons accelerated at 7 TeV travel through the beam pipe at more than 99.9999% the speed of light.

With a circumference of ~ 27 km, it was built in the recycled LEP tunnel under the Swiss-French border, at depths between 50 and 175 m. More than 1600 superconducting magnets cooled at -271.3°C (colder than the outer space) are bending each beam trajectory by generating a magnetic field of more than 8 T. The accelerated particles are grouped in bunches traveling in opposite directions. Particle interaction rate is related to the luminosity, defined for colliders as [PDG]:

$$\mathcal{L} = f \frac{n_1 n_2}{4\pi\sigma_x\sigma_y} \quad (3.1)$$

where, f is the collision frequency, n_1 and n_2 are the number of particles in each bunch and $\sigma_{x,y}$ characterize the transverse beam sizes in the horizontal and vertical directions.

At the moment the LHC is in a technical shutdown period for upgrade of the beam energy up to the designed goal of $\sqrt{s} = 14$ TeV for proton-proton collisions and $\sqrt{s_{NN}} = 5.5$ TeV for lead-lead collisions.

In total, at the LHC there are seven experiments:

- A Large Ion Collider Experiment - ALICE
- A Toroidal LHC Apparatus - ATLAS
- Compact Muon Solenoid - CMS
- Large Hadron Collider beauty - LHCb
- Large Hadron Collider forward - LHCf

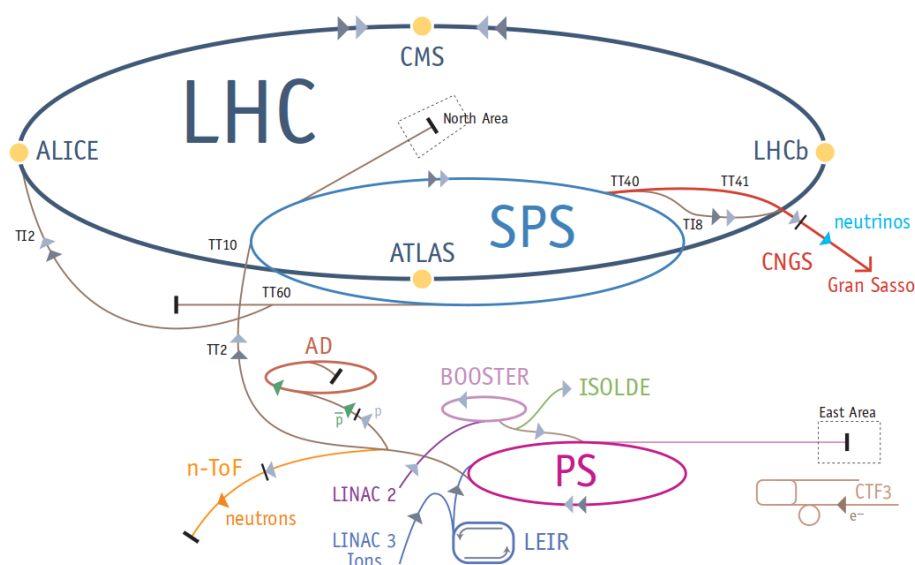


Figure 3.1: Schematic view of the LHC accelerator system. Picture from [LHC].

- Monopole and Exotics Detector At the LHC - MoEDAL
- TOTal Elastic and diffractive cross section Measurement - TOTEM

The most remarkable achievement of the LHC scientific program is the discovery of the Higgs boson announced by the ATLAS and CMS experiments [CMS2012], [ATLAS2012].

3.2 ALICE experimental setup

In the continuous quest of observing nuclear matter under extreme conditions, the experiments keep growing in complexity due to the identification capabilities required for the signals searched are less and less distinguishable from the noise. ALICE (A Large Ion Collider Experiment) is a heavy ion dedicated experiment at CERN [ALICE2004], [ALICE2008]. Designed to study the physics of strongly interacting matter and the Quark Gluon Plasma in heavy-ion collisions at LHC, the ALICE experiment must fulfill extreme requirements in order to identify rare signals originating in the interaction zone. This complex experimental setup designed for Pb-Pb collisions at energies of up to 5.5 TeV/nucleon includes multiple sub-detectors with various and sometime overlapping roles in the detection and identification of emerging particles. Being a general oriented experiment, ALICE will detect particles around mid-rapidity using the so-called Central Barrel built inside the L3 magnet, at high rapidities with the “forward” detectors including a muon arm and will detect the spectator fragments using zero degree calorimeters. Photons emerging from collision will be measured by the Photon Spectrometer detector located under the central barrel. ALICE also includes a cosmic ray trigger.

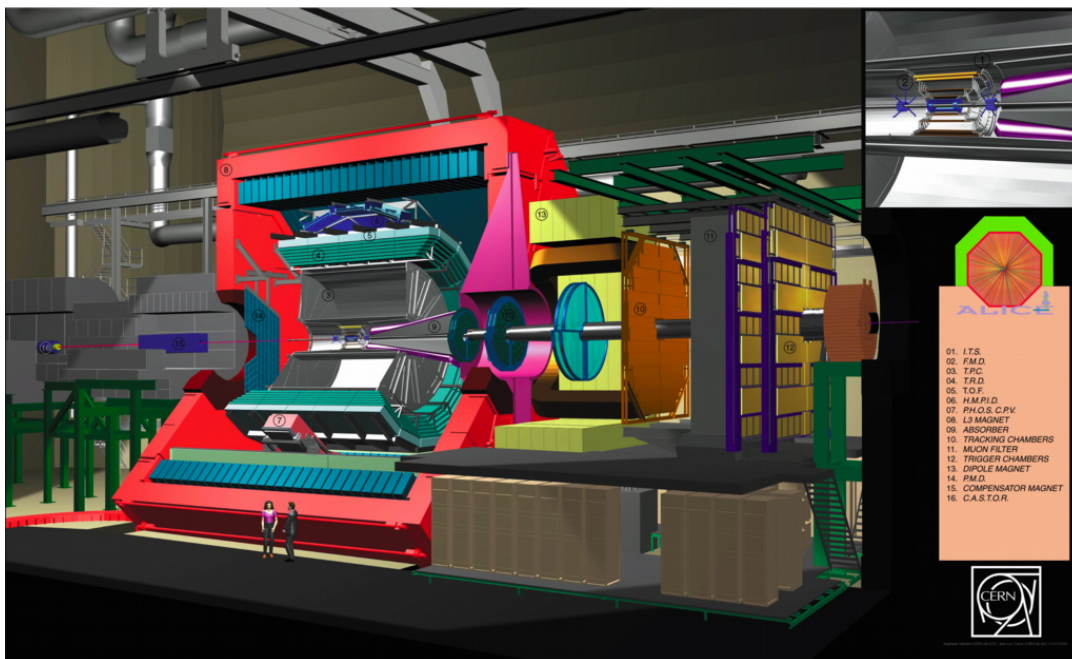


Figure 3.2: Schematic view of the ALICE experimental setup.

3.2.1 Central Barrel Detectors

This section will present the central barrel detectors used in present studies in terms of physics requirements, geometrical description, functioning principles, and physical performances. The detectors described here are:

- ITS - Inner Tracking System
- TPC - Time Projection Chamber

3.2.2 Inner Tracking System

The closest detector to the beam pipe and therefore, to the interaction zone, is the Inner Tracking System (ITS) exemplified in Figure 3.3. The ITS is made out of six layers grouped in three major sub-detector systems: Silicon Pixel Detectors (SPD), Silicon Drift Detectors (SDD) and Silicon Strip Detectors (SSD) [ALICE1999]. The geometry of the ITS is optimized in order to cover the $|\eta| < 0.9$ range in pseudo-rapidity, to get as close as possible to the beam pipe and also to the inner radius of the TPC. The tasks of the ITS are [ALICE2004]:

- to localize the primary vertex with a resolution better than $100 \mu\text{m}$; For establishing the geometry of the event a good vertex resolution is needed. Also the primary particle identification can be done with better accuracy if the primary vertex is reconstructed with an increased efficiency.
- to reconstruct the secondary vertices from decays of hyperons and D and B mesons. The momentum resolution is a key component in short lived particles reconstruction and the study of their properties like mass and width.

The resolution of the reconstructed mass must be comparable, if not better, than the natural width of the resonances to observe possible changes of their parameters. Mass measurements for heavy-flavour states with better resolution improves the signal-to-background ratio in the study of heavy-quarkonia suppression, such as J/ψ and Υ .

- to track and identify particles with momentum below 100 MeV. Charged particles with low momenta will have a high specific energy loss and also their trajectories will be strongly curved by the magnetic field and therefore only the ITS will detect them having an essential contribution to multiplicity measurements and reconstruction of inclusive particle spectra.
- to improve the momentum and angle resolution for the high- p_T particles which also traverse the TPC; The longer the trajectory the better the momentum resolution. ITS has a high granularity which means that tracks can be individually identified improving the tracking quality.
- to reconstruct, although with limited momentum resolution, particles traversing dead regions of the TPC. It is most important to get as close as possible to a 4π detector geometry increasing the total acceptance.

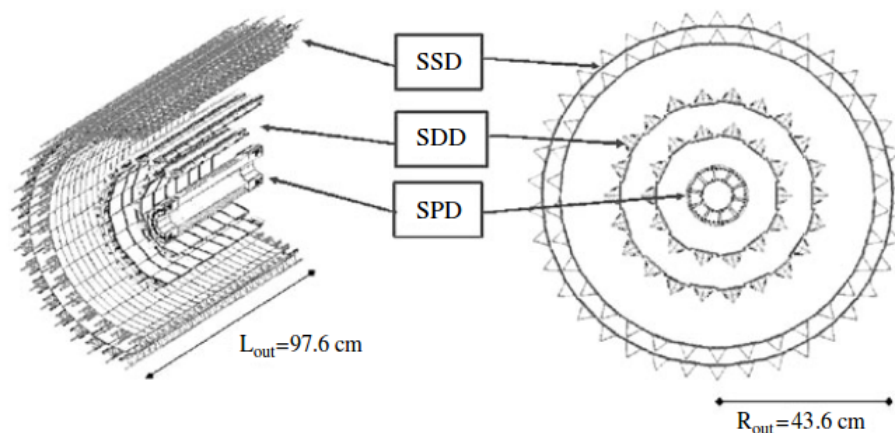


Figure 3.3: Schematic view of the ALICE Inner Tracking System.

Silicon Pixel Detectors

The estimations of particle yield predict up to 8000 tracks per unit of rapidity which is equivalent in the very proximity of the interaction zone to a density of tracks of about 80 particles/cm². As a consequence, the geometry of the two innermost silicon detectors is based on a pixel structure. A particle interacting with a silicon cell will lose energy according to the Bethe-Bloch formula and will be localized by the cell dimensions: $50 \mu\text{m}(r\varphi) \times 425 \mu\text{m}(z)$ in a two dimensional matrix with $200 \mu\text{m}$

sensitive volume thickness and a total of 9.8×10^6 cells. The SPD design implements several specific solutions to minimize the material budget due to the resulting background for other detectors. The average material traversed by a straight track perpendicular to the detector surface is $\approx 1\%X_0$ per layer.

Silicon Drift Detectors

The Silicon Drift Detectors - SDD represent the two intermediate layers of the ITS. The detection principle allows good multi-track performance and also will provide two of the dE/dx samples used for the ITS particle identification. The sensitive area of $70.17 \times 75.26 \text{ mm}^2$ is split into two drift regions by the central cathode strip.

Silicon Strip Detectors

Third ITS subsystem is the SSD - Silicon Strip Detector. The design of this layer is determined in order to optimize the connection of the tracks from TPC to the ITS, to minimize multiple scattering and to provide dE/dx information to assist particle identification for low-momentum particles.

3.2.3 Time Projection Chamber

The Time Projection Chamber (TPC) [ALICE2000] is the main tracking detector of the ALICE central barrel and, together with the ITS and the TRD will provide charged-particle momentum measurements with good two-track separation, particle identification, and vertex determination [Alme2010]. The TPC provides full azimuthal distribution and covers a pseudo-rapidity range of $|\eta| < 0.9$ and, with limited momentum resolution and reduced track length, in the range $0.9 < |\eta| < 1.5$. The tracking efficiency must be larger than 90% for tracks with $p_T > 1 \text{ GeV}/c$ in order to study electron pair production. The study of Υ 's requires a momentum resolution for electrons with momenta of about $4 \text{ GeV}/c$ to be better than 2.5%, resolution achieved only when correlated with the ITS and TRD for magnetic fields around 0.4 T. Since the detection principle (as discussed below) is based on measuring the specific energy loss, the resolution in dE/dx provided by the TPC should be better than 10% for the high-multiplicity environment expected in Pb-Pb collisions. This is motivated by the interest in the electron identification in a high pion multiplicity environment. A pion rejection factor of $> 10^3$ is aimed by the TPC along with the TRD for a 90% electron efficiency at momenta larger than $1 \text{ GeV}/c$. All these requirements must be reached at full luminosity, meaning that the operation rate of the TPC should go up to 200 Hz.

A particle traversing the gas volume, will loose according to the Bethe-Bloch formula a certain amount of energy producing ionizations. This will generate electron pairs inside the gas volume. Due to the electric field, the electrons will drift away from the middle cathode of the TPC towards the read-out electrode. Since the electric field is parallel with magnetic field, the electrons will drift also parallel with the z axis. Depending on the specific location of the initial charge, the time needed to travel the distance to the read-out electrode may vary. This considera-

tions will enable the reconstruction of the x and y coordinates due to the location where the charges arrive, and also the z coordinate if the drift speed is known.

Detector Geometry

As can be seen in Figure 3.4, the TPC is one cylinder with the inner radius of 80 cm, the outer radius of 250 cm and an overall length in the beam direction of 500 cm. The TPC is separated in two equal symmetric parts by a thin foil representing the cathode electrode. The electric field inside the cage will determine the drift of the electrons toward the reading out electrodes. The uniformity of the electric field is assured by intermediate radial multi-wire planes inside the cage. The maximum drift time is $92 \mu s$. Since the electric and the magnetic field lines are parallel, the electrons will drift in the z direction without any deviation, the (x,y) coordinates being reconstructed directly without corrections. The z component is extracted from the total drift time since the drift speed is controlled by the magnitude of the electric field.

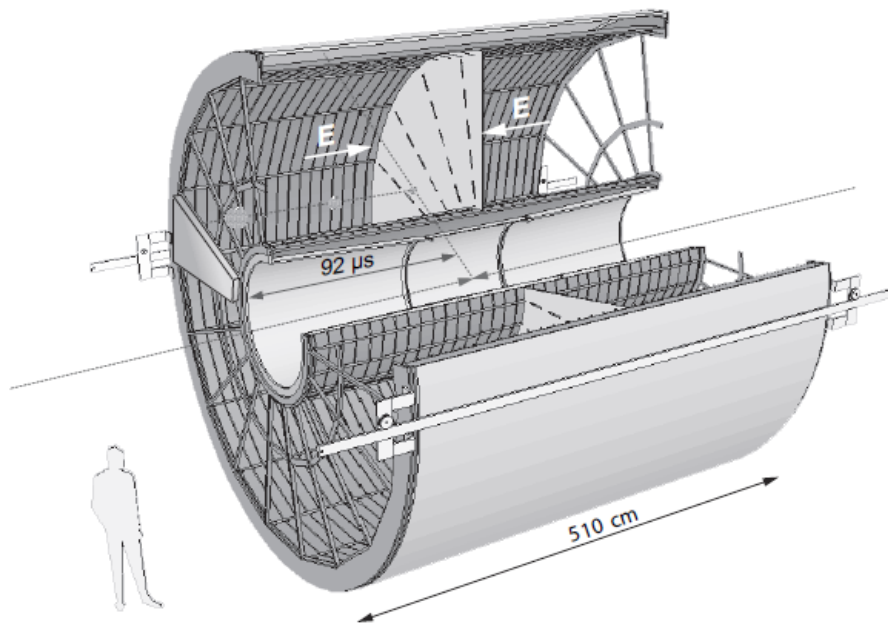


Figure 3.4: Schematic view of the ALICE Time Projection Chamber.

The identification performance can be observed in Figure 3.5 where the results from simulated events are compared to the theoretical Bethe-Bloch dE/dx curves.

3.3 Analysis and computational framework

The large amount of data generated in the modern high energy experiments imposed the mandatory development of new software and hardware infrastructure. The new infrastructure must cope with the complex tasks like data storage, Monte Carlo

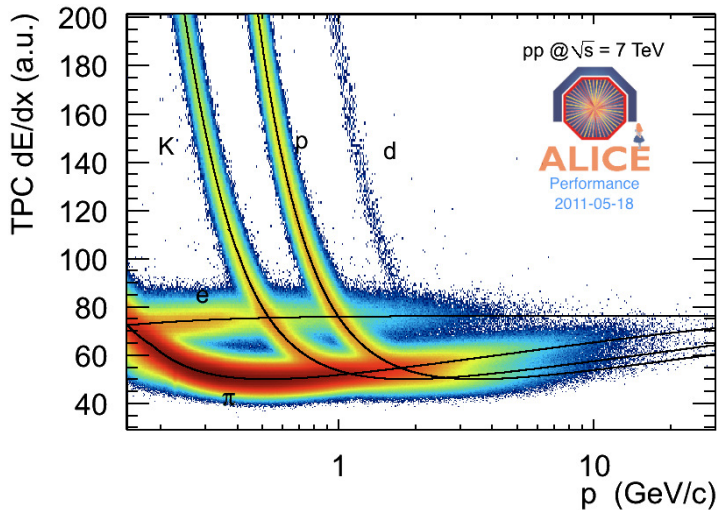


Figure 3.5: Energy loss versus momentum in the ALICE TPC for 7 TeV pp collisions. The lines are the theoretical Bethe-Bloch predictions for dE/dx . Figure ALI-PERF-4849 from ALICE figure repository.

simulations of the experiments, event reconstruction and data analysis. In the case of the ALICE experiment, the computing framework is based on a GRID structure. The ALICE GRID consisting of many data centers, mostly located in Europe, but also in other parts of the world, is able to process tens of thousands of job at any given time. The analysis task of each user is copied to the location of the data and processed locally. In this way, the data transfer is heavily reduced.

The software includes the analysis dedicated framework - AliRoot and the software needed for the job submission on the GRID -ALICE ENvironment - AliEn [AliEn]. A job is basically an analysis task that runs on a particular set of data. The job assignment to the data centers is not transparent to the user since the job management is part of the AliEn framework.

All the information on the raw data and simulated runs, data center occupancy, storage availability and submitted jobs for all the users, can be found at the dedicated monitoring web site [Monalisa].

AliRoot is a complex software framework designed for data processing in the ALICE experiment [AliRoot]. It includes all the features needed for event generation, the transport of the primary particles, the reconstruction and the analysis of the reconstructed data. This can be observed in more details in Figure 3.6. The strategy used during the development of AliRoot was to use as much as possible already existing software packages that had been tested in previous nuclear experiments and to develop new components when needed. Also, the ROOT infrastructure on which AliRoot was developed has been upgraded in the process based on the feed-back from the AliRoot developers. The event generators included in the AliRoot distributions that will be described below are Pythia and Phojet. Particle transport and detector response packages included in AliRoot are GEANT3 (by default) GEANT4 and Fluka.

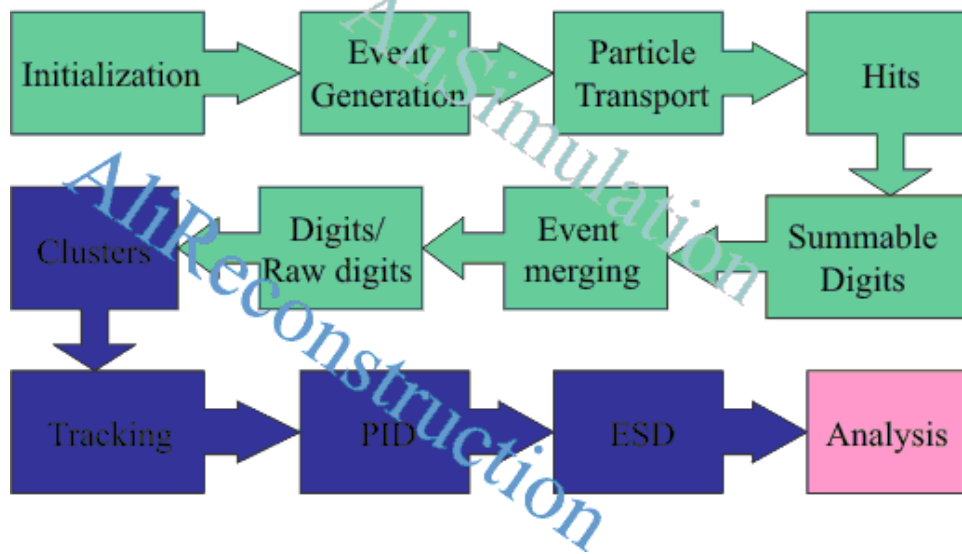


Figure 3.6: General view of data main processing stages in AliRoot.

The analysis of the simulated or real data is the last stage of event processing with various goals depending on the physics involved. The analysis represents also a diagnosis of previous stages when simulated events are used since at this particular moment it may become obvious if something has gone wrong during any of the mentioned steps. Using simulated data one can evaluate the reconstruction capabilities of the AliRoot in order to correct the physics results obtained with real data.

3.3.1 Virtual Monte Carlo

Virtual Monte Carlo - VMC - is a concept designed as an interface between a general user code and a specific Monte Carlo package (i.e. GEANT). The consequence of using this method is that the code written by the user will not suffer any modification (i.e. collision geometry, detector configuration or I/O parameters) when a different Monte Carlo framework is used at a different time. In AliRoot, the MC packages “hidden” by the VMC are GEANT3, GEANT4 and Fluka. The VMC implementation allows the user to ignore specific code conventions in the GEANT, but relevant details about the physics involved should, obviously, be taken into consideration.

Another advantage in using a VMC is that the detector geometry is defined independently of the MC package used in the simulation as can be seen in Figure 3.7.

3.3.2 Event generators

Taking into account the fact that the ALICE experiment is a general purpose designed detector, a complex software for the data analysis is required. Only one particle generator would be insufficient to meet all the physics requirements and, consequently, AliRoot includes a number of oriented event generators. The Monte Carlo generators most commonly used in proton-proton simulations in the ALICE

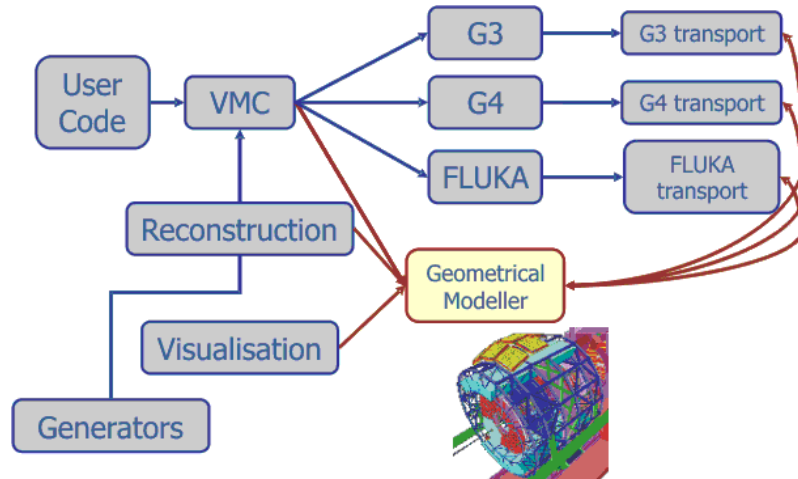


Figure 3.7: General view of the AliRoot Virtual Monte Carlo. The independence of the users code on the packages used can be observed.

Collaboration are Pythia [Sjöstrand2008] and Phojet [Engel1996]. Pythia is also used as a decayer by GEANT in the process of particle transport as some of the particle are not stable. The configuration macro can define what type of decays to be taken into account in the simulation and also can force a particular decay channel for a particle type.

3.3.3 GEANT

The fact that GEANT [Geant4] packages have been extensively tested in nuclear experiments and showed good agreement with the real data determined their usage in AliRoot distribution. Another advantage of GEANT is that it is extremely flexible and allows the user to implement new approaches regarding physics processes to be simulated. The package used for the particle transport and detector response simulation in AliRoot is by default GEANT3, but the user can set the configuration to the alternative GEANT4 or FLUKA. GEANT3, GEANT4 and FLUKA are toolkits for simulation the passage of particles through matter and they include a complete range of functionality including tracking, geometry, physics models and hits. The physics processes taken into account cover a wide range form electromagnetic, hadronic and optical processes and also a large set of particles, materials and elements over a wide energy range from a few hundred eV up to the TeV region. The features of GEANT used for event simulation are: geometry and materials, particle interaction with matter, tracking management, digitization and hit management, event and track management, visualization and user interface.

The geometry of the detectors must include the sensitive areas where "hits" will be generated by the incoming particles and detector response will be simulated using digitization algorithms. Once the detector geometry and materials are defined by the Virtual Monte Carlo subroutine, the transport framework needs as input a list containing the particles to be transported. This is provided by the above mentioned event generators and passed to GEANT after some additional selection are applied.

Additional information regarding the physical processes.

3.3.4 Event reconstruction

After the transport simulation is finished, the next step is the digitization of the hits. The detector response is digitized and formatted according to the output of the front-end electronics and the data acquisition system. The results should resemble the real data that will be produced by the detector. Adjacent digits were presumably generated by the same particle crossing the sensitive area of the detector and are grouped in "clusters". The position of the cluster is then used to reconstruct the track using a set of parameters such as curvature and the angles relative to the coordinate axes together with the covariance matrix estimated at a given point in space. Once the track is reconstructed, the particle types can be identified and the output of the simulation is stored in the Event Summary Data (ESD) files. Each track is reconstructed using the information from different detectors. The ESD files contain the following information about the reconstructed event:

1. reconstructed ZDC energies and number of participants. This information is necessary for reconstructing the reaction plane and centrality of the collision.
2. primary vertex, needed to identify the primary particles and for distance to the Time Of Flight computation.
3. T0 estimation of the primary vertex also needed for the time of flight technique of identifying particles.
4. array of ESD tracks;
5. arrays of HLT tracks both from the conformal mapping and from the Hough transform reconstruction;
6. array of MUON tracks;
7. array of PMD tracks;
8. arrays of reconstructed V^0 vertexes, cascade decays and kinks;
9. indexes of the information from PHOS and EMCAL detectors in the array of the ESD tracks.

Chapter 4

Analysis details

Data acquisition in the ALICE experiment is performed during so-called “periods”. Labels attributed to the periods follow a specific rule. The labels begin with “LHC” followed by two digits year information and the a letter that identifies the period within the year, alphabetically. For example, the “LHC10d” is the fourth period from 2010.

Efficiency corrections are studied on Monte Carlo simulated “anchored” runs. These runs are simulated using the same detector configuration as in the real case. The simulations take into account the geometry and the material budget of the detectors inside the experiment, the applied voltages and also the inactive areas in the corresponding run. The anchored runs also try to reproduce the statistics of the corresponding acquisition run.

4.1 Data selection

The data set used in the analysis presented in the thesis was selected according to the trigger configuration, pile-up probability, run quality and number of events. All this requirements are needed in order to ensure a good quality of the data sample used.

4.1.1 Period selection

The results presented in this thesis are obtained using the ALICE collaboration runs at 7 TeV from LHC10d and LHC10e periods. Data were corrected for efficiency, feed-down and secondary interactions contamination using the corresponding anchored runs of Monte Carlo simulations. Events were simulated, reconstructed and analyzed using the dedicated framework of the collaboration - AliRoot [AliRoot]. Only LHC10d and LHC10e periods were used in the present analysis for reasons discussed below.

The pile-up probability must be reasonably low in order to avoid multiple collisions to be erroneously considered as a single event, affecting the multiplicity, the event shape and also the corrected spectra. Pile-up rejection was used in the analysis but sufficiently close vertexes cannot be discriminated if the relative distance is

below the experimental resolution. Low pile-up events were recorded only in 2010. Later periods cannot be used for this kind of studies.

In section 6.3.1 the model dependence of the efficiency as a function of multiplicity is discussed. The correct reconstruction of the combined multiplicity estimator must be taken into account. The LHC10b and LHC10c do not have yet the combined multiplicity properly reconstructed.

Another requirement is related to the trigger used during the data acquisition. The LHC10d period contains mostly minimum bias trigger events and the LHC10e includes a high multiplicity trigger along with the minimum bias used for reference. LHC10e is the best candidate for analyses targeted at high multiplicities. Most of the results are obtained for the LHC10d period due to the available statistics but also due to the availability of Monte Carlo runs based on Pythia, Phojet and Flat Pythia models. The LHC10e anchored runs have only 10% of the Monte Carlo statistics available. This is insufficient for analysis of high multiplicity events where the efficiency and the feed-down corrections have large statistical fluctuations, especially in the tail of the spectra. A compromise was made in order to access the high multiplicity trigger events. The efficiency evaluation was based on the flat multiplicity events simulated for the 10d period. Only after the corrections are proved to be within few percents multiplicity independent, the high statistics minimum bias efficiency is applied to all multiplicity bins.

High multiplicity events can be contaminated from multiple collisions in the same bunch crossing. Selected data were taken in 2010, period with relatively low-pileup probability. Since pileup events are still possible, even for this data sample, a pileup rejection algorithm was applied. The influence of the pileup is studied comparing the results obtained using runs with low and high multiple collisions probabilities. This is further discussed in section 6.5.

Table 4.1 summarizes all this information. For the pile-up, the maximum value of the Poisson distribution coefficient for the selected runs passing all other criteria is given. Only runs with available pile-up information in the MonALISA [Monalisa] repository were considered. Only runs from LHC10d and LHC10e were used for the final results due to the combined multiplicity estimator available. The combined multiplicity estimator is described in section 4.5.

Table 4.1: Summary of the 2010 LHC periods investigated in this analysis.

Period	Trigger		Monte Carlo			Pile-up (max μ)	Combined Multiplicity
	MB	HM	Pythia	Phojet	Flat		
LHC10b	yes	no	yes	yes	no	-	no
LHC10c	yes	no	yes	yes	no	-	no
LHC10d	yes	no	yes	yes	yes	0.054	yes
LHC10e	yes	yes	10%	10%	no	0.079	yes

4.1.2 Event Selection

The following event cuts were used:

- Minimum Bias - MB - or High Multiplicity - HM - trigger;
- primary vertex z position < 10 cm;
- events are required to be collision candidates.

The minimum bias trigger has the maximum efficiency and the lowest effect on the physics recorded. The high multiplicity trigger is used to enhance by almost an order of magnitude the statistics at multiplicities higher than 40 relative to the minimum bias trigger.

The vertex position is limited due to the efficiency variation as a function of vertex position along beam axis presented in section 4.1.4.

The collision candidate requirement is used to eliminate the so-called non-events (e.g. beam-gas collisions, collisions triggered when there was no beam present).

4.1.3 Trigger selection

The data sets recorded by the ALICE experiment and analyzed in this thesis were collected with two trigger configurations. The Minimum Bias trigger is configured in such a manner that it minimizes the systematic effect of the detector. The on-line MB trigger is conditioned by a signal in either of the V0 detectors or a hit in the Silicon Pixel Detector. The signal in the detectors must come in a time window corresponding to a beam crossing from both sides of the experiment. This requirement eliminates the collisions that might be triggered, for example, by an interaction of one beam with that gas inside the beam pipe.

The High Multiplicity trigger was designed to allow the acquisition of events with high number of particles. The multiplicity distribution for MB and HM triggers and their ratio can be seen in Figure 4.1. The HM distribution introduces a hardware bias at charged particle multiplicities lower than 50. The two combined multiplicity distributions have almost the same shape for multiplicities larger than 50, as can be seen in the left panel. A quantitative comparison can be seen on the right panel. The ratio of the multiplicity distributions for the two hardware trigger configurations reaches a plateau for charged particle multiplicities larger than 50.

4.1.4 Vertex selection

The vertex position along the beam direction is limited due to the TPC geometrical acceptance. The vertex distributions for the Pythia and data used in the analysis are plotted in Figure 4.2.

As plotted in Figure 6.1, the efficiency decreases with $\sim 5\%$ when the vertex position is within 9-10 cm from the center of the detector relative to when the vertex is in the limit of 0.5 cm. This is the reason for the pseudo-rapidity range of ± 0.8 in the present analysis. Events with vertex outside the 10 cm limit will contain particles that will hit the edge of the TPC and, due to the minimum number of

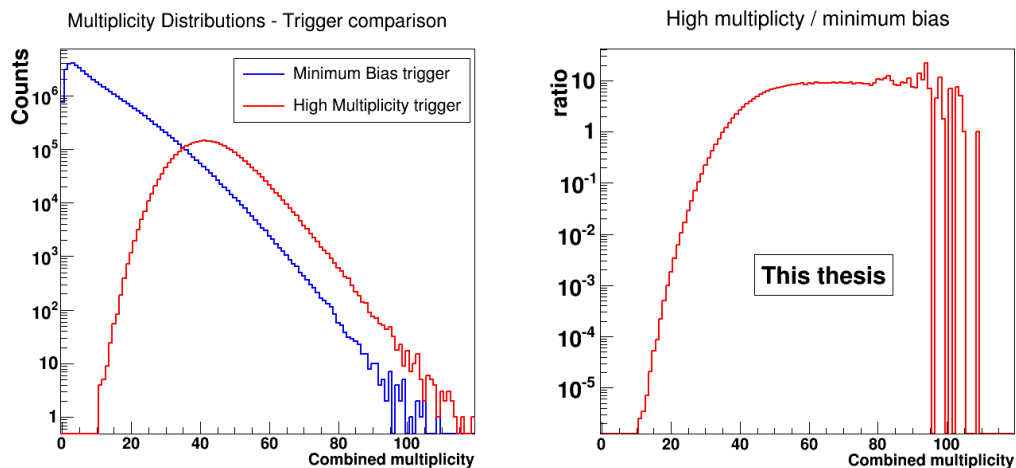


Figure 4.1: Minimum Bias (in blue) and High Multiplicity (in red) trigger combined multiplicity distributions (left panel) and their ratio (right panel).

clusters requirement described below, will not pass the track cuts. Therefore, the associated tracks have lower efficiency. Approximately 10% of the events are rejected by this condition (see section 6.2).

4.1.5 Pileup rejection

Multiple collisions from a single triggered event (pileup) must be rejected in the analysis presented in this thesis. Pileup events have an artificially increased multiplicity and events migrate to higher multiplicity bins. The multi-collision probability follows a Poisson distribution characteristic to rare events. The Poisson distribution is defined by the mean of the distribution - μ . This parameter is used for the pileup probability evaluation in the data runs from ALICE (see [Monalisa]). In order to limit the impact of multiple collisions in one event, for the LHC10d period, the runs with μ limited to 0.054 were selected for this analysis. For the LHC10e high multiplicity period, where only few of the runs have a $\mu < 0.05$, the maximum μ is 0.079. Later periods have higher μ values due to the increase of the beam luminosity.

A pileup rejection was used in order to reject as much as possible multiple collisions in the same event, even for low luminosity runs. This rejection minimizes the pileup contamination in the data sample.

4.1.6 Track selection

The information on the particle reconstruction obtained with the Inner Tracking System and the Time Projection Chamber is used, in this analysis, in order to evaluate the quality of the track reconstruction. The following cuts were established within the ALICE Collaboration in order to select tracks with high quality reconstruction:

- minimum TPC clusters = 70;

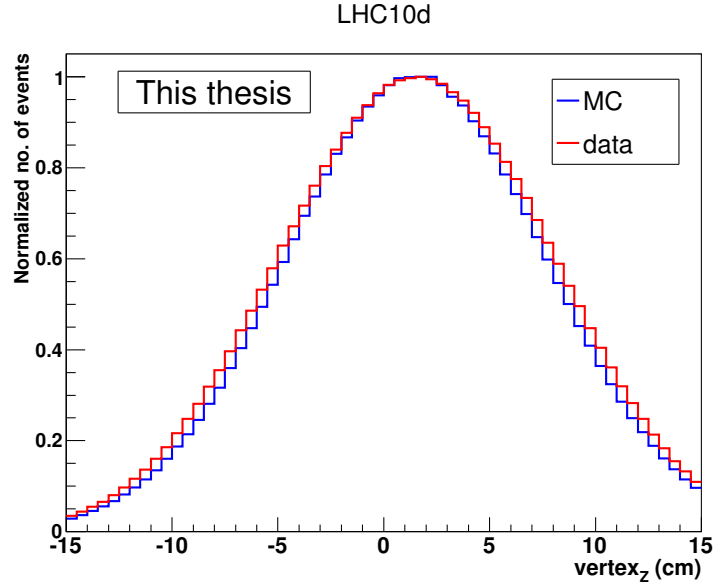


Figure 4.2: Vertex distribution along the beam axis - z for Pythia anchor runs (blue) and data (red) for the LHC10d period. The two distributions are normalized to the corresponding highest value.

- maximum χ^2 per cluster in the TPC = 4;
- TPC refit and ITS refit required;
- kink daughters not accepted;
- no p_T cut;
- $|\eta| < 0.8$;
- one cluster in the SPD;
- maximum DCA¹ to vertex in (x,y) plane = $0.0182 + 0.0350/p_T^{1.01}$;
- maximum DCA to vertex in $z = 2$ cm;

This set of cuts is called “standard 2010 cuts”. The same cuts are used for the data and Monte Carlo simulations at the level of reconstructed tracks.

The minimum number of TPC clusters set to 70 (the maximum is 159) correlated with the maximum χ^2 ensures a good track quality in the TPC. Kinks in the reconstructed track are likely coming from decays and the products are not considered primary even if all other cuts are passed. The η cut is imposed due to TPC geometric efficiency. The distance of closest approach of the track relative (see Figure 4.3) to the primary vertex is used to reject tracks coming from “slow” weak decays ($\tau > 10^{-22}$ s) and secondary interactions. Tracks that have kinks are also eliminated from the data. Kinks are specific to decays. The presence of a signal in at least

¹DCA - Distance to Closest Approach

one cluster in the Silicon Pixel Detectors maximizes the likelihood of a track to be primary and allows a better estimation of the DCA.

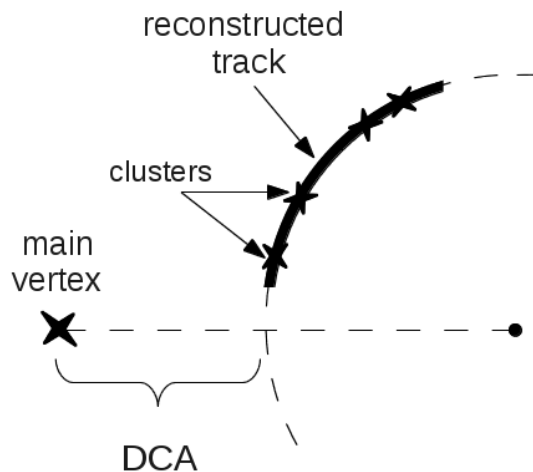


Figure 4.3: Definition of the DCA - distance of closest approach.

For the Monte Carlo generated events, the following particle cuts were implemented:

- $|\eta| < 0.8$;
- the particle has to be charged;
- the particle must be primary

Particles are considered primary if they are generated in the collision or are the products of fast decaying resonances ($\tau < 10^{-22} s$). Daughter particles of slow decays are not considered primary because their contribution to the corrected yield can be eliminated using DCA studies as described in section 6.4.1.

These cuts have a minimum bias on the selected tracks detected in the Central Barrel. In this thesis, only the positive charged particles are considered. The motivation for this choice is the difference observed for propagation through the detector of the negative charged particles between GEANT and FLUKA simulation codes (e.g. [Leeuwen2011]).

4.2 Multiplicity estimation

Multiplicity is defined as the number of charged particles in a given pseudo-rapidity range. The pseudo-rapidity range used in this analysis is $|\eta| < 0.8$. Evaluating the multiplicity from the reconstructed data is not a straight forward task. Two estimators for the multiplicity were used in this analysis and are described in the next sections.

4.2.1 Global Tracks multiplicity

One method used for the estimation of the multiplicity in each event is to count the number of global tracks. These are the tracks that pass the standard track cuts listed in section 4.1.6. These are also the tracks that are used in the final analysis. The correlation matrix for this estimator is plotted in Figure 4.4. The slope of the distribution is ~ 0.7 . The contribution from weak decays and secondaries to the number of global tracks is evaluated at few percents of the total number of tracks. Their contribution is eliminated as described in section 6.4.1.

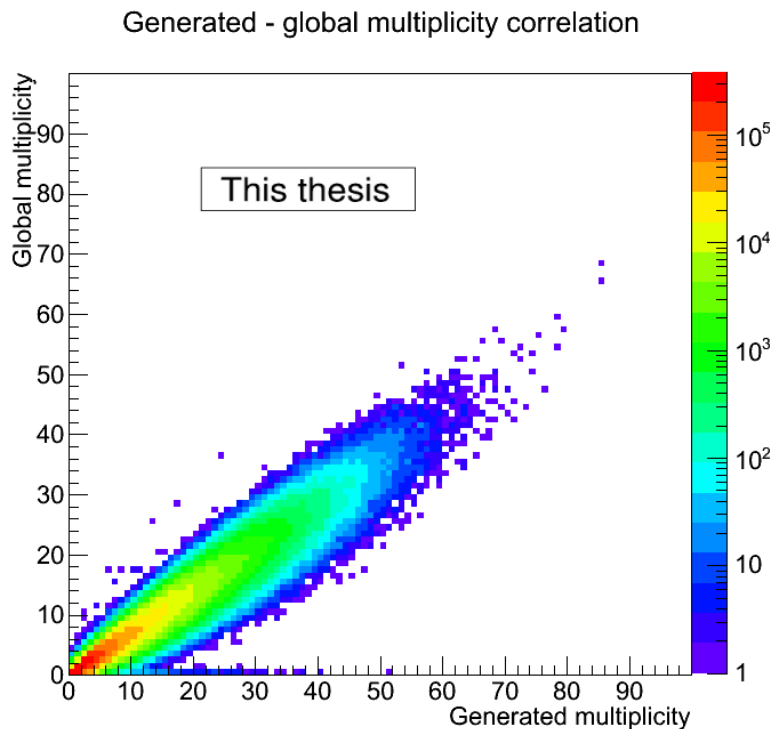


Figure 4.4: Correlation matrix for the Global Multiplicity estimator. Generated multiplicity represents the primary particle multiplicity obtained from Monte Carlo generator. Global multiplicity is estimated after the reconstruction of the simulated events.

4.2.2 Combined multiplicity estimator

Another multiplicity estimator was introduced in order to reproduce the primary multiplicity better. The Combined Multiplicity - CM - is estimated using the following algorithm [Shahoyan]: count all the global tracks, add the tracks which are not global but are reconstructed by the ITS stand alone and, finally, add the tracks that can be reconstructed from SPD tracklets that do not belong to any previously counted tracks and can be extrapolated to the primary vertex. This algorithm is presented in Figure 4.5.

The correlation matrix for the combined multiplicity estimator is plotted in Figure 4.6. It can be seen that the distribution is narrower than in the global multiplicity case and the primary multiplicity is better estimated. The slope of the distribution is ~ 0.89 .

Several events show a clear deviation from the main distribution. These events are called outliers and they are events with the vertex position in z direction very close to the 10 cm limit. A vertex cut limit smaller than 10 cm eliminates the outliers. The reason why such a cut was not used is the fact that the total contribution of the outliers is relatively small. The total number of outlier events was evaluated at 0.004%. Therefore, their contribution is below any other systematic effect presented in 6.5. In the same time, a more strict cut eliminates a big number of events that are well reconstructed and the systematics is reduced. The vertex cut was maintained at 10 cm.

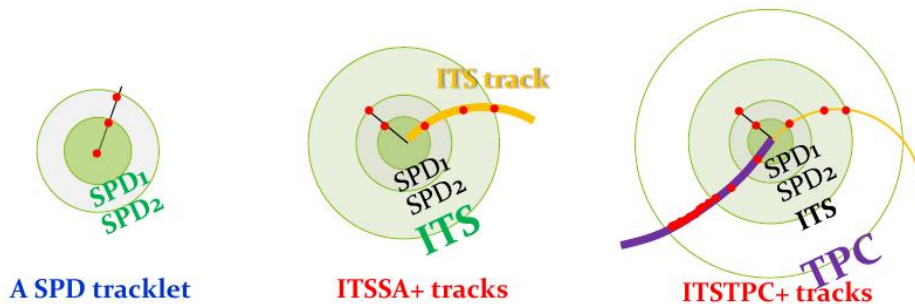


Figure 4.5: Combined multiplicity estimation algorithm.

The correspondence between the multiplicity bin limits for the global and combined multiplicity estimators, listed in Table 6.1, is calculated using the correlation matrix from Figure 4.7. Each global multiplicity bin limit (vertical line corresponding to global multiplicity = 20 in the example from Figure 4.7) defines a wide distribution for the combined multiplicity. The bin on Y axis that corresponds to the maximum of this distribution gives the selected values for the combined multiplicity bin limit.

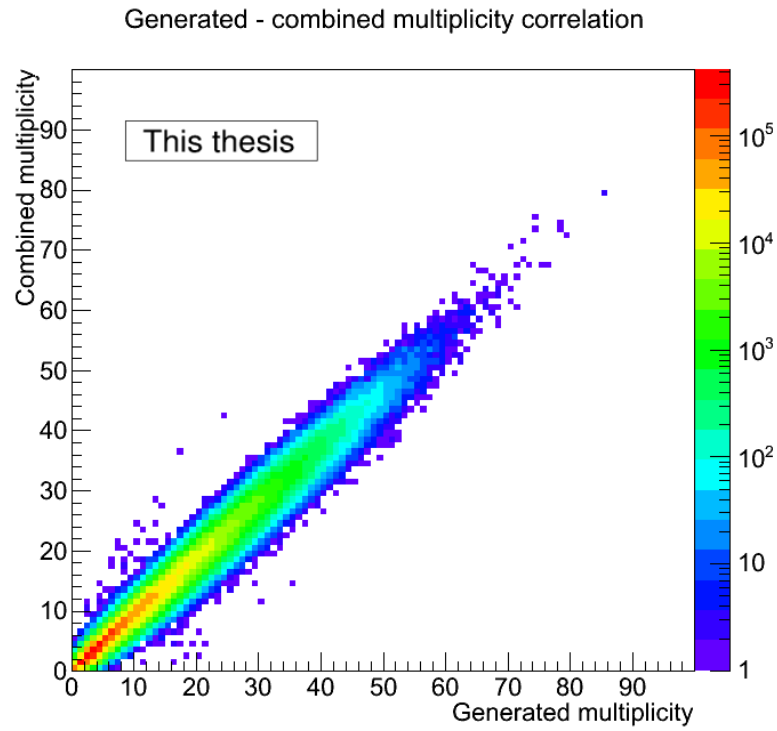


Figure 4.6: Correlation matrix for the Combined Multiplicity estimator.

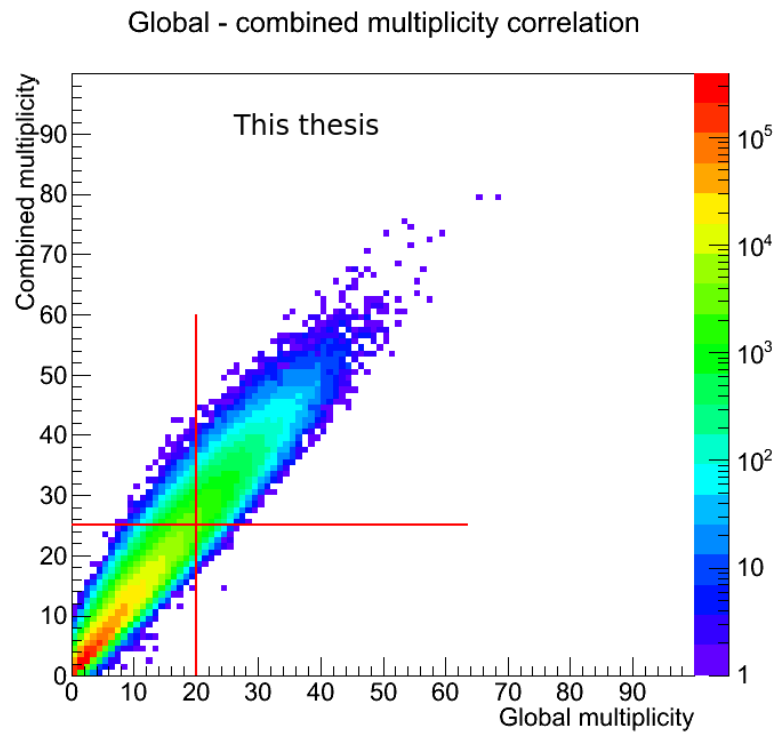


Figure 4.7: Bin limit estimation for the combined multiplicity estimator.

Chapter 5

Event shape observables

*“He who asks is a fool for five minutes,
but he who does not ask remains a fool forever.”
Chinese Proverb*

The hadronic final states formed in high energy collisions can manifest different topologies depending on the underlying processes. The topology of each event can be characterized by several event shape variables built using the detected particles. By definition, the event shape observables are designed to measure the energy flow in the collision. They are constructed using both the orientation and the magnitude of each particle momentum. Several event shapes observables - ESO - have been used for more than forty years in high energy physics (e.g. [Bjorken1970]). Originally, these observables were used in jet studies to evidence parton hard scatterings that translate into hadronic jets, discovered at SPEAR [Hanson1975] and DESY [Banderlik1979], [Barber1979], [Bartel1980], [Berger1979]. The study of jets is a central part of the perturbative QCD studies that extract the properties of quarks and gluons from the hadron distribution in the final event.

Using a different approach, in this analysis, event shape observables are used to identify events with random particle distributions. A uniform particle distribution is specific to a non-jetty event. Such isotropic events could reveal properties of the matter created in the collision in the soft region of the spectrum, region described phenomenologically. This approach raises some questions on the event selection performance of the event shapes observables. Can events with jets be labeled as uniform by using the event shapes? Is it possible to use the same observables that are used to select jetty events to clean the data sample? Are the selected events in any way biased? Is there a spectrum that randomly distributed in azimuth is not biased by the event shape selection?

Even if the jet identifying algorithms have radically evolved in the past decade, especially due to Tevatron and RHIC experimental results [Cacciari2011], rejecting events with jets identified using any jet finding algorithms is considered not feasible since reconstructed jets have relatively high transverse momenta (≈ 20 GeV/c, [ALICE2013a]).

One problem when studying collective effects is that jets can mimic flow both

when using azimuthal distribution methods based on Fourier decomposition and when using particle's spectra studies. The method based on ESO has the clear advantage that it doesn't depend on any specific jet algorithm. The study of the p_T spectra requires a method that eliminates events with jets from the analysis. Although jets originate in hard processes and are characterized by high p_T values they may also influence the so called underlying event in the soft region of the spectra. This is the reason why the selected events should not contain jets. The event shapes observables were used for jet studies due to their capability of identifying events with two or three jets. Using a complementary approach, in this thesis event shape observables are used to reject the events containing jets.

In this chapter, sphericity [Bjorken1970], thrust [Brandt1964], [Fahri1977], directivity [Beckmann1987], recoil [Banfi2004] and modified transverse Fox-Wolfram moments [Fox-Wolfram1979] are studied. After the introduction of these observables, details on their multiplicity dependence are presented for minimum bias and high multiplicity trigger configurations. Based on data and toy models, the selection capabilities of the event shape observables used in the present work are evaluated as a function of multiplicity.

5.1 Directivity

Directivity - D - is defined as:

$$D^\pm = \frac{|\sum_i \vec{p}_{t,i}|}{\sum_i |\vec{p}_{t,i}|} \Big|_{\eta^{pos/neg}} \quad (5.1)$$

and measures the normalized momentum deviation from 0 in the positive or negative η ranges [Beckmann1987], [Alard1992]. Directivity was originally used to determine the event plane in heavy ion collisions where the collective flow induces an enhanced particle emission in a direction correlated with the event plane [Reisdorf1999]. The reason for using this observable in this thesis is that events with jets will have the sum over $|p_T|$ deviating from 0 and will generate high directivity values. Still, there are special configurations of multiple jet distributions in the (p_T, φ) phase space or long range correlations of the type evidenced by CMS Collaboration [CMS2010a] characterized by low directivity value. The probability for such events to occur is considered to be low due to the special configurations required. Multiple jets must have a relatively uniform orientation but also a momentum distribution such that the magnitude of the vectorial sum is low enough for the directivity to have a small value.

On the other hand, high multiplicity events may have a low directivity value, due to the normalization factor, even if they contain jets. For example, if an event contains a jet of 50 GeV/c in one η region and the underlying event has 50 particles evenly spread in the azimuth with an average momentum of 0.5 GeV/c, the directivity will be equal to $50/75 = 0.66$, close to the middle of the directivity range. For an event to be classified as uniform ($D < 0.3$) in the previous example, the jet momentum should not be higher than ~ 11 GeV/c, which is a rather high value for the purpose of this study. This is also in agreement with the multiplicity dependence of directivity plotted in Figure 5.6. The directivity goes to rather low values for the

high multiplicity range but jets are still present. Therefore, high multiplicity events that contain jets will not necessarily have a high directivity value.

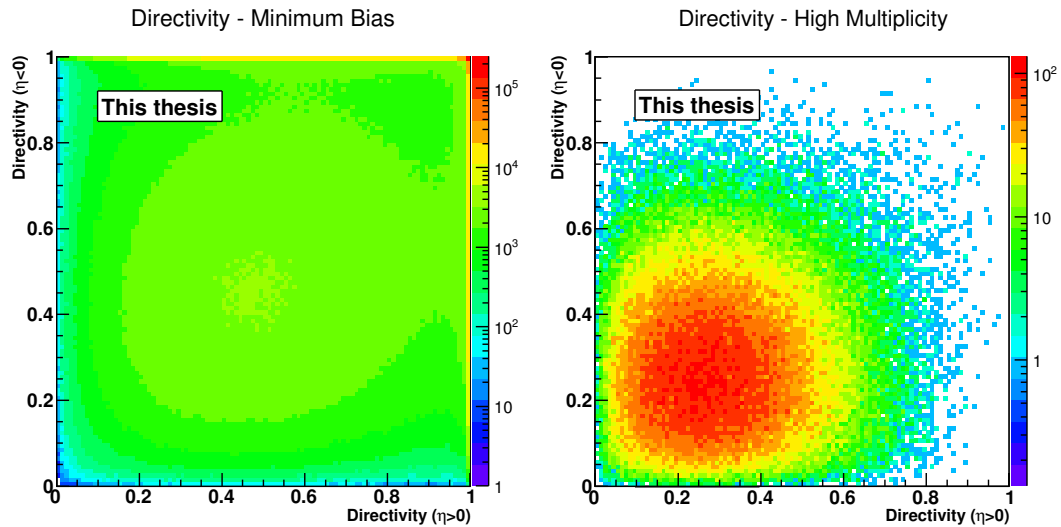


Figure 5.1: Directivity for particles with negative η vs. directivity for positive η for Minimum Bias trigger (left panel) and High Multiplicity trigger (right panel).

The first attempt to study directivity as an observable capable of selecting uniform events was performed by using the directivity value in one side of the detector corresponding to η either positive or negative. In the process of evaluating the directivity selection performance it was noted that particle distributions relative to the leading particle were substantially different for the two η regions. Large differences in the directivity values for the two η regions were found to be the cause of this behavior. The correlation between D^+ and D^- is plotted in Figure 5.1. One can see that events called “highly isotropic” for extremely low values of directivity for positive η can have large directivity values in the negative η region. Averaging on D^+ and D^- will mix the distributions belonging to different classes. Less pronounced, the same mixing will occur even for high multiplicities as shown in the right panel of Figure 5.1. The choice for this analysis was to use cuts on both directivity values simultaneously.

5.2 Thrust

Thrust - T - [Brandt1964], [Fahri1977] is defined as the normalized maximum value of the momentum projection on an arbitrary axis, summed over all particles in the event:

$$T = \underbrace{\max}_{\vec{n}} \frac{\sum_i |\vec{p}_i \cdot \vec{n}|}{\sum_i |\vec{p}_i|} \quad (5.2)$$

The orientation of \vec{n} for which the thrust maximum value is obtained is called the

thrust axis and is denoted by \vec{n}_T . Transverse thrust using the transverse projection of each particle's momentum is defined in the same manner:

$$T = \underbrace{\max}_{\vec{n}_T} \frac{\sum_i |\vec{p}_{t,i} \cdot \vec{n}_T|}{\sum_i |\vec{p}_{t,i}|} \quad (5.3)$$

This definition is useful when rapidity coverage of the experiment is rather low. In this case, the thrust axis will be contained in the transverse plane due to the maximum condition. The analysis presented in this paper uses the transverse thrust definition due to the low pseudo-rapidity coverage of the ALICE experimental setup at mid-rapidity.

Trust is, by definition, always positive. Since the numerator is always smaller than the denominator, the thrust is always smaller than 1. This value is reached only when the sum of the momentum projections is equal to the sum of the particle's momentum and this is possible only for perfectly aligned events (i.e. all the particles are detected in the same direction). This is a reasonable approximation of two jets events where particles with high momenta are generated and emitted in opposite directions. For the transverse thrust, the lower limit is $2/\pi \simeq 0.6367$.

5.3 Sphericity

Sphericity - S - was introduced in [Bjorken1970] and it measures how close to being spherical the particle distribution in the event is. The spherical shape will be replaced by a circular one when the particles are projected in the transverse plane. To define and compute the transverse sphericity, the properties of the eigenvalues are used. First, the following matrix is built:

$$S_{xy} = \frac{1}{\sum_i p_T^{(i)2}} \sum_i \begin{pmatrix} p_x^{(i)2} & p_x^{(i)} p_y^{(i)} \\ p_x^{(i)} p_y^{(i)} & p_y^{(i)2} \end{pmatrix} \quad (5.4)$$

where $p_x^{(i)}$ and $p_y^{(i)}$ are the transverse components of the i -th particle three-momentum in the center of mass reference system. The sum runs over all detected particles. Note that this is the two-dimensional case corresponding to the transverse plane. Once the eigenvalues ($\lambda_1 > \lambda_2$) of the matrix defined above, (5.4), are found, the sphericity is defined as:

$$S_{\perp} \equiv \frac{2\lambda_2}{\lambda_2 + \lambda_1} \quad (5.5)$$

Sphericity can take values from 0 for ‘‘pencil-like’’ events up to 1 for isotropic events. Two back-to-back jets represents an extreme case where the smaller eigenvalue of the sphericity matrix tends to zero. Following from equation (5.5) S_{\perp} is also zero. For an isotropic event, the two eigenvalues will be equal as the distribution will be isotropic and there will be no preferential direction. This immediately leads to a unitary S_{\perp} .

Linear sphericity

Sphericity defined using the matrix (5.4) is not “collinear safe”, as required by the QCD calculations. Collinear safe means that changing one particle with two collinear particles with summed four-momenta equal to the original one will not change the estimation of that particular observable. This is clearly not the case of the sphericity that is a quadratic form in momentum components and $p_1^2 + p_2^2 \neq (p_1 + p_2)^2$. This considerations do not imply that sphericity cannot be used for event shape analysis where the eigenvalues properties remain valid.

The collinear safe version of the sphericity is given by the linear sphericity defined as:

$$S_{xy}^{lin} = \frac{1}{\sum_i p_T^i} \sum_i \frac{1}{p_T^i} \begin{pmatrix} p_x^{(i)2} & p_x^{(i)} p_y^{(i)} \\ p_x^{(i)} p_y^{(i)} & p_y^{(i)2} \end{pmatrix} \quad (5.6)$$

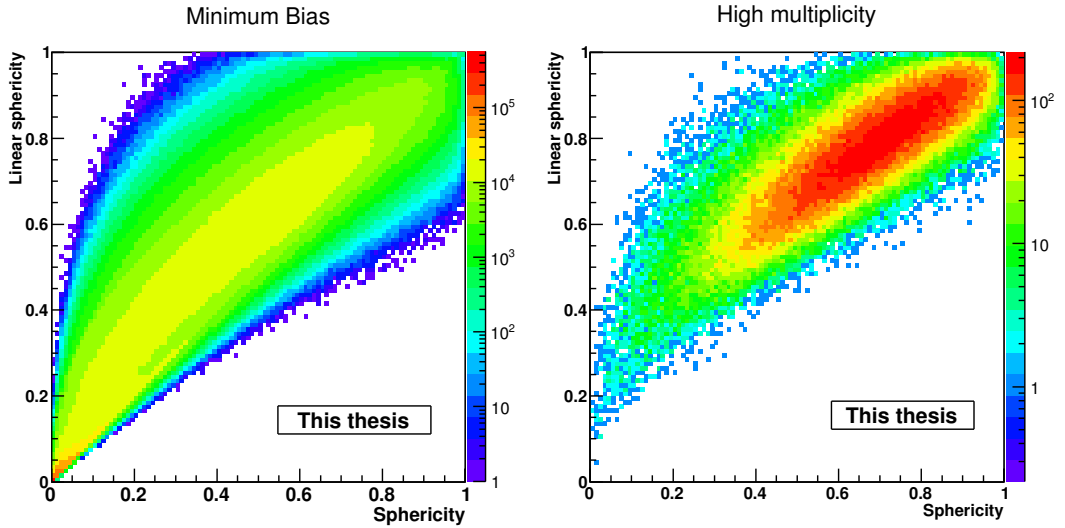


Figure 5.2: Linear sphericity versus sphericity for MB (left) and HM (right) triggers.

The correlation between sphericity and linear sphericity is displayed in Figure 5.2 for both Minimum Bias and High Multiplicity triggers. One can see that the correlation is relatively wide in the allowed kinematic range. In this thesis, the non-linear form of sphericity is used.

5.4 Recoil

The recoil - R - is defined as:

$$R = \frac{|\sum_i \vec{p}_{t,i}|}{\sum_i |\vec{p}_{t,i}|} \quad (5.7)$$

and it measures how well the momentum conservation is reconstructed in the event [Banfi2004]. Obviously, due to conservation principles, the total momentum is conserved and the total transverse momentum should be zero. This is usually not the case in a real experiment where any detector has a limited acceptance and reconstruction efficiency. To ensure the selection of symmetric events desired by this analysis, the cut on recoil will require small values, as close as possible to zero. Selecting events with small recoil will reject events where many particles are lost in one side of the detector assuming a symmetrical geometry. Recoil alone will not differentiate, for example, between events with two jets or three jets where the momentum is well reconstructed. Also, it will not select on its own azimuthally highly isotropic events. This is the reason why the recoil must be combined with at least one other global observable in order to characterize the events.

For the ALICE experiment in particular, recoil deviates from 0 due to acceptance, efficiency, reconstruction resolution, and neutral particles that are not detected.

5.5 Fox-Wolfram moments

Fox-Wolfram moments - FWM - were introduced by G.C. Fox and S. Wolfram in [Fox-Wolfram1979] and are defined as:

$$H_l \equiv \frac{4\pi}{2l+1} \sum_{m=-l}^{+l} \left| \sum_i Y_l^m(\Omega_i) \frac{|p_i|}{E_{tot}} \right|^2 = \sum_{i,j} \frac{p_i p_j P_l(\cos\phi_{ij})}{E_{tot}^2} \quad (5.8)$$

where p_i and p_j are the momenta of the i -th and, respectively, j -th particle in the event, E_{tot} is the total energy of the resulting particles, ϕ_{ij} is the angle between the i -th and j -th particle and P_l are the Legendre polynomials. The sum is taken over all the hadron pairs produced in the event, including the situation when i equals j . The first Legendre polynomials are:

$$\begin{aligned} P_0(x) &= 1 \\ P_1(x) &= x \\ P_2(x) &= \frac{1}{2}(3x^2 - 1) \\ P_3(x) &= \frac{1}{2}(5x^3 + x) \end{aligned}$$

Higher order Legendre polynomials can be computed using the recurrence formula:

$$(n+1)P_{n+1}(x) = (2n+1)xP_n(x) - nP_{n-1}(x)$$

5.5.1 General properties of Fox-Wolfram moments

As shown in [Fox-Wolfram1979], the FWM define a complete set of event shape observables. As a consequence, in order to distinguish between events with different shapes, by definition, one has to use at least several H_l values. This is more clear when looking at table 5.1, where the H_l for values of l up to 8 are shown for different ideal event shapes. Also, another reason why using only one event shape observable is not enough to discriminate between events is that multi-dimensional shapes cannot be described by a single number. In other words, significantly different topologies will have similar event shape values. As an example, this can be seen in 5.11.2. Events with n particles have the same sphericity and thrust values.

Another problem of using individual event shapes is that for sufficiently high multiplicity events with few jets or events with sufficiently high number of jets distributed more or less uniform, the separation from the truly uniform events becomes less perfect.

FWM are also rotationally invariant and, more importantly for QCD computations, infrared stable [Fox-Wolfram1979].

Another important and very interesting property of the FWM is that they have a higher value for orders that are multiple of the event symmetry order. More explicitly, for triangular events, H_3 and H_6 have higher values than their neighbors (see Table 5.1). This indicates a method to eliminate (or select) multiple jets events. This kind of events cannot be discriminated by the other event shape observables.

In this study, uniform events are selected using a narrow region (see Table 5.8.3) around the values corresponding the “equatorial” event shape.

Table 5.1: The first eight Fox-Wolfram moments for different ideal event shape events.

shape	H_0	H_1	H_2	H_3	H_4	H_5	H_6	H_7	H_8
single jet	1	1	1	1	1	1	1	1	1
liniar	1	0	1	0	1	0	1	0	1
triangular	1	0	0.25	0.63	0.14	0.27	0.55	0.18	0.28
square	1	0	0.25	0	0.69	0	0.34	0	0.64
equatorial	1	0	0.25	0	0.14	0	0.10	0	0.08

5.5.2 Modified Fox-Wolfram moments

The Fox-Wolfram moments are usually normalized to H_0 [Fox-Wolfram1979], [Filed1997]:

$$\frac{H_l}{H_0} = \frac{\sum_{i,j} p_i p_j P_l(\cos\phi_{ij})}{\sum_{i,j} p_i p_j}$$

The same expression is obtained in the massless particles approximation for the initial definition of the FWM. With this definition, H_0 is always 1 and there is no

reason to use it any further in the study. In the analysis presented in this thesis, the particle's transverse momenta is used and, therefore, what was called in the original paper and in table 5.1 "equatorial", in this thesis will be equivalent to uniform or azimuthally isotropic, with the transverse plane representing the equatorial plane.

5.5.3 Correlation between FWM and other Event Shape Observables

Using the normalized expression for H_l , one can see that:

$$H_1 = \frac{\sum_{i,j} p_i p_j \cos\phi_{ij}}{\sum_{i,j} p_i p_j} = \frac{(\sum_i \vec{p}_i)^2}{(\sum_i p_i)^2} = R^2$$

where R is the recoil [Banfi2004]. The fact that one FWM is related with the recoil is not surprising since the FWM are a complete set of event shape observables and must include some information about the recoil of the event.

5.6 Examples based on Pythia

Examples of high multiplicity uniform and jet-like events are shown in Figures 5.3 and 5.4. The distribution of the charged particles in the (η, φ) plane is plotted in the upper left plot. The projection of each particle's momentum on the transverse plane is presented in the upper right plot. Red lines are used for the particles in the negative η region and blue for the positive one. All momenta are normalized to the leading particle momentum. The black line is the computed thrust axis. For the jet-like case (figure 5.4), the thrust axis is clearly defined by the jets orientation. For the uniform case (figure 5.3), the \vec{n}_T is determined rather by a fluctuation than a real anisotropy of the event.

In the lower left plot, the FWM for the analyzed events are compared with expected values for several geometries mentioned in section 5.5. It is clearly visible that the uniform event has FWM values extremely close to the "circular" geometry. For the two back-to-back jets, the FWM are close to the theoretical prediction of alternating values of 1 and 0. The even FWM are not 1 due to the underlying event.

On the lower right corner, the values of all the events shapes are listed. Also, the p_T of the leading particle is shown. For the uniform event, the leading particle has a very low transverse momentum, while for the jetty event the leading p_T is significantly higher. This is, at least for the given examples, in good agreement with the 2 GeV/c cut used to separate hard and soft events. It is also in good agreement with the conclusions from the study shown in section 5.11.

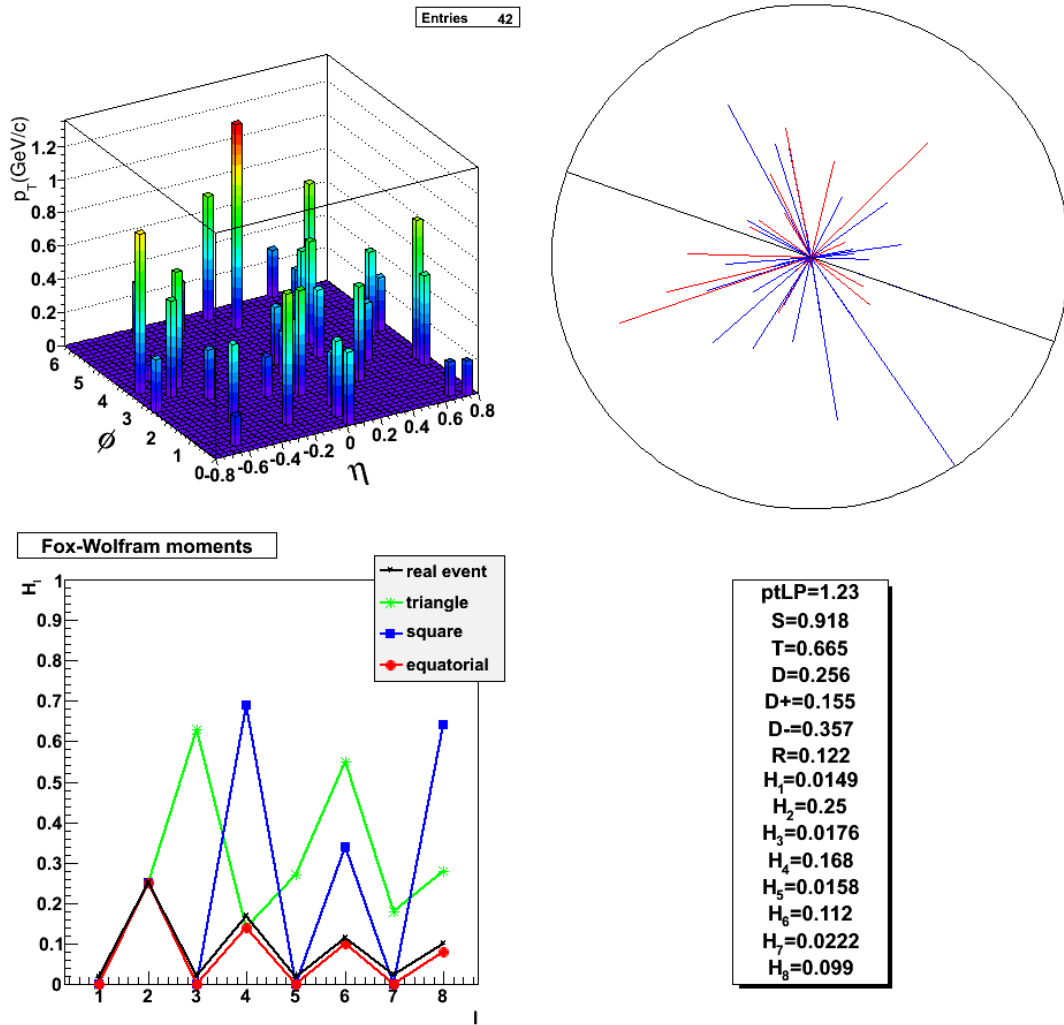


Figure 5.3: Example of a high multiplicity event ($n_{ch} = 42$) with uniform particle distribution.

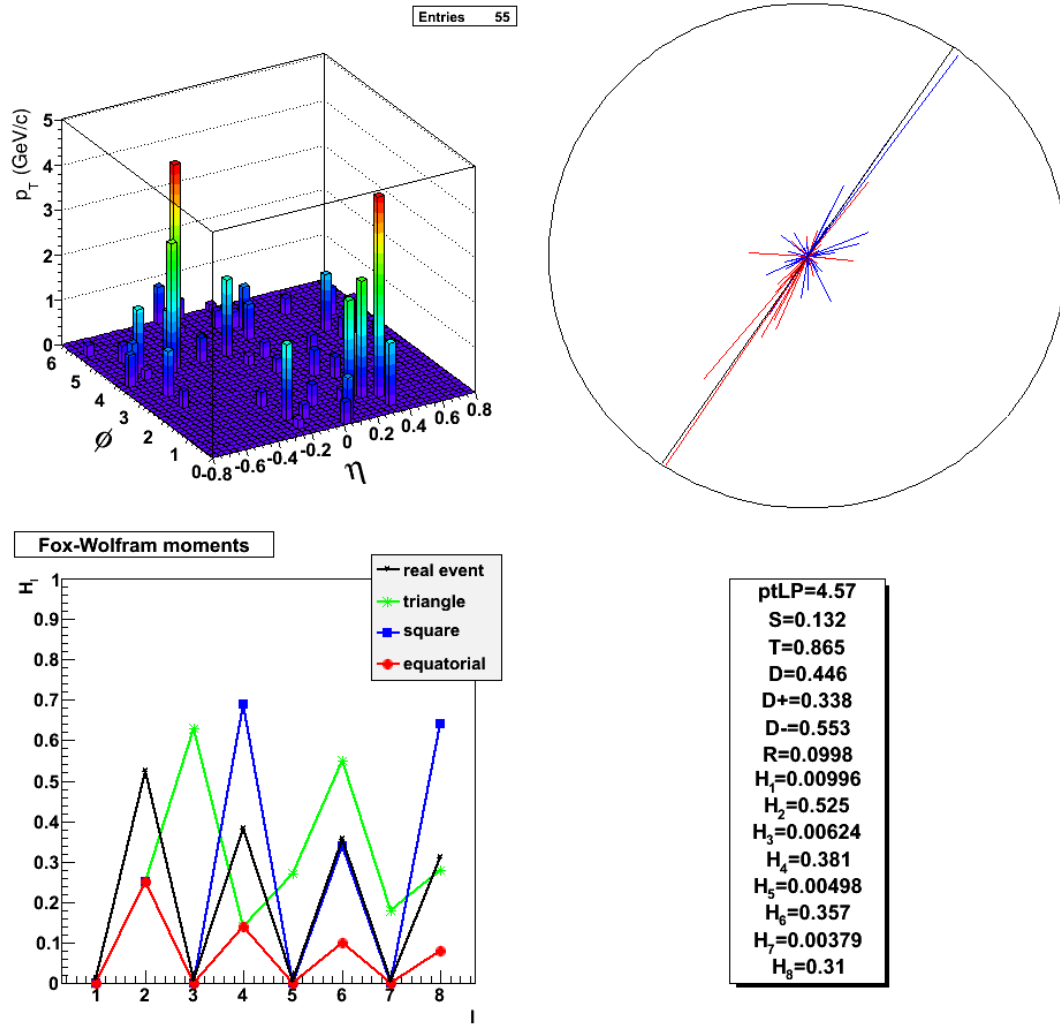


Figure 5.4: Example of a jet-like event with $n_{ch} = 55$.

5.7 Comparison with data

Event shape observables are affected by the limited efficiency of the detector which must be taken into account when analyzing data. A comparison between the reconstructed and simulated values of sphericity, thrust, directivity and recoil can be seen in Figure 5.5. All the event shape observables are rather well reconstructed. The correlation is not perfect due to limited efficiency and acceptance of the detector.

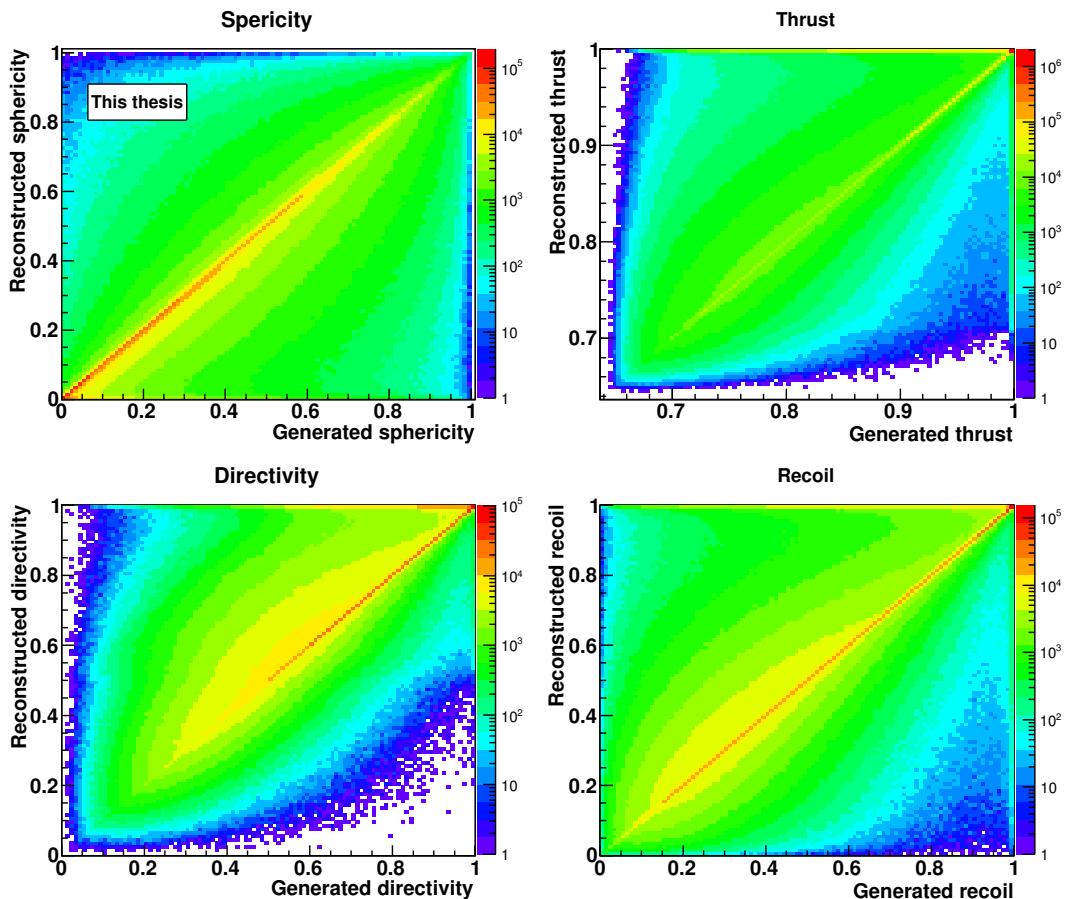


Figure 5.5: Reconstructed values for Sphericity, Thrust, Directivity and Recoil vs. the simulated values in the same Pythia events.

5.8 Study of multiplicity - event shape correlation

Another study that was made is the multiplicity dependence of the event shape observables. The four event shape observables discussed in this paper are plotted as a function of multiplicity for the reconstructed events in Figure 5.6. On top of the bi-dimensional histograms, the profile on the x axis is drawn (red line) to show the mean value for each multiplicity bin. The values from low multiplicities generally correspond to anisotropic shapes and can be understood as a low number effect, namely, it is hard to find an azimuthal isotropic distribution (both in ϕ and p_T)

when there are only few particles in the event. This is further discussed in section 5.11.2.

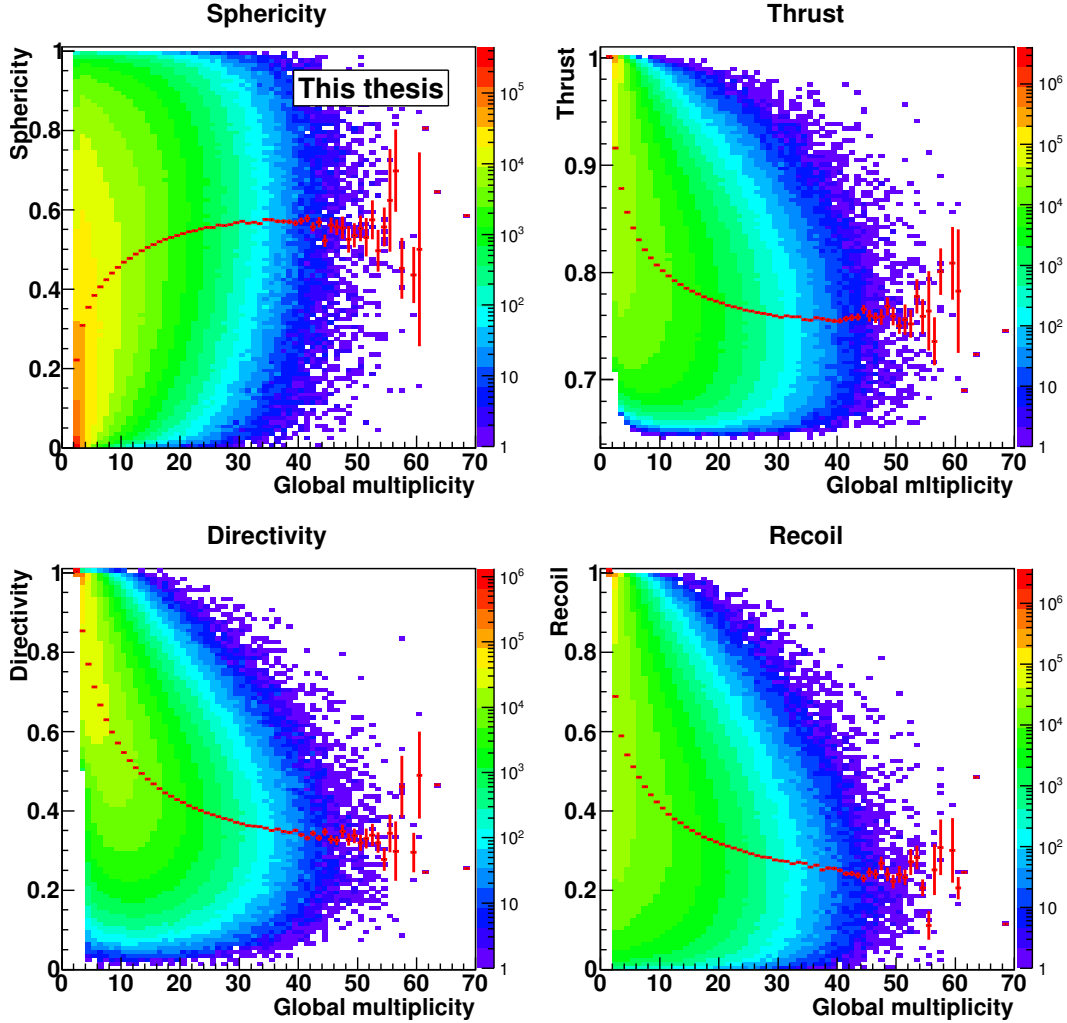


Figure 5.6: Multiplicity dependence of sphericity, thrust, directivity and recoil. With red lines, the profiles (on x axis) of the distributions are shown.

At high multiplicities, especially the Sphericity and Thrust profiles reach an almost flat plateau while the values of each observable have a rather wide range. This is actually understandable since the two extreme cases of back-to-back jets and azimuthally symmetric events are not restrained by only asking for the event to have high multiplicity.

5.8.1 Comparison with Pythia

The ratio between the profiles of the reconstructed sphericity, thrust and directivity for data and Pythia simulations are shown in Figure 5.8. For all three event shape observables, the data show a behaviour towards soft-like events for high multiplicities.

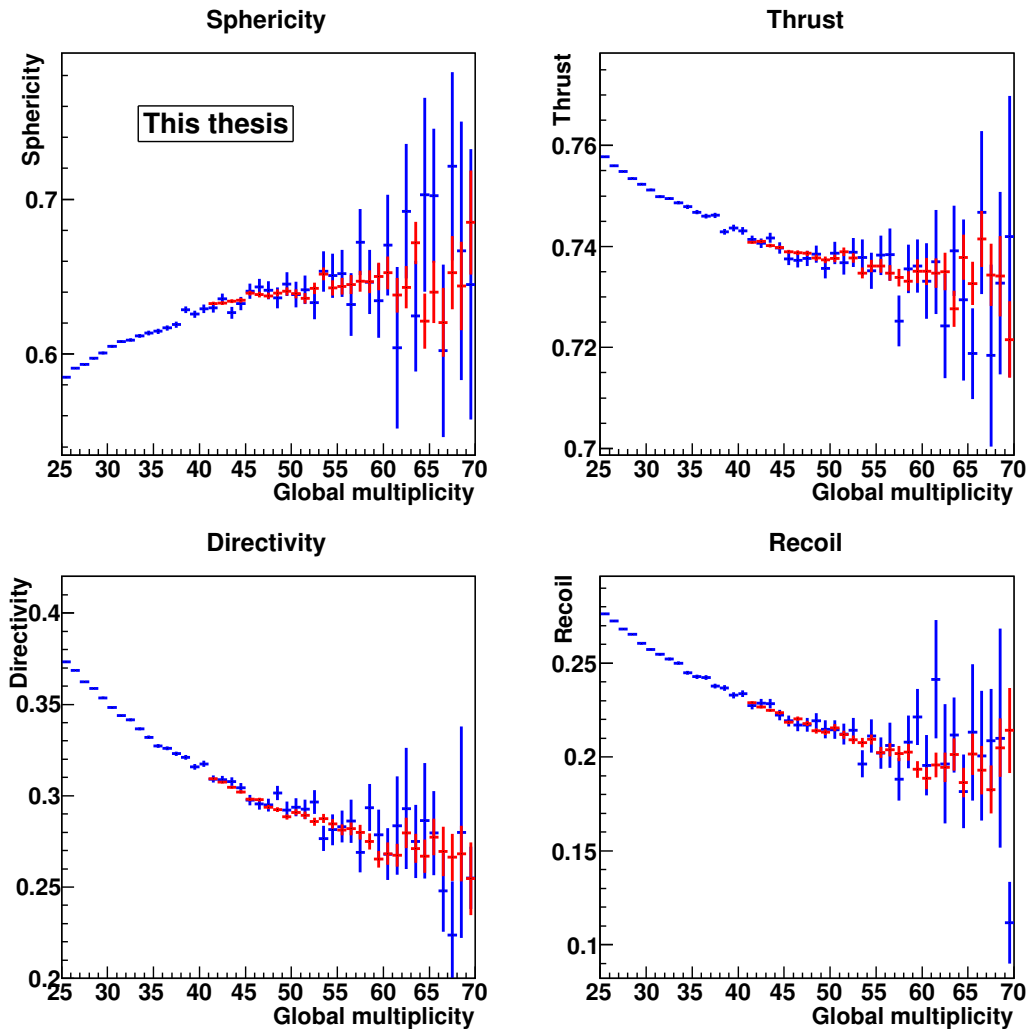


Figure 5.7: Profiles for Minimum Bias (blue) and High Multiplicity trigger (red) for sphericity, thrust, directivity and recoil.

5.8.2 Multiplicity dependence of the Fox-Wolfram moments distributions

A two dimensional dependence of each FWM on the multiplicity is plotted in Figure 5.9. One obvious feature is that all plots have some sort of a triangular shape with respect to the multiplicity. This raises the question what is the reason for this behavior? Is it that the FWM are not sensitive enough at very high multiplicities or at such high multiplicities (i.e. above 60) all the events are more or less azimuthally isotropic? To answer this question one can look at events with multiplicity greater than 60 and also at the momentum distribution of these events. The examples presented in section 5.6, along with the results on high multiplicity events from Chapter 7 clearly show that not all the high multiplicity events are labeled “soft”. Therefore, events containing jets may still be rejected, event at very high multiplicities.

A quantitative estimation of the distribution of the first eight Fox-Wolfram Mo-

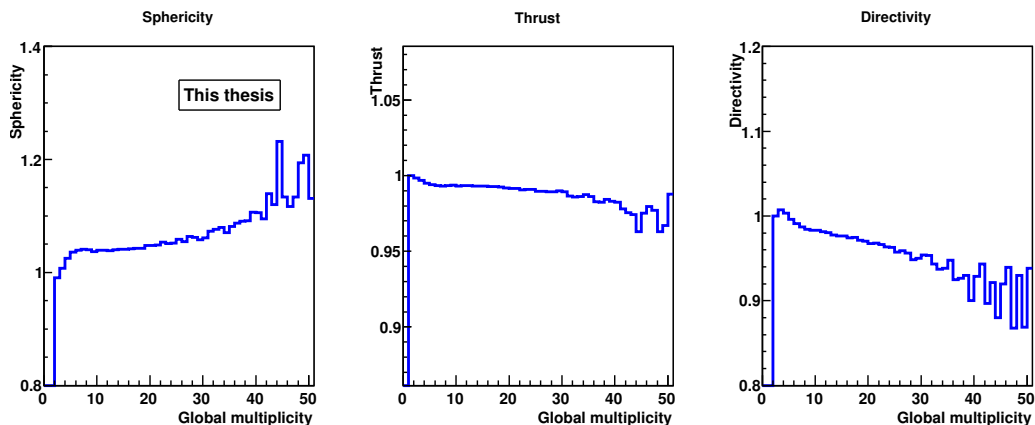


Figure 5.8: Sphericity, thrust and directivity profile ratio (for Minimum Bias) between data and Pythia simulations.

ments is plotted in Figure 5.10 for different multiplicity bins.

5.8.3 Trigger dependence

The profiles of all the event shape observables as a function of the global multiplicity show similar trends for minimum bias and high multiplicity events, as can be observed in Figure 5.7. Therefore, the analysis can also be performed on high multiplicity events.

Table 5.2: Cut values for each of the event shape observables used.

Label \ ESO	S	T	D	$H_{1,3,5,7}$	H_2	H_4	H_6	H_8
Uniform/isotropic	> 0.8	< 0.72	< 0.3	< 0.1	< 0.3	< 0.2	< 0.16	< 0.12
Non-isotropic	< 0.4	> 0.85	> 0.6	> 0.1	> 0.3	> 0.2	> 0.16	> 0.12

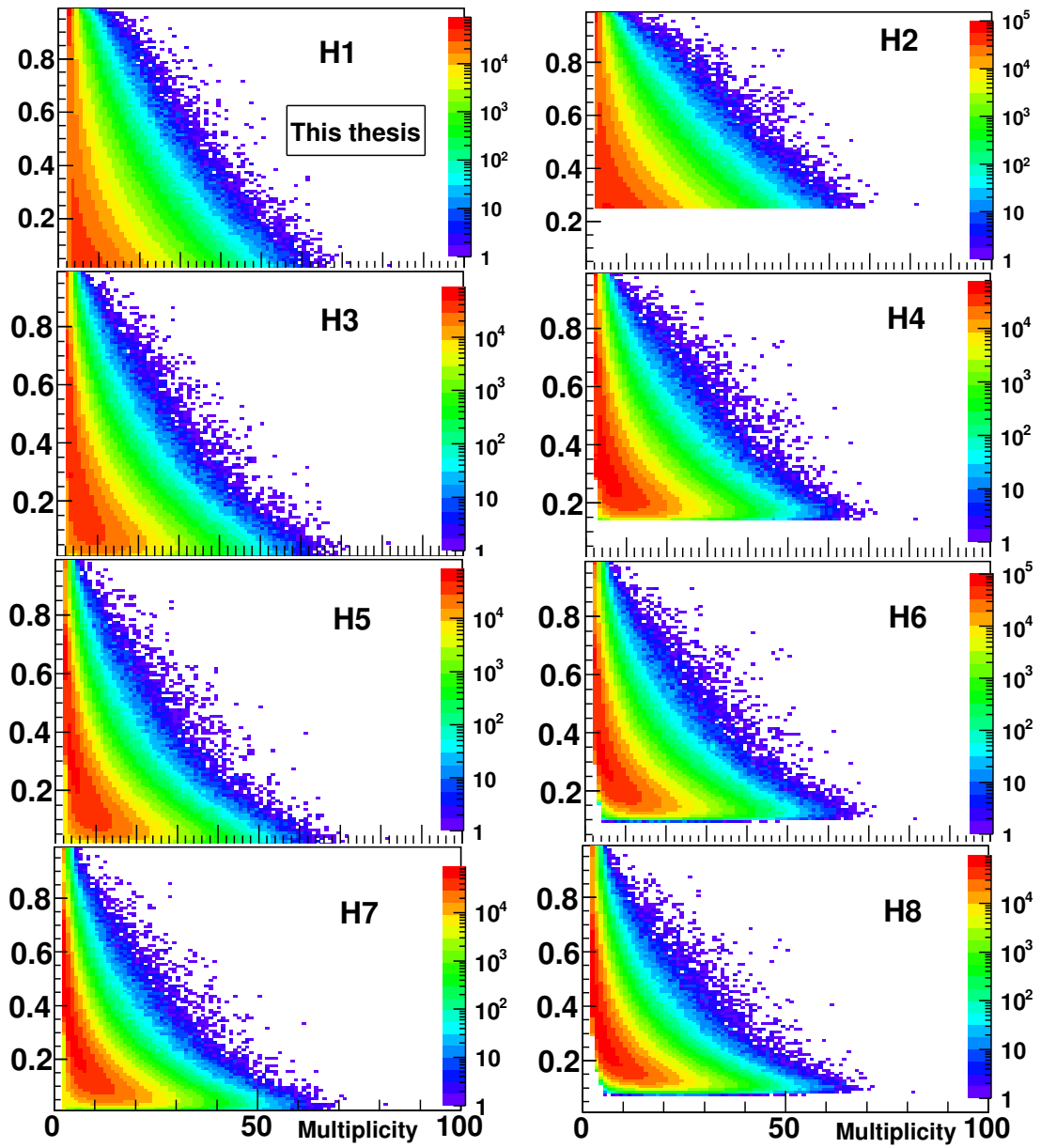


Figure 5.9: Fox-Wolfram moments multiplicity dependence.

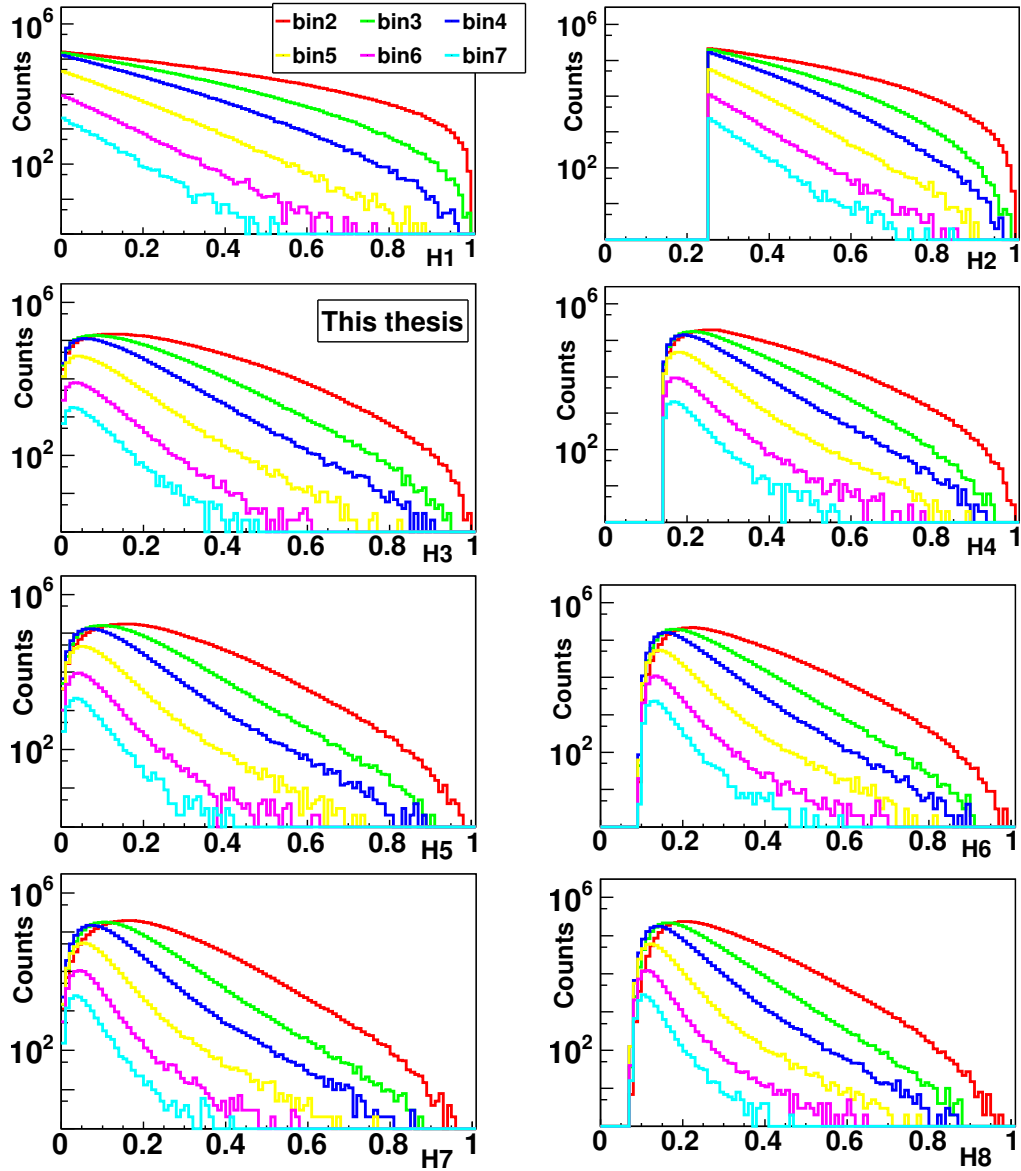


Figure 5.10: Fox-Wolfram moments yields in different multiplicity bins.

5.9 Event topology selection performance

A delicate problem raised when building azimuthal distributions in p-p collisions, is that of the origin of the representation. In heavy ion collisions, where the colliding systems have a “large” size (at least when compared with the proton), a reaction plane - RP - can be defined and flow studies are made relative to that reaction plane. In proton-proton collisions the reaction plane is not defined.

In the process of evaluating the performance of event shapes selection, one must find a general reference for the azimuthal distributions. Two possible choices were identified and used in this study. The first choice is to use as reference the leading particle. In this case, the leading particle itself was eliminated from the distribution since it will trigger an artificial peak in the origin of the distribution with no physical meaning.

The second choice for the direction taken as reference in the azimuthal distributions is the thrust axis - \vec{n}_T . Distributions with the \vec{n}_T in the origin have a physical meaning in the context of event shape analysis and need no particle elimination. The results for the azimuthally isotropic events selected with sphericity, thrust and directivity are plotted in Figure 5.11.

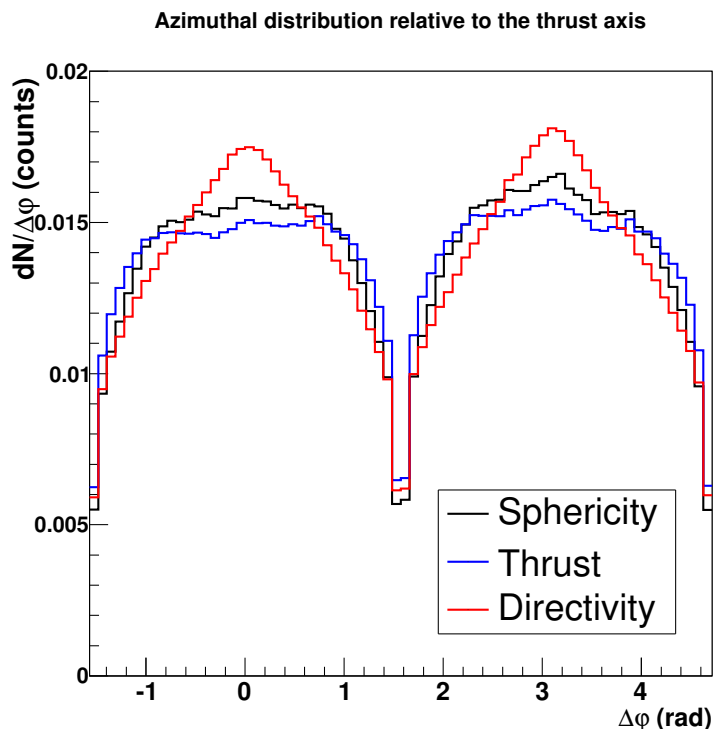


Figure 5.11: Particle distribution relative to the thrust axis \vec{n}_T for sphericity, thrust and directivity azimuthally isotropic selected events. All the distributions are normalized.

When thrust is physically very well defined, meaning that reconstruction errors have a small effect on the \vec{n}_T and the thrust has high values corresponding to confined

particle emission, most if not all the particles will be detected in the proximity of the thrust axis. The azimuthal distribution will not be flat-like but will more likely show two peaks. For the opposite situation, of azimuthally symmetric events, the thrust axis is not well defined as there is no preferential direction in space. Since the thrust axis was determined in a somewhat “unstable” manner, particles are distributed uniformly relative to the thrust axis. This will not result in a completely flat distribution since all the events have a finite multiplicity that is rather far from what we call uniform distribution. In a finite multiplicity event, the thrust axis is unlikely to be determined perpendicularly to any particle orientation due to the maximum condition in the thrust definition. Particles at 90° from \vec{n}_T have no contribution to the thrust value and are “lost” when considering the sum of p_T projections. This means that is very difficult to find particles very close to 90° from \vec{n}_T due to the thrust definition and finite event multiplicity. Hence, the resulting distribution will show two corresponding gaps at $\varphi_{\vec{n}_T} \pm 90^\circ$. This is visible for all the distributions plotted in Figure 5.11. Sphericity and thrust show a relatively flat plateau. It is worth mentioning that the azimuthal distribution by itself is not a definitive indicator of the isotropy of the event since the event shapes take into consideration the transverse momentum.

5.10 Evaluation of the event shape selection performance for the modified Fox-Wolfram moments

As mentioned, the event shape observables characterize the energy distribution in a collision. Since jets contain high p_T particles, one possible choice for the origin of the azimuthal distributions is the orientation of the particle with the highest transverse momentum in the event, the leading particle. If there is a jet in the experimental acceptance, most probably the leading particle is part of that jet and the relative azimuthal distribution will show a peak near the axis origin and also some structure in the opposite direction.

Taking into consideration that the thrust maximizes the sum of all the momenta, the uniform events should not have the thrust axis well defined, in the sense that thrust values are similar for different thrust axis orientations and only a small difference will define the final thrust value and axis in the event. One must keep in mind that all the ESO are defined using not only the orientation of the particles, but also the momentum. This means that, for example, the thrust axis can be defined by a high energy particle that will not be included in the $d^2N/\Delta\eta\Delta\phi$ representations.

5.10.1 Two particle correlations

The results for the minimum bias events are plotted in Figure 5.12, for the high multiplicity case in Figure 5.13 and the HM events selected with the FWM cuts as can be seen in Figure 5.14. The cut values used for event selection are listed in Table 5.8.3. The uniform events selected using the FWM values represent approximately 20% of the total high multiplicity events.

As expected, for the MB case, there is a clear peak near the leading particle. This peak is visible in the high multiplicity events. For the events selected with FWM cuts, there are no clear peaks in the $\frac{dN}{\Delta\phi}$ distribution within the present statistics.

The plots in the left panel represent the relative distribution of the particles relative to the LP taking into account both the azimuthal angle and the pseudorapidity. The plot in the middle is the projection of the two particle distribution on the $\delta\varphi$ axis. The right panel plot represents the two particle correlation after a uniform background has been subtracted from the signal. For the minimum bias and multiplicity greater than 40, the two particle distributions show a clear peak near the origin of the representation. The shape of the peaks for the two cases is qualitatively the same. Also, a ridge is visible at 180° relative to the leading particle.

For the high multiplicity events selected with the Fox-Wolfram moments as uniform, the results are presented in Figure 5.14. The bi-dimensional distribution nearly flat within the available statistics. There are some small non-uniformities in the unidimensional two-particle correlation (middle plot). Two regions where the profile shows a small dip are present at the origin and $\Delta\varphi = 180^\circ$. The origin of these two regions is not yet understood.

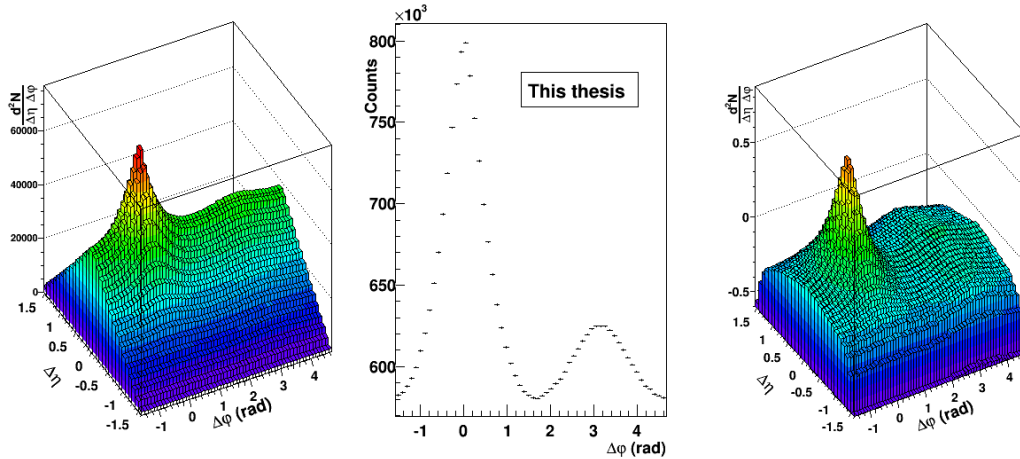


Figure 5.12: Particle distribution relative to the leading particle for minimum bias events.

The distribution represented in Figure 5.14, although it has a very low statistics and is not completely flat, gives an answer to the questions about the events with multiplicities above 60. These events, with low FWM values, do not manifest any noticeable correlation in the particle distribution relative to the leading particle. The conclusion is that most probably the very high multiplicity events included in this study are mostly uniform.

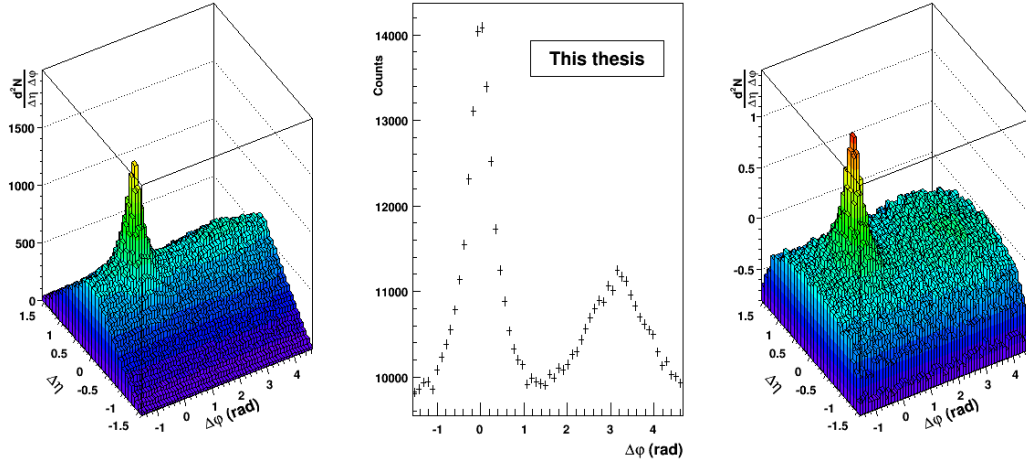


Figure 5.13: Particle distribution relative to the leading particle for high multiplicity events ($N_{ch} > 40$).

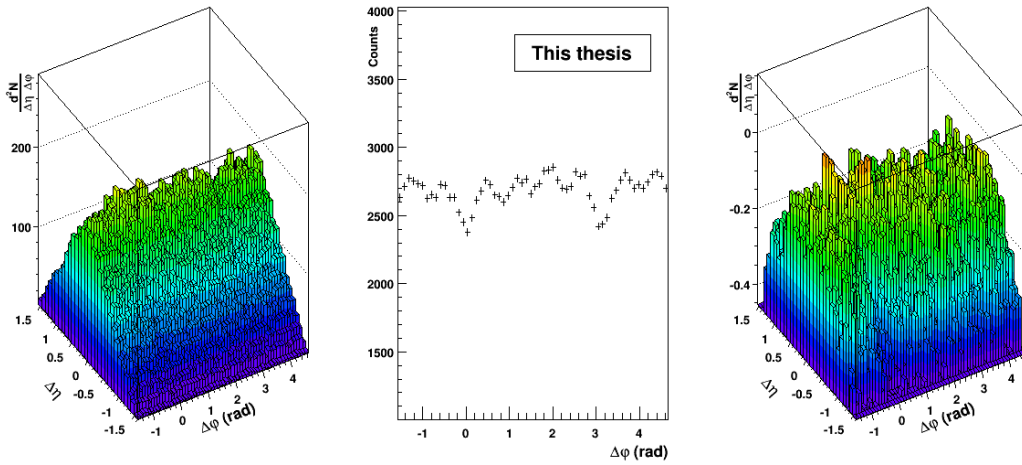


Figure 5.14: Particle distribution relative to the leading particle for high multiplicity events ($N_{ch} > 40$) and Fox-Wolfram moments selection.

5.11 Transverse momentum spectra dependence on the event shape selection

A simple toy model using N particles with the same momentum magnitude distributed equidistant in azimuth was used to study the event shape phenomenology in [Banfi2010]. In Figure 5.15, the results from [Banfi2010] are reproduced for sphericity and thrust. This model is not well adapted for the purpose of this analysis and a different approach is necessary. The main question is what happens with the shape of the spectra when events are selected using a given event shape observable. The way this problem was approached by generating particles with momentum values corresponding to a certain p_T distribution for different multiplicities. Then, the particles were randomly spread in the transverse plane and the shape modification of the spectra was investigated for different event shape cuts and multiplicities.

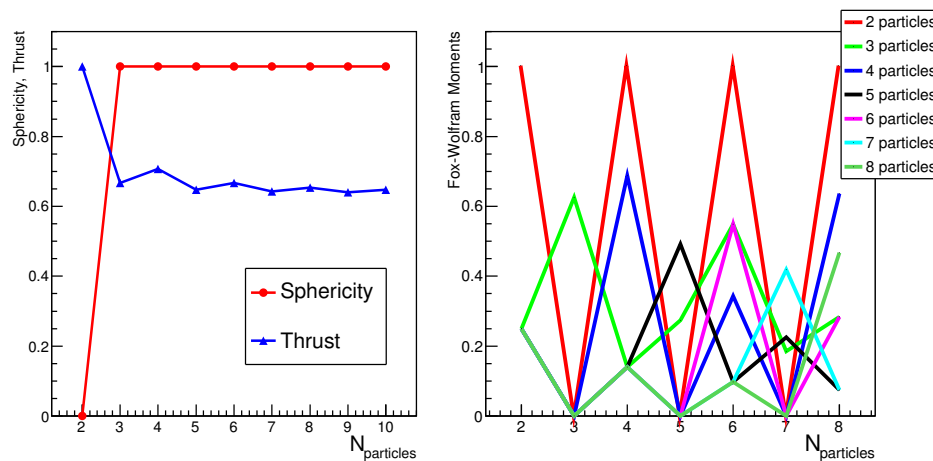


Figure 5.15: Sphericity and thrust (left) and FWM(right) for N equidistant particles.

The random generation of the p_T values was done according to Boltzmann (eq. (2.2)), Boltzmann-Gibbs Blast Wave (eq. (2.5)) and Tsallis Blast Wave (eq. (2.8)) parameterizations used in high energy physics and discussed in Chapter 2.

The value of the mass considered in the calculations is the mass of the charged pions ($139.6 \text{ MeV}/c^2$). The values used for the parameters are listed in Table 5.3 and correspond to the values from [Petrovici2009] [Andrei2009].

Table 5.3: The parameters used for p_T distribution random generation.

Model \ Parameter	Temperature (MeV)	β	q
Boltzmann	170	-	-
Blast-wave	110	0.6	-
Tsallis	70	0	1.15

The simulated Monte Carlo events were selected using each of the event shape observables. The spectra for the “uniform” and for “all but uniform” events are

plotted on top of the original simulated spectra in the first column of each of the Figures 5.16 - 5.19 for thermal distribution, Figures 5.20 - 5.23 for the Boltzmann-Gibbs Blast Wave model and Figures 5.24 - 5.27 for the Tsallis distribution. The rows correspond to multiplicity values of 5, 10, 20, 40 and 60 from top to bottom. In the second column the ratios between the selected uniform and non-uniform spectra to the original one are plotted.

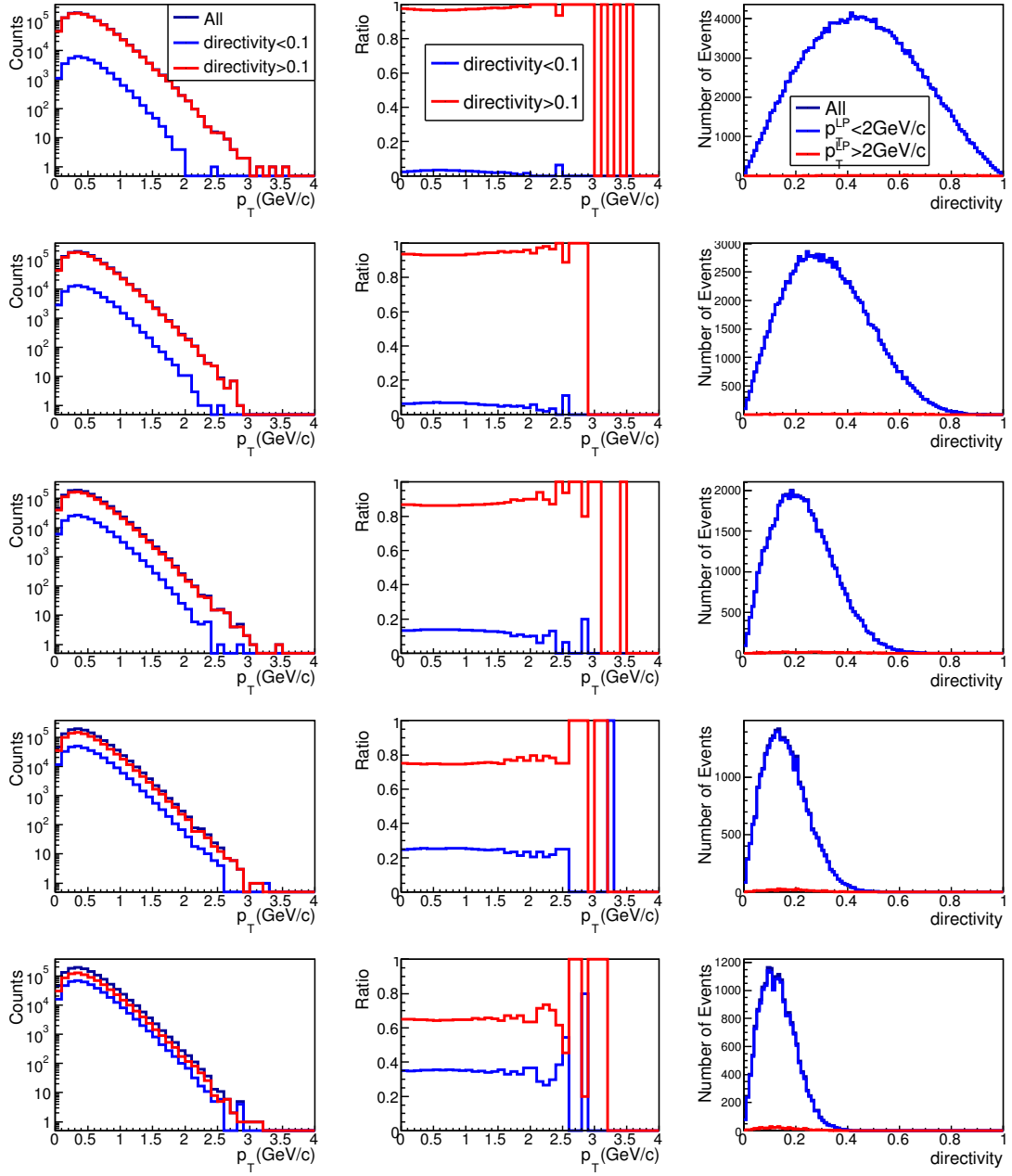


Figure 5.16: Directivity selection on random thermal simulated distribution. The rows correspond to multiplicity values of 5, 10, 20, 40 and 60 from top to bottom.

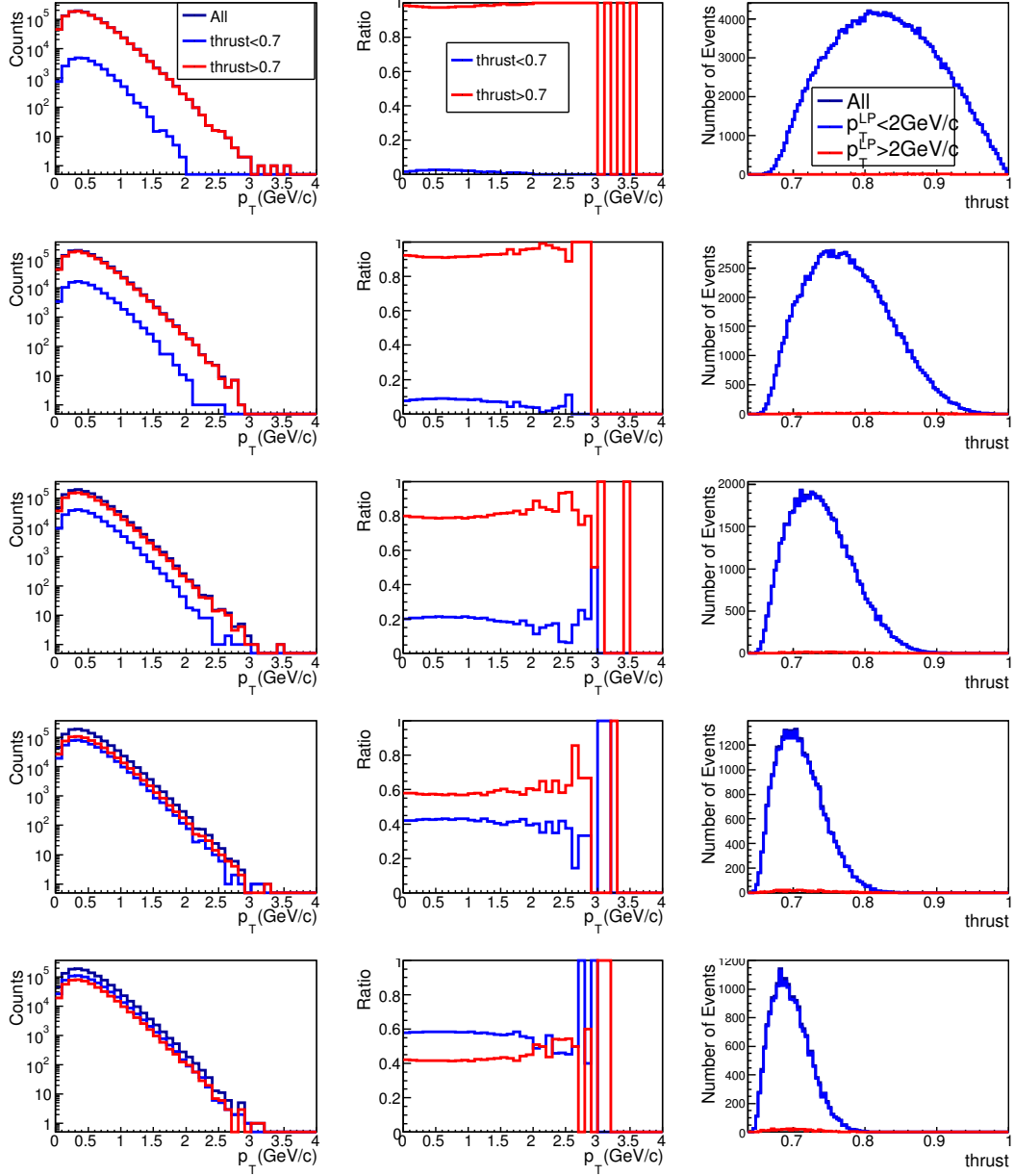


Figure 5.17: Thrust selection on random thermal simulated distribution. The rows correspond to multiplicity values of 5, 10, 20, 40 and 60 from top to bottom.

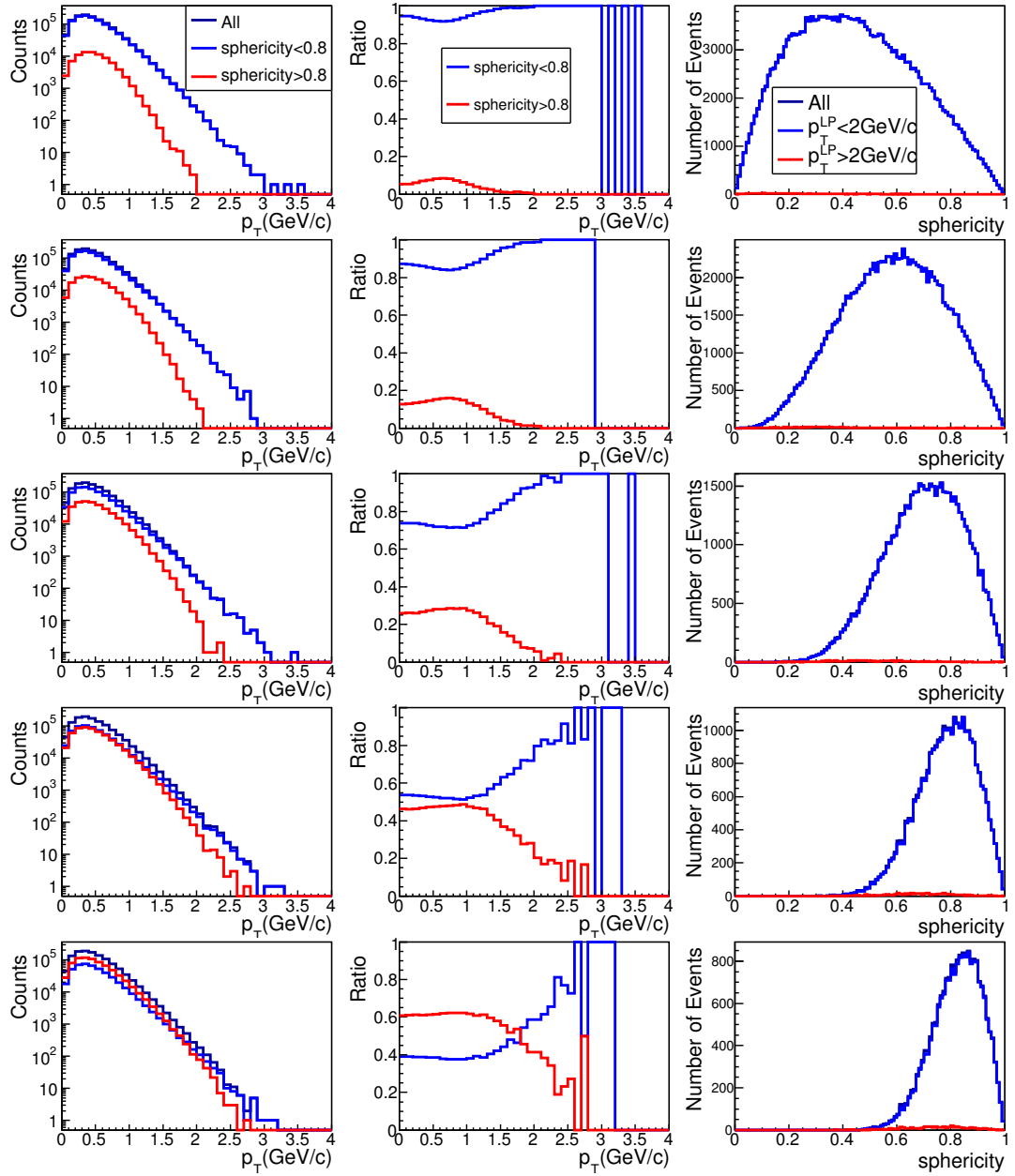


Figure 5.18: Sphericity selection on random thermal simulated distribution. The rows correspond to multiplicity values of 5, 10, 20, 40 and 60 from top to bottom.

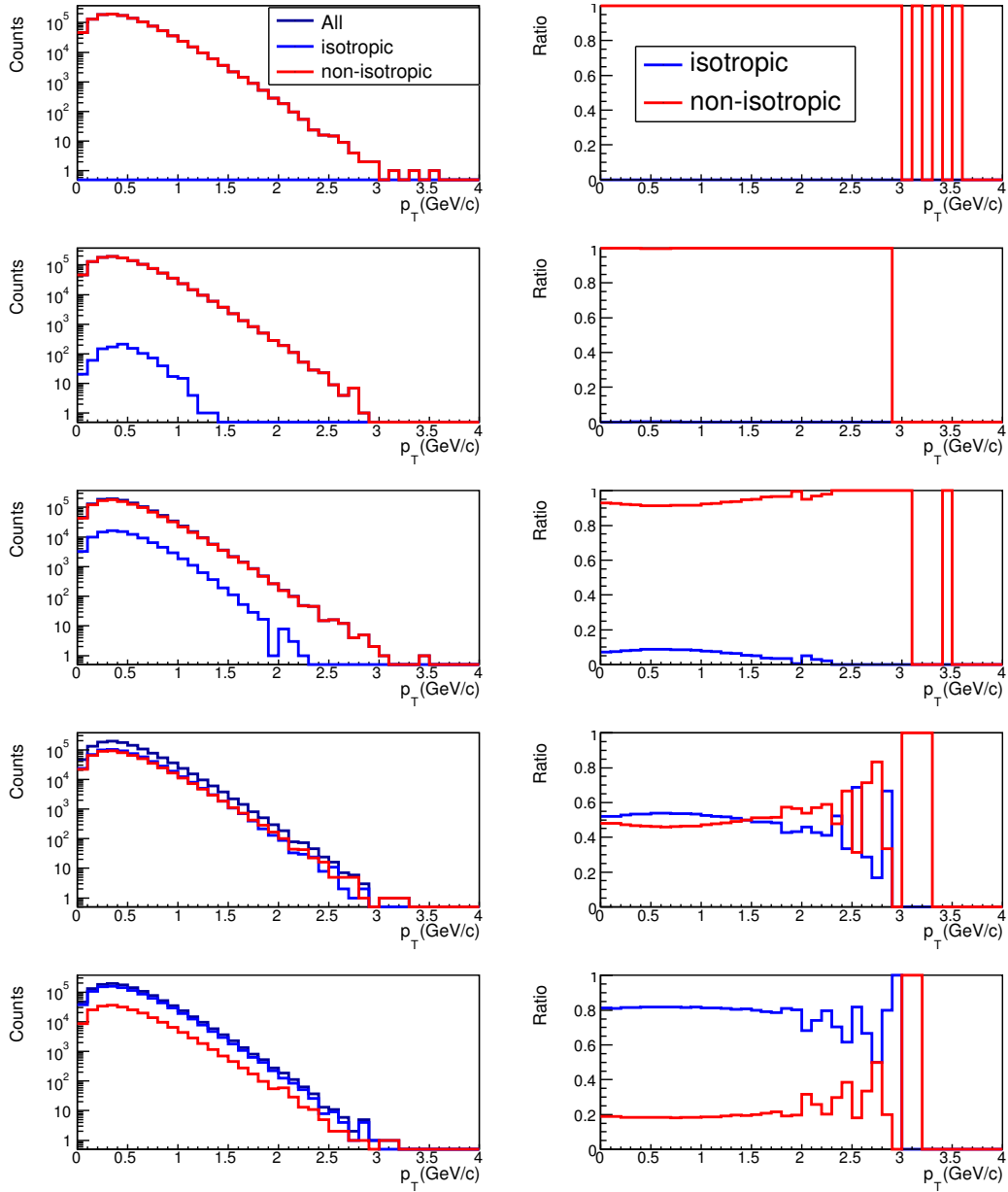


Figure 5.19: Fox-Wolfram moments selection on random thermal simulated distribution. The rows correspond to multiplicity values of 5, 10, 20, 40 and 60 from top to bottom.

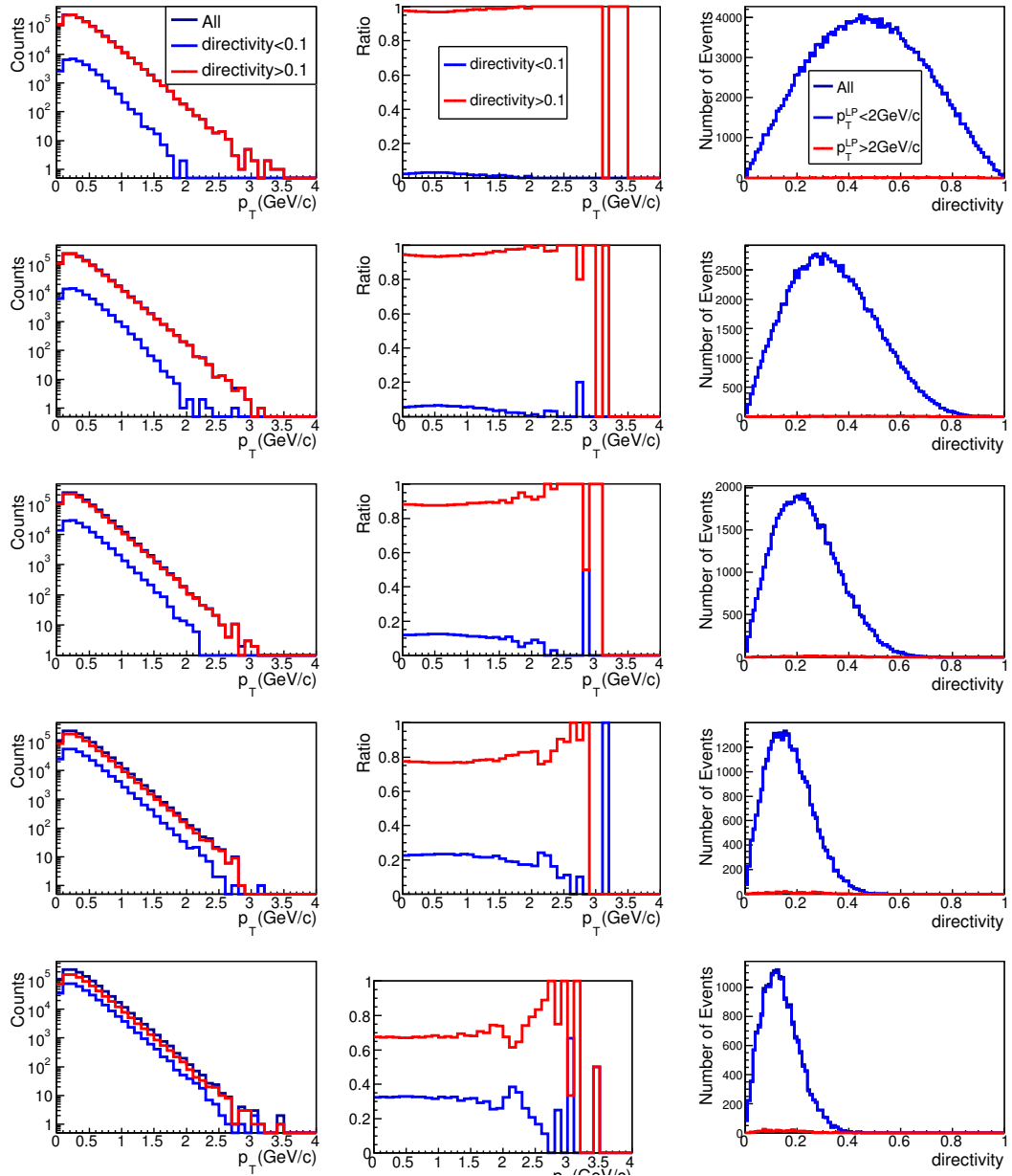


Figure 5.20: Directivity selection on random Boltzmann-Gibbs blast wave simulated distribution. The rows correspond to multiplicity values of 5, 10, 20, 40 and 60 from top to bottom.

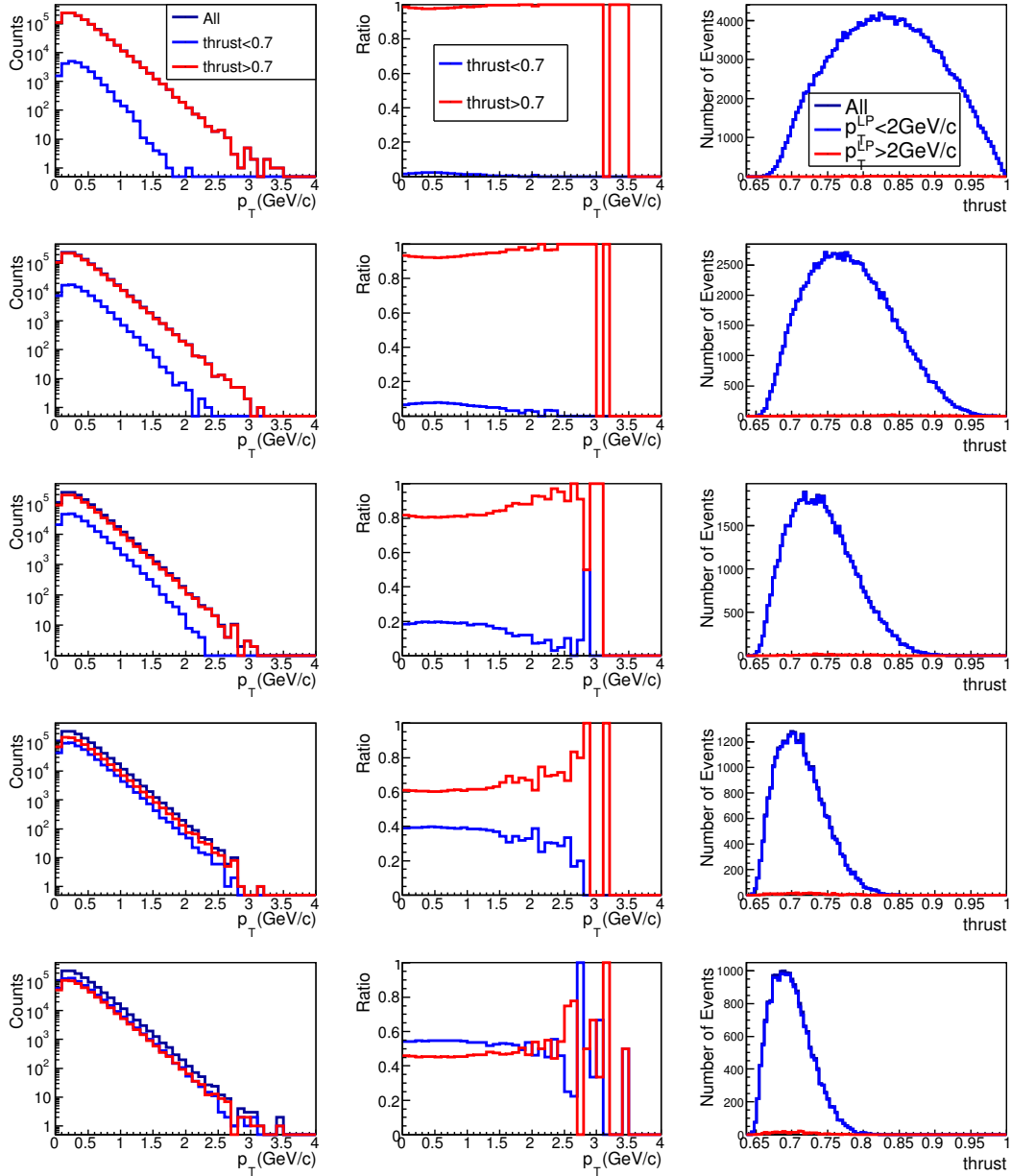


Figure 5.21: Thrust selection on random Boltzmann-Gibbs blast wave simulated distribution. The rows correspond to multiplicity values of 5, 10, 20, 40 and 60 from top to bottom.

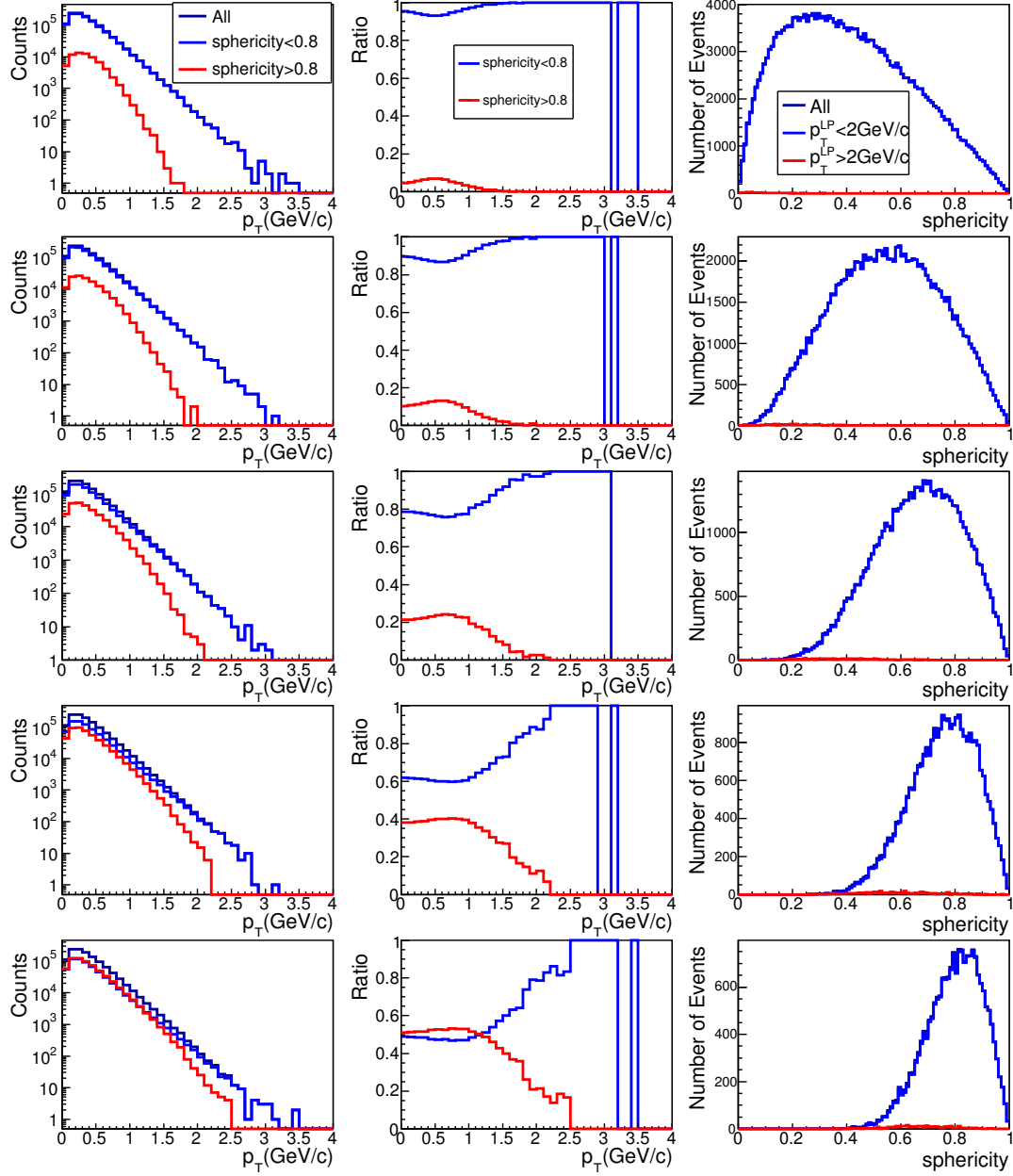


Figure 5.22: Sphericity selection on random Boltzmann-Gibbs blast wave simulated distribution. The rows correspond to multiplicity values of 5, 10, 20, 40 and 60 from top to bottom.

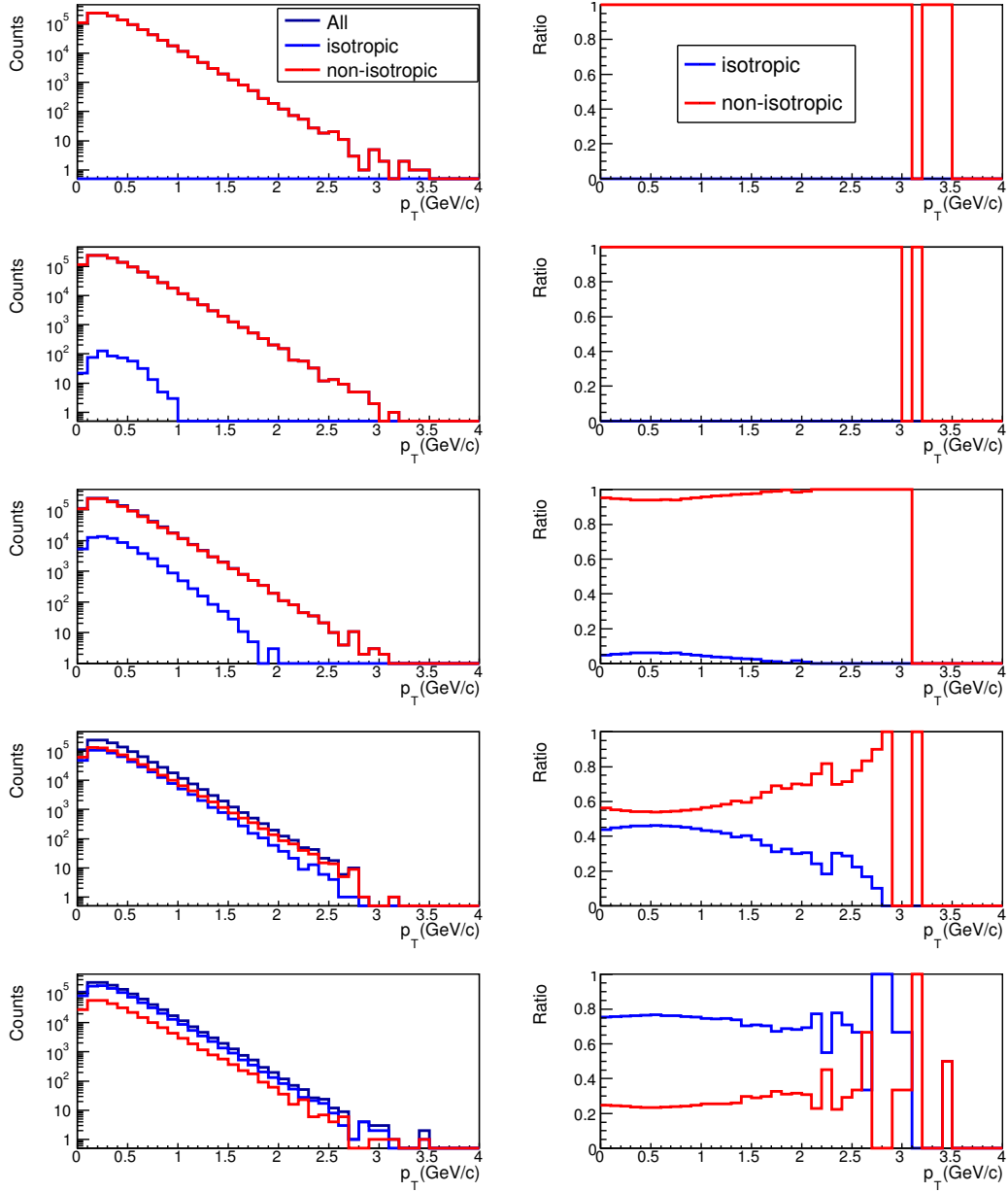


Figure 5.23: Fox-Wolfram moments selection on random Boltzmann-Gibbs blast wave simulated distribution. The rows correspond to multiplicity values of 5, 10, 20, 40 and 60 from top to bottom.

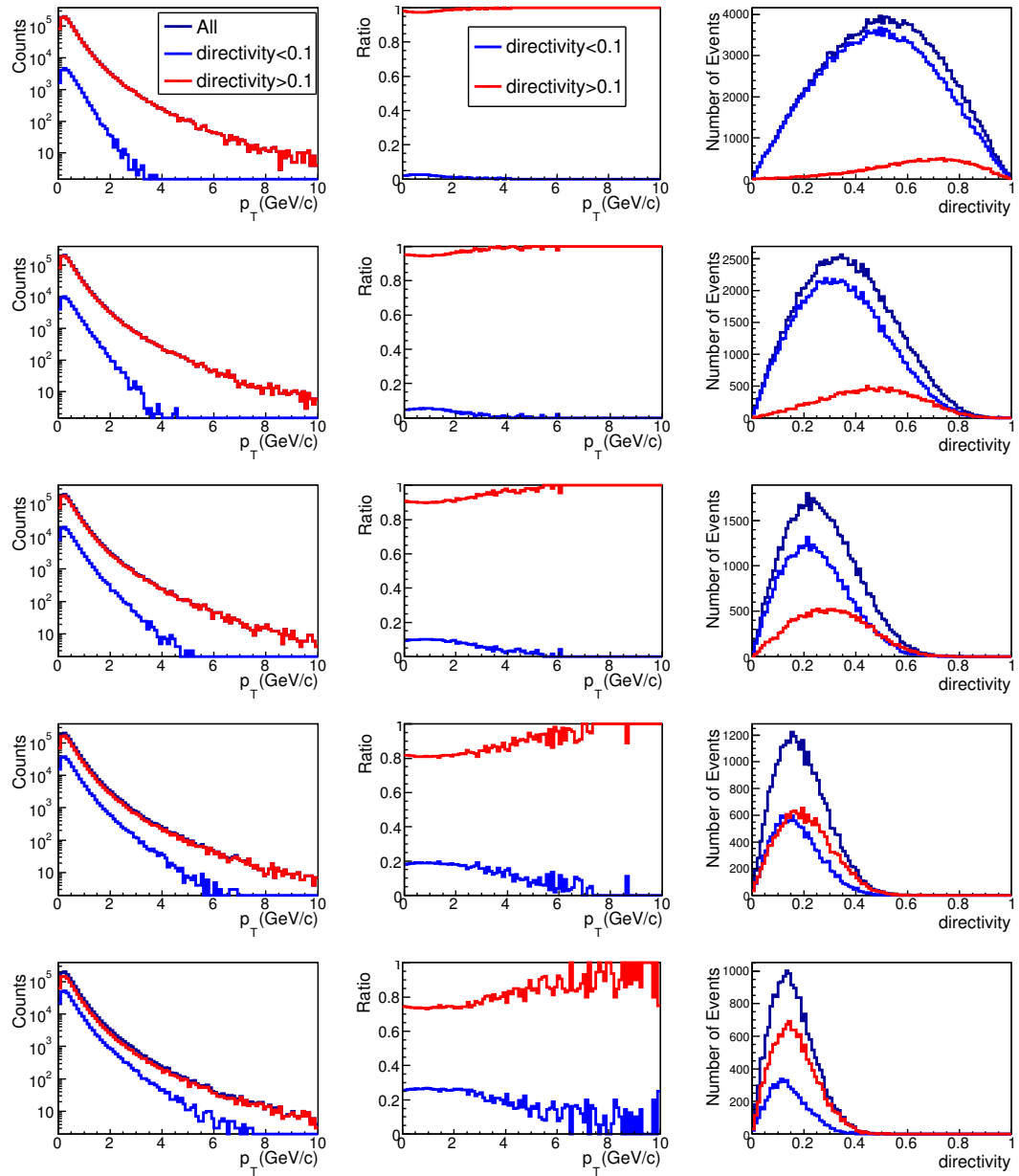


Figure 5.24: Directivity selection on random Tsallis simulated distribution. The rows correspond to multiplicity values of 5, 10, 20, 40 and 60 from top to bottom.

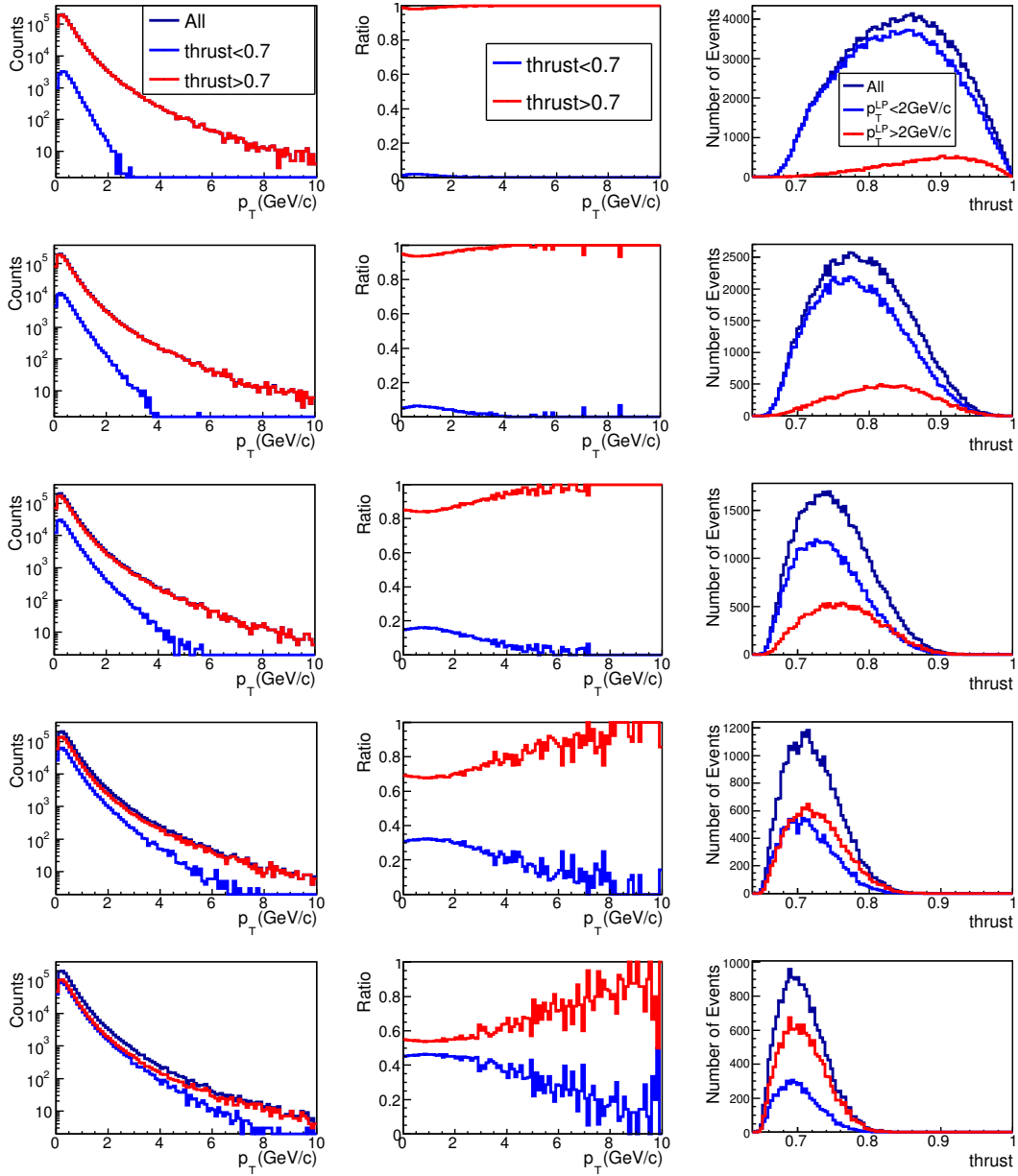


Figure 5.25: Thrust selection on random Tsallis simulated distribution. The rows correspond to multiplicity values of 5, 10, 20, 40 and 60 from top to bottom.

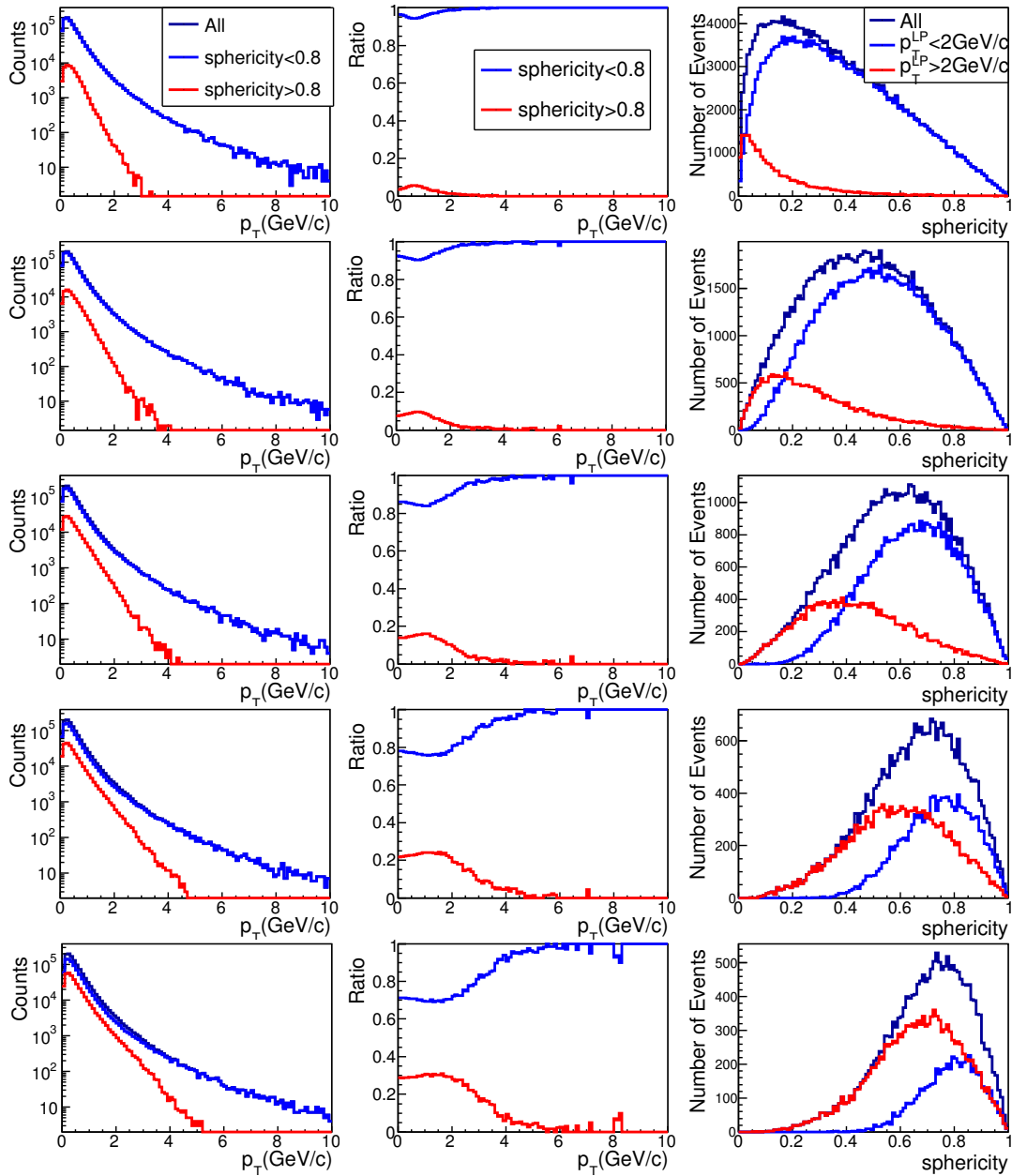


Figure 5.26: Sphericity selection on random Tsallis simulated distribution. The rows correspond to multiplicity values of 5, 10, 20, 40 and 60 from top to bottom.

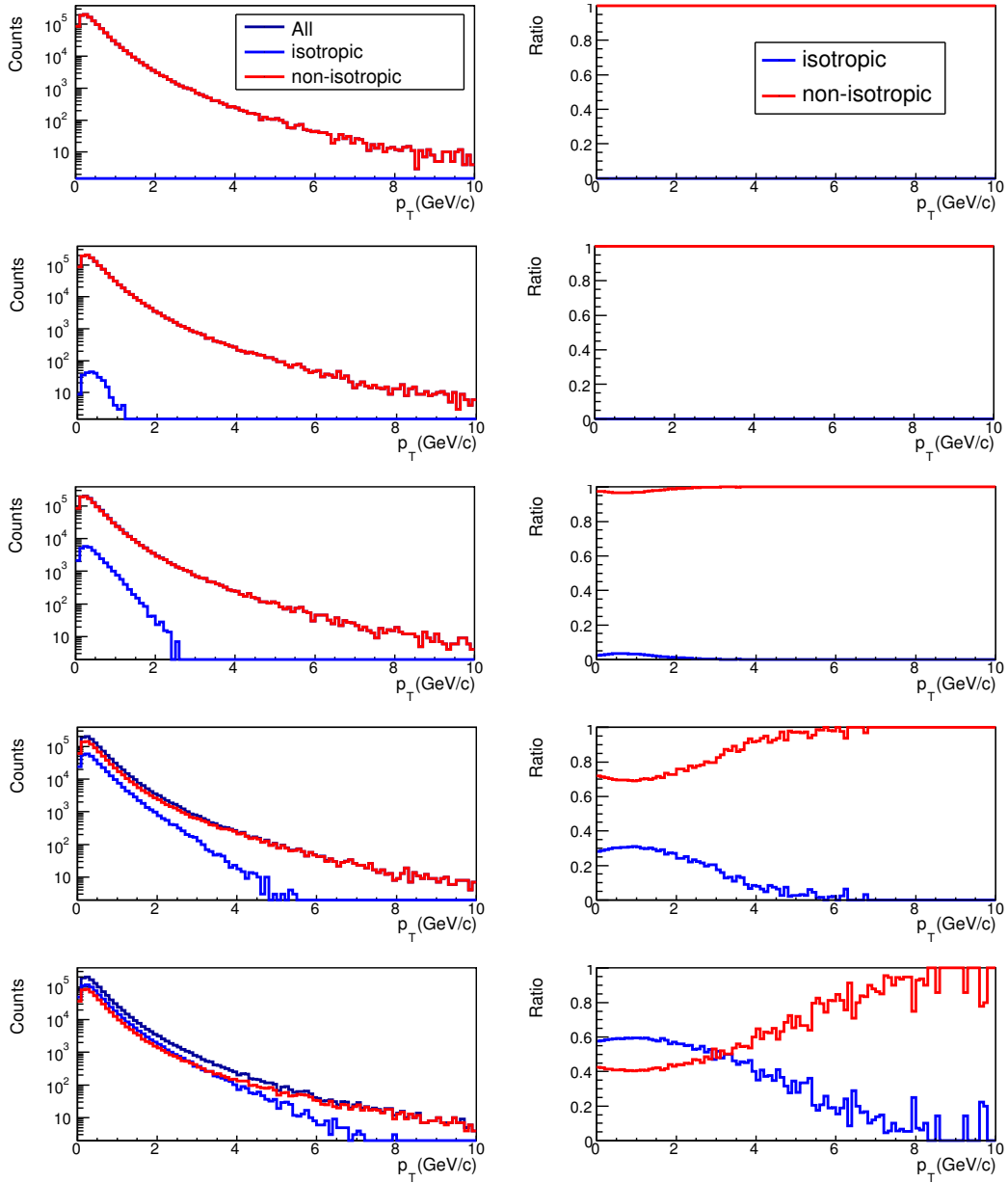


Figure 5.27: Fox-Wolfram moments selection on random Tsallis simulated distribution. The rows correspond to multiplicity values of 5, 10, 20, 40 and 60 from top to bottom.

All the event shapes cuts used introduce a bias in the spectrum depending on the multiplicity and the original spectrum. The conclusion of this study is that no p_T distribution (at least those used here) randomly spread in the azimuth can be reconstructed after any event shape cut. For high multiplicity values the bias introduced by the selection cut is smaller than for the low multiplicities but, obviously present, even for multiplicity values at the end of the ALICE Central Barrel experimental range (see section 4.2). It is worth mentioning that the bias is event shape dependent. One possible qualitatively partial explanation of this bias may be given by the results from section 5.11.2 where events with few evenly spread particles with same momentum are selected by sphericity and thrust as uniform. Many particles with similar values of momentum are improbable to be generated in the high p_T range of the spectrum. Hence, the low p_T values are more probable to be found in events selected as uniform. More extensive studies are needed in order to improve this simplistic explanation which does not explain reasonably the spectra distortion after FWM selection. A more realistic explanation would consider non-equidistant particles as in Figure 5.34. For this toy model four particle events with relatively close p_T values oriented in a plus shape pass the uniformity test. Further study of simple toy models may reveal that special configurations of a small number of particles require close values of transverse momentum for each of the particles and also spatial orientation that produces the mathematical conditions for selecting the event.

The event shape observables are used in this thesis for soft event selection. The evaluation of the selection can be done using a formula that simultaneously fits the both regions. The ratio of the two soft and hard contributions can be evaluated from the two distinct parts of the formula after a fit is performed. In this thesis, the Bylinkin-Rostovtsev (eq. 7.3) formula is used for this task. The first part of the formula corresponds to the thermal part of the spectrum, specific for soft processes. The second part is a power law distribution and is well adapted for the high p_T region. The event shape selection eliminates almost completely the hard component but it also modifies the shape of the soft spectrum.

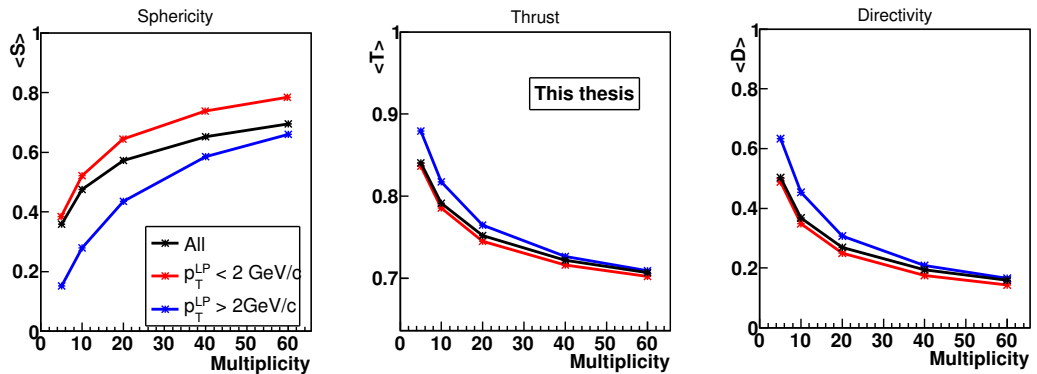


Figure 5.28: Mean sphericity (left), thrust (middle) and directivity (right) for all (black), soft (blue) and hard (red) events. The soft and hard events are identified according to the leading particle transverse momentum.

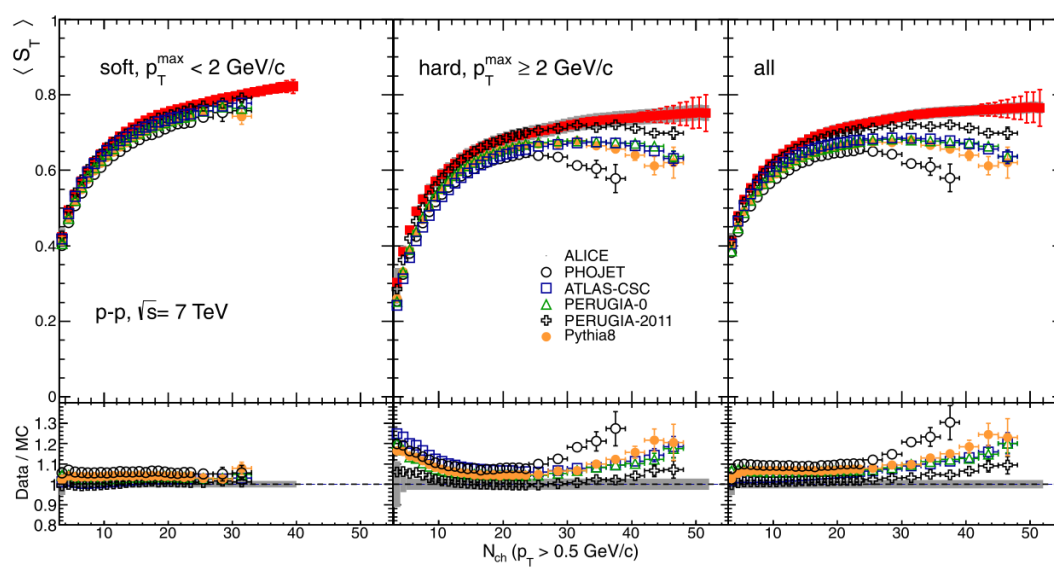


Figure 5.29: Mean sphericity for “soft” (left), “hard” (middle) and all events (right). The soft and hard are identified according to the leading particle transverse momentum. Picture from [ALICE2012b].

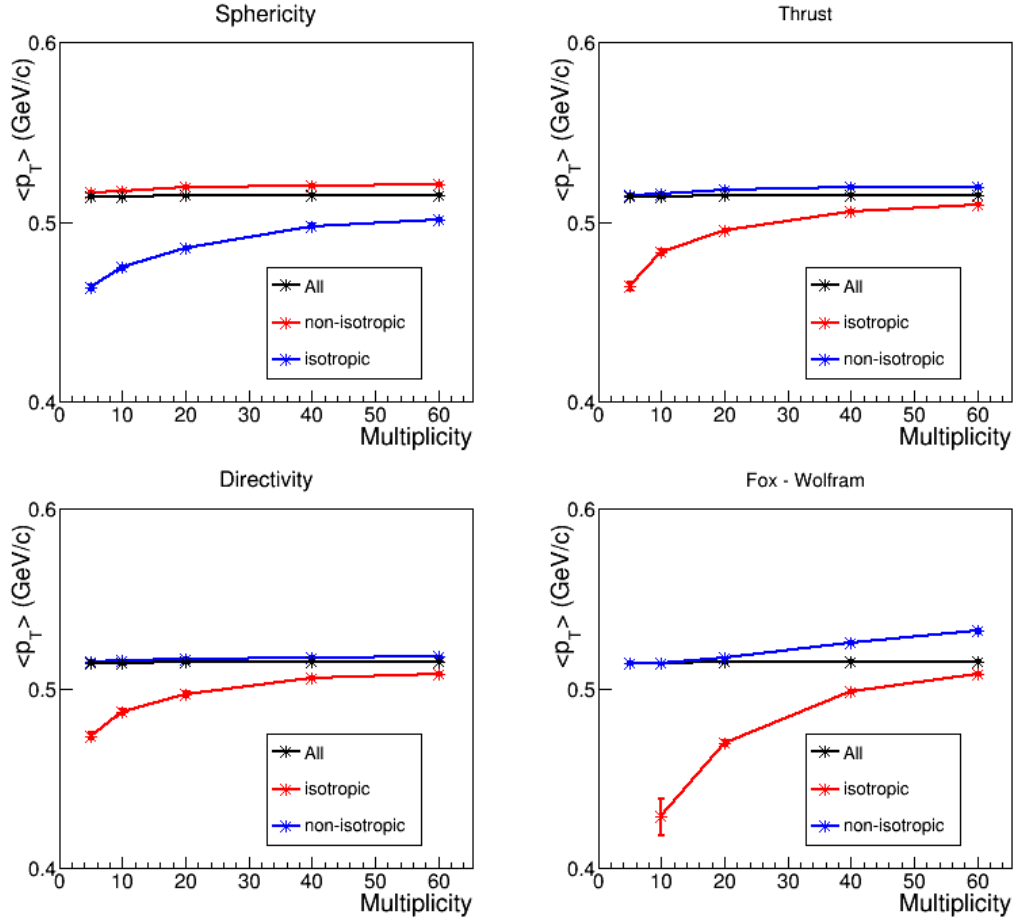


Figure 5.30: Mean transverse momentum as a function of multiplicity for isotropic and non-isotropic events selected with sphericity, thrust, directivity and Fox-Wolfram moments.

The mean transverse momentum for the events selected with sphericity, thrust, directivity and Fox-Wolfram moments is plotted in Figure 5.30. For the generated distribution (black line) the mean p_T is obviously constant by construction. For the isotropic events, the mean transverse momentum increases with the multiplicity. This effect is due to the selection process that allows more high p_T particles into the data sample for high multiplicity events. This is visible in the spectra variation from Figures 5.24-5.27 where at low multiplicities the isotropic events do not contain high p_T particles.

5.11.1 Isotropic events in Pythia

The p_T spectra for the two extreme regions in the event shape observables are represented in Figure 5.31. The events are selected as uniform or non-uniform by using the cuts listed in Table 5.8.3.

For all the spectra presented, the tail of the distribution for the jet-like events is above the tail for uniform events, all the ESO cutting events with high p_T , in

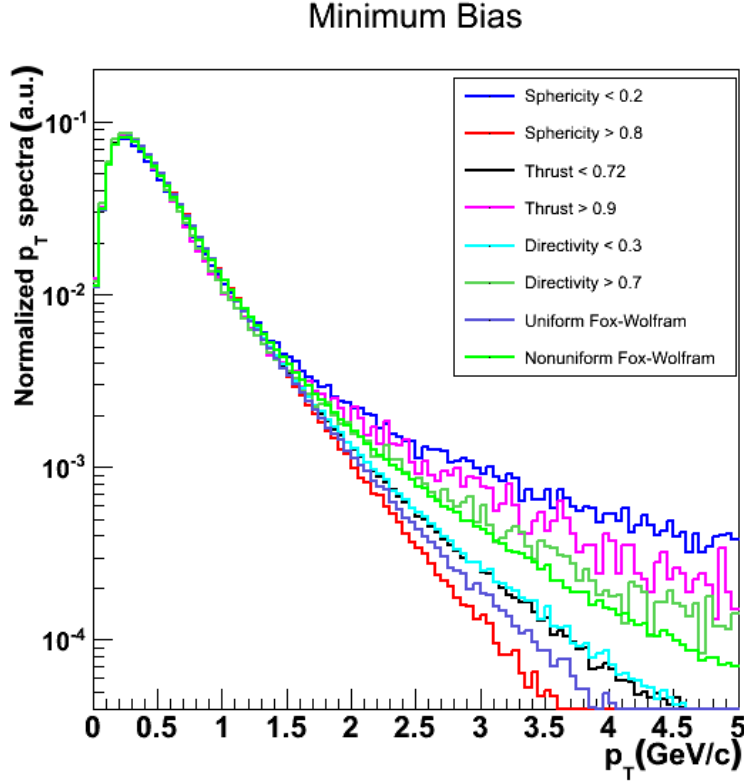


Figure 5.31: Pythia simulation of p_T spectra for uniform and jet-like events for all event shape observables. The cuts used are listed in Table 5.8.3.

accordance with the results from the previous section. It is not clear if combined event shape cuts should be used.

A high number of particles will allow a wider phase space occupancy and a smaller spectra bias, as shown by the results in the section 5.11. In the same time, the ATLAS results [ATLAS2011b] shown in Figure 5.32 suggest that the number of jets decreases rapidly, with almost an order of magnitude at each step. Events with more than four jets are considered rare.

Using the same simulations another investigation was made regarding the event shapes distributions. First, all the event shape profiles plotted in the third column (in Figures 5.16 - 5.27) roughly reproduce the multiplicity dependence trend seen for the real data or Pythia simulations. Second, sometimes the “hard” and “soft” components are labeled as such according to the momentum of the leading particle in the event. The usual cut used is $p_T^0 = 2$ GeV/c [ALICE2012b]. Since the event shape selection will cut the tail of the p_T spectra and the momentum of the leading particle will have a lower value, a cut in p_T^{LP} will change the event shape distribution. For example, a high value cut in sphericity will select events with low p_T^{LP} of the leading particle, but also a low p_T^{LP} will select higher sphericity values, although, the two selections are not *a priori* equivalent. The mean of the event shape distribution is affected accordingly. The normalized event shape distributions with the p_T^{LP} cut are shown in the third column of the previous plots. For low multiplicities a

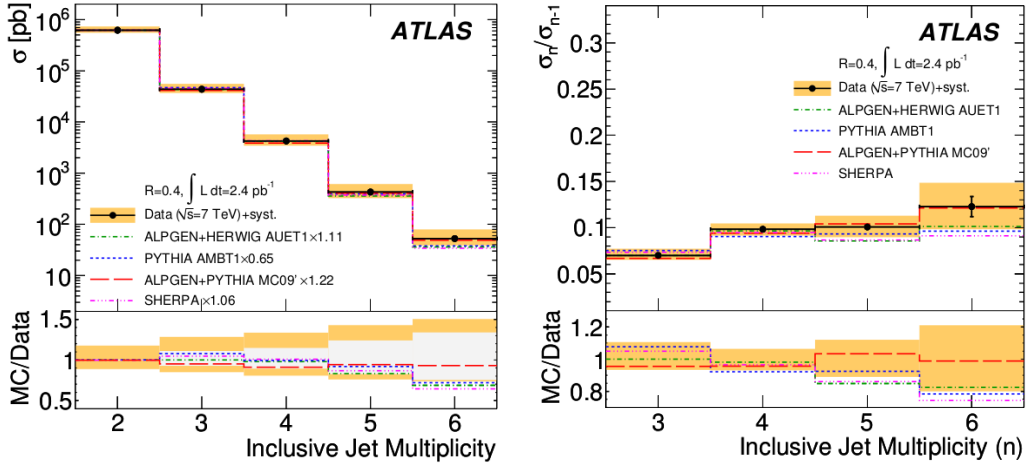


Figure 5.32: ATLAS results on multi-jet cross-section. In the left panel, the ratio between the cross-section for n and $n+1$ jets is plotted. Figures from [ATLAS2011b].

clear separation between the two classes is present. The mean of the distributions for “hard” and “soft” components and minimum bias for sphericity, thrust and directivity are shown in Figure 5.28. Sphericity averages are compared with those obtained in ALICE (Figure 5.29). Events for Boltzmann-Gibbs blast wave and thermal models have low p_T^{LP} values and only few events are labeled as “hard”.

Another toy model was used for the three jet events. Again, the jets are approximated by particles. The scan of the phase-space was done relative to one particle with $p_T^0 = 1$ a.u., fixed in the origin $\varphi = 0$. All other momenta are considered as a fraction of the reference p_T . Instead of randomly distributing the other two particles, one of them scans the p_T range from 0 to p_T^0 and is oriented from 0 to π relative to the reference particle. The third particle is orientation and momentum are computed in order to fulfill the momentum conservation. Since this toy model uses three particles, H_6 was also computed. Figure 5.33 shows sphericity, thrust, H_2, H_3, H_4 and H_6 for three particles events.

Similar to the four jets toy model, in this case, special configurations of the momenta and also the orientation of the particles are required for the events to be considered uniform. While in the case of jets this means that most probably high energy jets will be rejected, in the case of “normal” particles it means that events with low number of particles have a small chance to be selected as uniform, regardless of the momenta of the particles. This means that soft events will be rejected unless a very narrow configuration in the (p_T, φ) phase space is reached. This phase space study is not trivial to extend to higher multiplicities. A more suitable approach is the one described in section 5.11.

5.11.2 Multiple jets

The model using N equidistant particles mentioned above cannot be used for transverse momentum studies since all particles have the same momentum. Nonetheless,

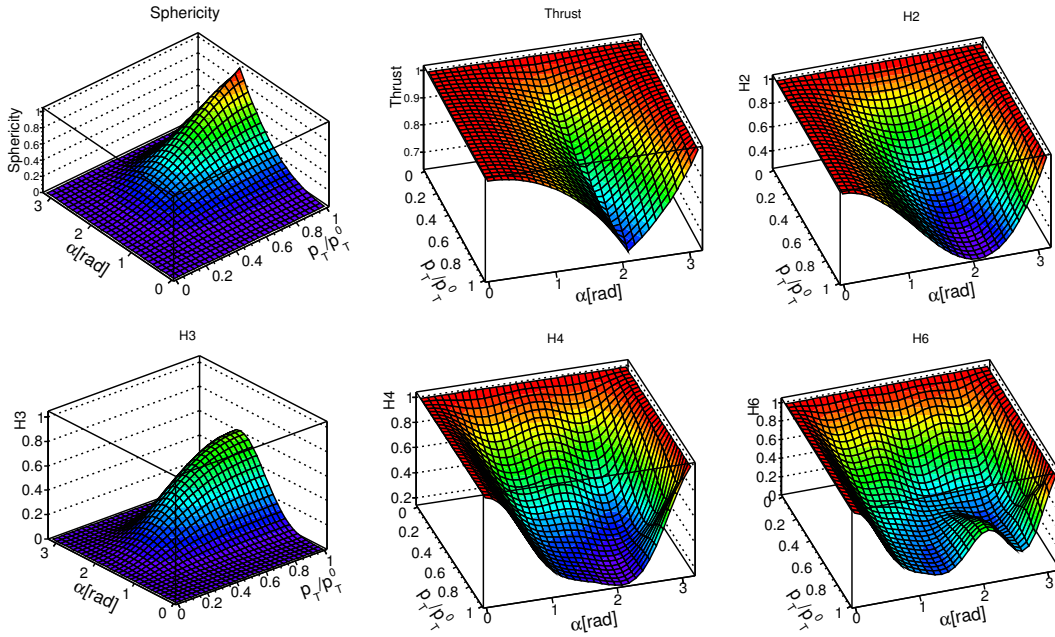


Figure 5.33: Sphericity, thrust and $H_{2,3,4,6}$ for the 3 jets toy model.

it was a starting point for the next study. In [Banfi2010] it was demonstrated that event shape observables are not sensitive to events with more than three equidistant particles. This becomes very important when instead of particles one investigates jets which are approximated for simplicity by single particles, ignoring the underlying event. Sphericity, thrust and directivity cannot identify events with multiple jets evenly distributed.

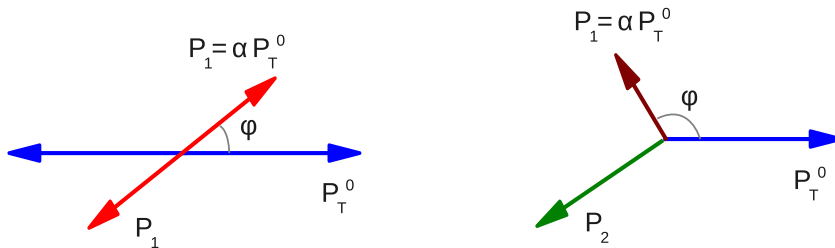


Figure 5.34: Schematic view of the toy models used for event shape selection performance.

The multiple jets may have different energies and orientations and in this section another toy model is used in order to investigate what are the requirements on the momenta and orientation of the pseudo-jets in order for the event to pass the event shape cut. The toy model used in this section investigates the discrimination capabilities of the event shape observables when two pairs of two back-to-back jets

are orientated at different angles (see Figure 5.34). The momentum for the “jets” is the same in each of the pairs (for momentum conservation) but may be different for the jets in different pairs. The momentum is normalized to the largest value without affecting the final result. A scan for the angle between the jets and also the ratio of the momenta of the two pseudo-jets was performed and the results are presented in Figure 5.35. In the case of sphericity (upper left) and thrust (upper right) there are special configurations corresponding to almost equal momentum pair of perpendicular jets. The regions where the events will pass the cuts ($S > 0.8$, $T < 0.7$) is quite narrow for both event shape observables. Obviously, this is a toy model and the real event shapes will be influenced by the underlying event and the cone shape of the jets. There is no condition on the maximum transverse momentum.

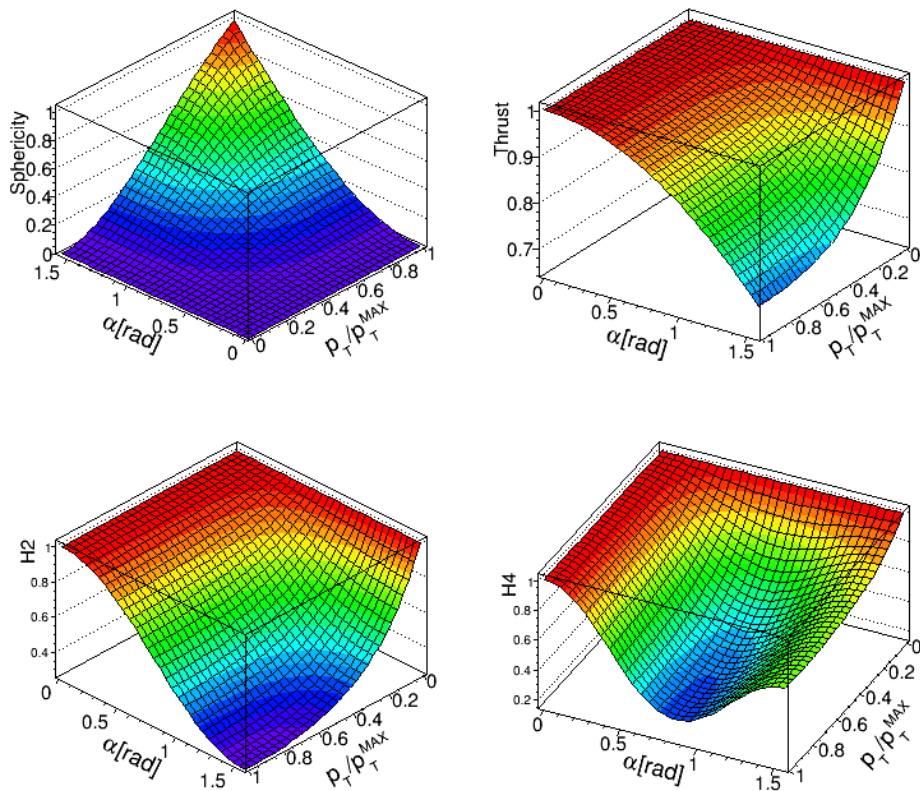


Figure 5.35: Sphericity, thrust, second and fourth Fox-Wolfram moments as a function of the angle between the two pairs of jets and the fraction of the momentum relative to the largest one. The results are obtained for the four jets toy model.

Only two Fox-Wolfram moments are shown in the lower plots of Figure 5.35. The reason is that one of the properties of the Fox-Wolfram moments mentioned in section 5.5.1 is that a given Fox-Wolfram moment will have a high value if the geometry of the event shows a periodicity and the order of the moment is a multiple of that specific periodicity. For the toy model used in this section, when the lowest momentum value is relatively small or the orientation of the jets is close to parallel,

the event shape periodicity is 2. When the jets will have similar momentum values and will be perpendicular, the degree of symmetry is 4. This is clearly visible in the distributions of the two chosen FWM. H_2 is close to 1 when the two jets are (almost) collinear or the low momentum jets are negligible. On the other hand, the H_4 value is high when the two jets are oriented at 90° or collinear, but also when the values of the lowest jet p_T is close to 0 and the event is basically reduced to only two back-to-back jets. H_4 cannot differentiate between two or four evenly spread jets/particles. Although there are configurations of the jets pair for which H_2 or H_4 have small values, no region will allow both FWM to reach values in order to pass the uniformity cuts. This is a strong argument in favor of using a combination of FWM instead of single event shape observable, at least for this analysis.

The results in this section are in accordance with the results presented in section 5.11. High momentum particles require that the same event contains other particles with similar momentum and proper orientation. It is unlikely that enough particles with high momentum to be generated in the same event for any of the input distributions used, even for high multiplicities. Although this toy model uses a very low number of particles, it gives a reasonable explanation to the tail cancellation of the event shape selection. Low values of the leading particle transverse momentum are specific to the soft region and the ESO select such events with the bias discussed in section 5.11. The toy model indicates also that a rather restrictive relative distribution of the particles momenta is needed in order to have azimuthal isotropy, but it does not give a definitive answer to how the p_T spectrum shape will be affected.

This model could be improved by introducing more particles, eventually with rather low p_T values to simulate the underlying event. This will shift the event shapes toward the isotropic region as suggested by Figure 5.3.

Considering more than four jets is a problem difficult to investigate. For the moment, the analysis is done under the assumption that special configurations of each of the jet momenta and orientations are needed in order to pass the FWM cuts, but also for sphericity and thrust, event shape observables that are proven to be less sensitive. Events with more than four jets are also improbable. A plausible hint in this direction is given by the ATLAS results from [ATLAS2011b] shown in Figure 5.32 with the mention that the analysis conditions are different. Although the ATLAS results are obtained in a different acceptance region and the momentum of the jets is extremely high, it is reasonable to assume that most of the jetty events have a relatively low number of jets.

Minijets, on the other hand, may have a rather high multiplicity. Their contribution is evaluated via two particle correlations.

The models presented above for a very small number of particles/jets give a hint about the conditions required for an event to be considered uniform.

5.12 Discussion

Modified transverse Fox-Wolfram moments were investigated. The results based on simulations indicate that this class of event shape observables can be used to separate events with highly isotropic azimuthal distribution. Compared with other observables, the FWM are, by definition, build to be used as a multidimensional

event selection, a more natural method to discriminate between events. The particle distribution relative to the leading particle in the events selected using the FWM is very close to being uniform. Also, the p_T spectra of the uniform events are quite different from the same distribution in high multiplicity events and, even more, from the minimum bias events. This result is strongly encouraging.

Considering the “ladder” pattern in the distribution of the number of jets and the narrow region in phase space where jets can be labeled as uniform by the sphericity, and thrust, the conclusion is that jets are rejected with high probability.

The downside of using event shape observables is that the transverse momentum spectra are biased and a fake signal of flow might be introduced when selecting isotropic events. This fake positive signal does not exclude a real signal but cannot be easily separated from a real collective behavior.

The cut values used in this analysis were established empirically. A systematic study focused on finding better suited parameters for event selection taking into account the minimization of the fake signal is mandatory. It will be extremely useful to implement a more consistent set of FWM cuts in order to separate the event classes more rigorously.

Another highly promising direction is to analyze extremely high multiplicity (i.e. greater than 80) events from the high multiplicity runs selected by the ALICE trigger. Also, it is not obvious how many H_l values are necessary to select highly azimuthal isotropic events. The first 8 values presented in this study were evaluated and demonstrated good capabilities in selecting high multiplicity azimuthally isotropic events.

Sphericity, Thrust, Recoil and Directivity event shapes were implemented in the ALICE official analysis framework - AliRoot. Also the performance of the mentioned observables in selecting events with azimuthal isotropy was investigated and the corresponding p_T spectra were reconstructed. Despite their simplicity, the event shapes used can distinguish events with azimuthal distribution relatively uniform and have an immediate consequence on the shape of the transverse momentum spectra. As perspectives, the actual limits for the event shape cuts will be further investigated, in order to implement a more consistent set of values, without analyzing a very narrow region in the phase space and, hence, treating mostly fluctuations.

Chapter 6

Efficiency corrections

Particles reconstructed in analyzed events do not always originate in the primary vertex. The most probable sources of contamination are particle decays and secondaries produced in the particle interaction with the material present in the experiment. Also, some particles will not be detected due to the limited acceptance and efficiency or the interaction with the material. Both effects can be evaluated using Monte Carlo simulations once the detector response and the material distribution in the experiment are known.

6.1 Trigger efficiency

Due to limited acceptance and efficiency of the trigger detectors, some collisions may not be triggered. Monte Carlo simulations using the PYTHIA generator were used for evaluating the trigger efficiency. This efficiency was found to be very close to 100%.

6.2 Vertex efficiency

The influence of the vertex reconstruction and position were investigated. Some events recorded with the minimum bias trigger may not have a reconstructed vertex. The vertex reconstruction efficiency is defined as the ratio between the number of events triggered which have a reconstructed vertex position and total number of triggered events. The vertex reconstruction efficiency was investigated directly on data and was found to be $\approx 89\%$. The vertex reconstruction efficiency is used for the minimum bias invariant spectrum.

Another study evaluates how the tracking efficiency is affected by the vertex position along the z axis. The tracking efficiency for events with vertex position in the center of the detector ($|vertex_z| < 0.5$ cm) and 9 cm $< |vertex_z| < 10$ cm are plotted in Figure 6.1.

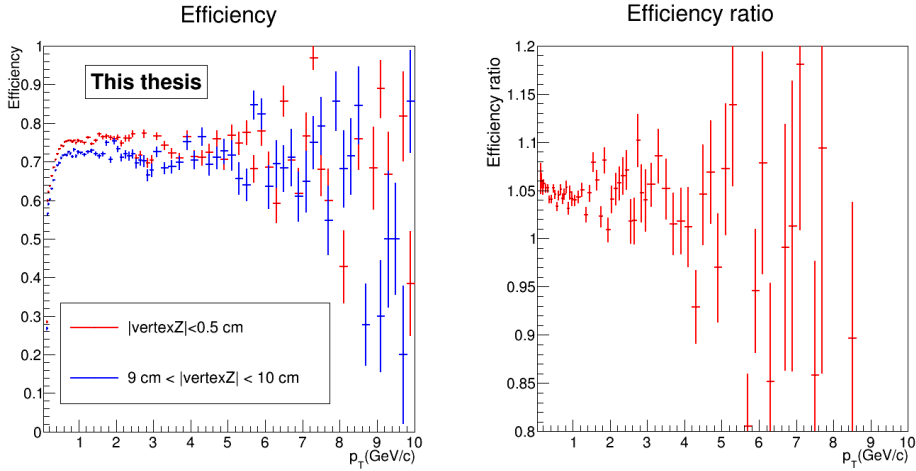


Figure 6.1: Tracking efficiency as a function of vertex position along the z axis (left panel). In the right panel the ratio of the efficiency for events with the vertex position near the center of the detector and events with the reconstructed vertex position between 9 and 10 cm from the center is plotted

6.3 Acceptance and tracking efficiency corrections

The acceptance and tracking efficiency presented here are defined as the ratio between the reconstructed tracks, after the track cut selection, and the generated primary particles in the event. Only events that pass the cut selection for trigger configuration, vertex reconstruction and vertex position are considered. Only primary reconstructed particles are included since the feed-down contamination is removed separately by using DCA studies described in section 6.4.1.

6.3.1 Multiplicity dependence

Efficiency was proved in the early stages of the analysis to be multiplicity dependent (see Figure 6.3). The trend was that the efficiency was growing with multiplicity and it was also model dependent. There is no multiplicity dependence of the efficiency when the selection is made using the generated multiplicity (given by the model used in the simulation). This independence on generated multiplicity can be understood by the fact that the correlation matrix (Figure 4.4) has a constant slope. This estimates, with a good approximation, the mean reconstruction efficiency which is not multiplicity nor model dependent. It is given only by the detector performance. The correlation matrix includes secondary particles contamination but their contribution is, as shown in section 6.4.1, uniform as a function of multiplicity and at the level of few percents. This does not have a strong influence on the correlation matrix, especially regarding the multiplicity dependence.

The detector performance is not at the origin of this dependence since ALICE is a detector designed to cope with multiplicities generated in Pb-Pb collisions. These are two orders of magnitude higher than the multiplicities in proton-proton events. Even further, the detector performance would decrease the efficiency at high

multiplicities and not increase it.

The reason for this behavior of the efficiency resides in the multiplicity selection method itself. Global multiplicity reconstruction performance is plotted in Figure 4.4. As can be seen, the distribution of reconstructed multiplicity has, for a given generated multiplicity, a rather wide Gaussian shape. When a cut is applied on a chosen global multiplicity range, different parts of each Gaussian distributions for the generated multiplicities are mixed. Since the multiplicity distribution is not flat, a high number of events with high number of reconstructed particles, corresponding to a high efficiency are mixed with a lower number of events with low efficiency. In Figure 6.2 there is an example of a bin selection (between gray lines) using the reconstructed multiplicity. Three generated distributions are plotted in the same region as the reconstructed multiplicity bin. In the reconstructed multiplicity bin many of the events come from the middle of the distribution of the generated bin that is colored in green. The tracking efficiency for this class of events is roughly the mean efficiency given by the slope of the multiplicity correlation matrix. Therefore, it does not introduce a significant efficiency bias. Also, many events in the selected multiplicity bin are contributions from the tails of the neighbor bins. The contamination from the lower bin (in red) is coming from events with high track reconstruction efficiency or high feed-down contamination (or both), while the upper bin (in blue) biases the efficiency toward lower values. The two tails have different number of events (strongly decreasing toward higher bins) with different number of particles and the overall bias is not canceled.

This multiplicity dependence of the tracking efficiency cannot be used as it is, because it is different for different models. The model dependence, originating in the difference between multiplicity distributions of the two models, makes it impossible for the efficiency to be used on a bin-by-bin basis.

One solution is to use the combined multiplicity estimator defined in section 4.2, [Shahoyan]. This estimator counts the global tracks, the tracks reconstructed by the ITS that are not global tracks and the remaining tracklets in the ITS that do not correspond to any of the previous categories. Even if the argument of combining events with high efficiency with events with low efficiency remains valid, the fact that the Gaussian distributions are narrower than in the case of global multiplicity results in a much lower multiplicity dependence of the efficiency. Multiplicity selection for a narrower correlation matrix, closer to the diagonal, as shown in Figure 4.6, is similar with the case of selecting multiplicity using generated tracks. When selecting events using generated multiplicity the efficiency is the same for all multiplicity bins, as mentioned before. Use of the combined multiplicity estimator limits event migration between multiplicity bins.

A weight calculated using the generated and unfolded multiplicity distributions can be used in the efficiency estimation. The results are similar to the results obtained with the combined multiplicity estimator [Herghelegiu2012].

The efficiency in each of the six multiplicity bins defined for the MB trigger and three bins for the HM trigger is shown in Figure 6.7. Except statistical fluctuations, the efficiency shows a rather negligible multiplicity dependence. The plot in Figure 6.8 shows the ratios of the efficiencies for all the multiplicity bins relative to the minimum bias efficiency calculated for all the events. The p_T range was reduced

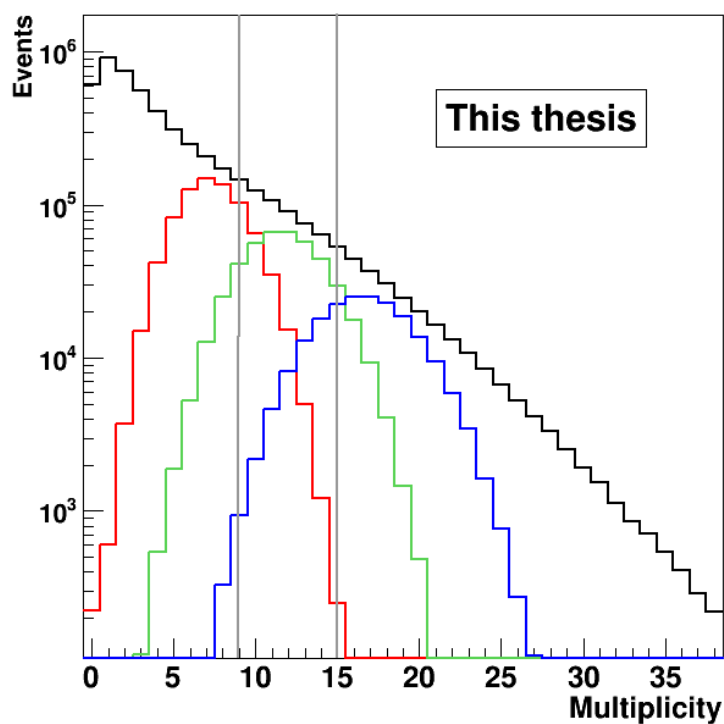


Figure 6.2: Generated bin mixing for a given reconstructed multiplicity bin. The reconstructed multiplicity distribution is displayed in black. The red, green and blue lines represent three consecutive generated multiplicity bins. This example is shown for illustration purpose only. It does not represent an experimental case.

to the region where the fluctuations are low enough to evidence any multiplicity dependence. The maximum deviation of the efficiency is below 2% in the region with reasonable statistics.

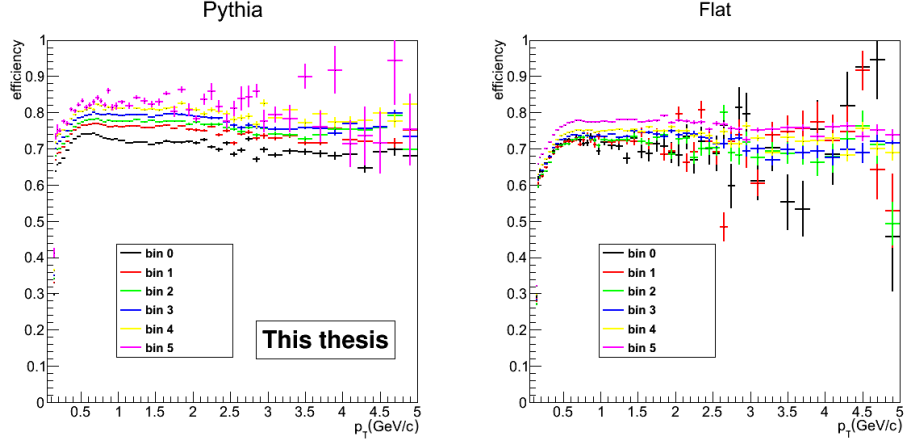


Figure 6.3: Global multiplicity bins - efficiency dependence.

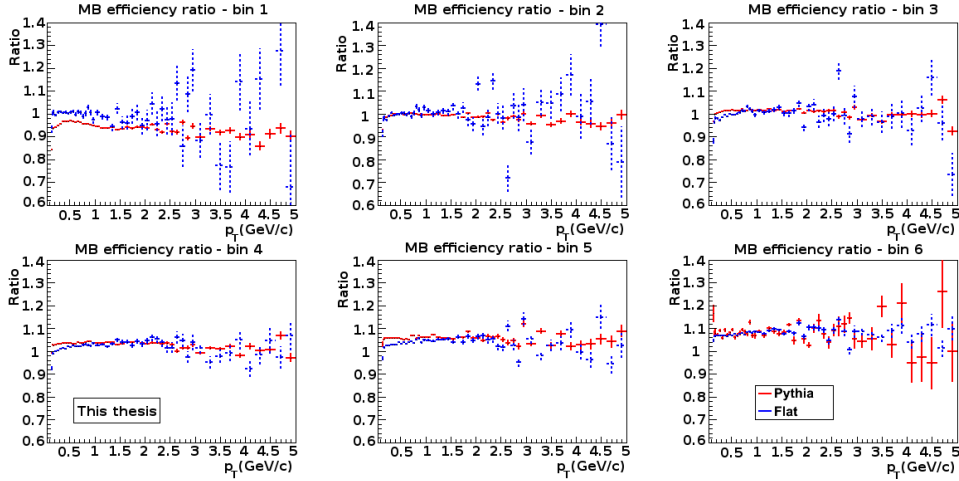


Figure 6.4: Bin by bin ratio for the global multiplicity.

Multiplicity bin limits are shown in table 6.1. The seventh multiplicity bin for MB trigger is not used in the analysis. It has the same limits as the first high multiplicity bin in order to investigate any bias from the hardware trigger by comparing the raw spectra from different triggers on the same multiplicity range. The ratio between the two spectra for the same multiplicity range recorded with the two trigger configurations is plotted in Figure 7.4. The ratio is very close to 1 and, within the error bars, the two spectra are in good agreement ($\sim 2\%$). The mean combined multiplicity value, in each multiplicity bin, was calculated from the reconstructed combined multiplicity distribution. The mean combined multiplicity for the minimum bias case is 8.69.

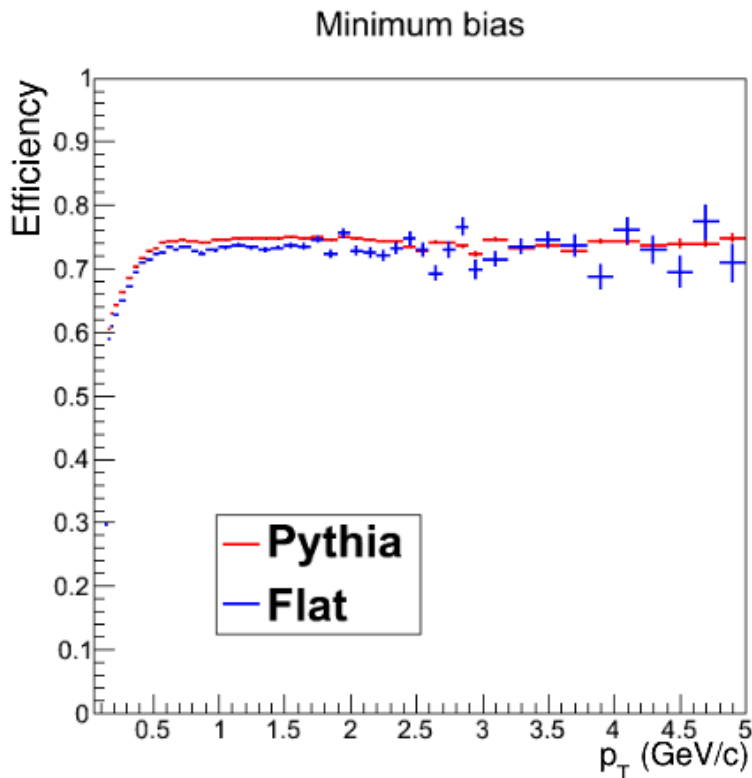


Figure 6.5: Minimum Bias efficiency for Pythia and Flat Pythia simulations.

6.3.2 High multiplicity bins efficiency

Simulated anchored runs from the LHC10e period that include a high multiplicity trigger have very low statistics ($\sim 10\%$ of data statistics) and cannot be used for efficiency estimation bin-wise. The only way to investigate the efficiency at such high multiplicities is by using flat multiplicity runs from the LHC10d period. These runs are simulated using the Pythia 8 generator. The multiplicity distribution is biased as shown in Figure 6.9. The tracking efficiency is found to be multiplicity dependent for the combined multiplicity estimator within a few percents. Therefore, different multiplicity bins that were selected with the combined estimator can be corrected with the efficiency evaluated with high statistics at minimum bias. The multiplicity dependence is included in the final systematic uncertainty.

6.3.3 Efficiency dependence on event shape observables

Results from section 5.11 show a bias toward low p_T values for the events selected as "uniform" by the event shape observables. Therefore, the efficiency dependence on the event shape cuts was also studied. Tracking efficiency for event shape selection in each multiplicity bin is plotted in Figures 6.10, 6.12, 6.14 and 6.16. The multiplicity bins are presented as follow. The first row contains the first three bins, followed by the last three minimum bias bins on the second row. For Sphericity, Thrust and Directivity, the efficiency is plotted in red, green and blue corresponding to

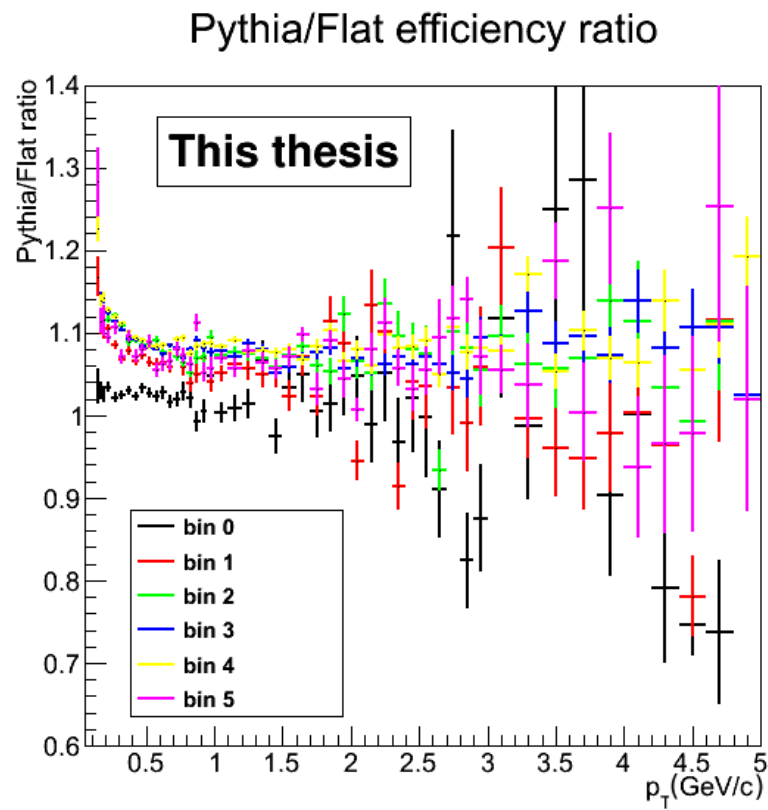


Figure 6.6: Global multiplicity bin by bin ratio for the efficiency of Pythia and Flat Pythia runs.

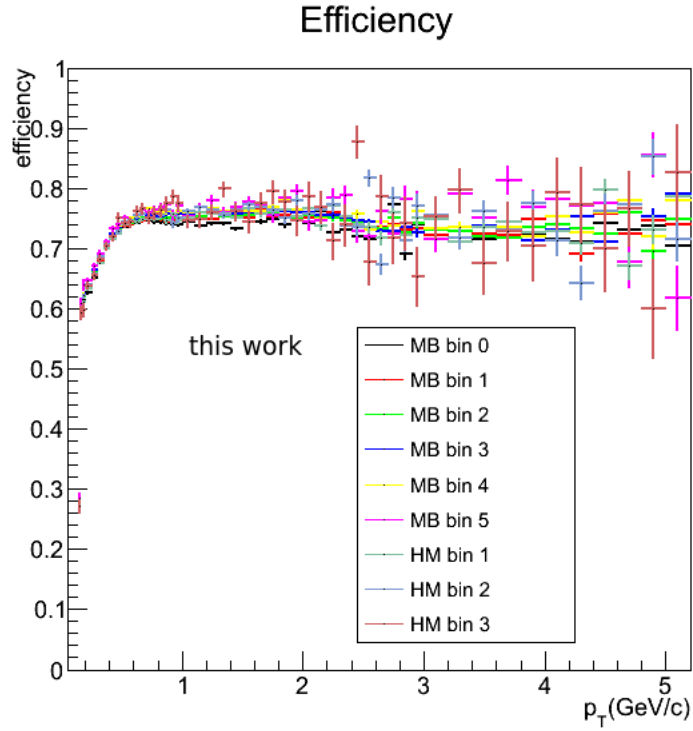


Figure 6.7: Tracking efficiency for combined multiplicity bins for MB and HM trigger.

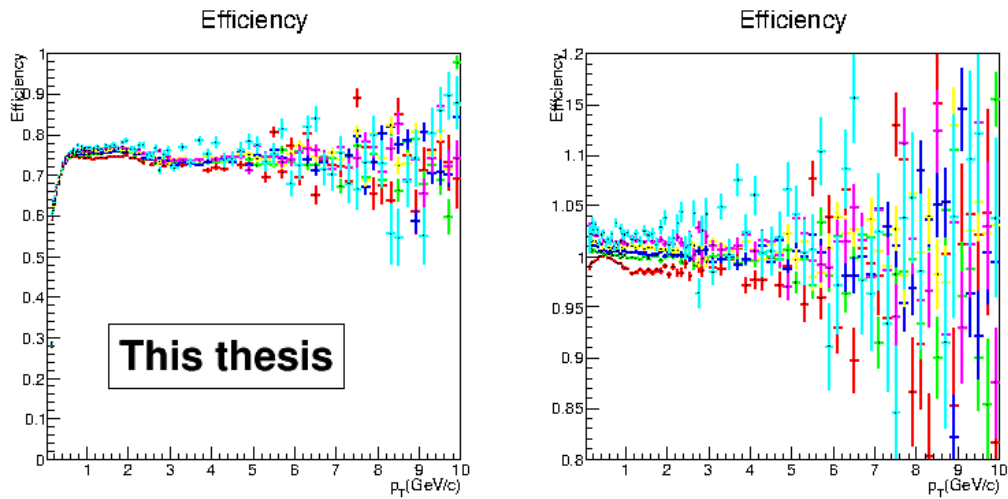


Figure 6.8: Tracking efficiency for minimum bias combined multiplicity bins (left panel). The ratio of the efficiency in each multiplicity bin and the minimum bias efficiency is plotted on the right panel.

Table 6.1: The correspondence between global and combined multiplicity bin limits.

Trigger	Estimator	Global	Combined	Mean Combined Multiplicity
	Bin no.			
Minimum Bias	0	0-5	0-6	3.26
	1	6-9	7-12	9.17
	2	10-14	13-19	15.59
	3	15-22	20-28	23.25
	4	23-31	29-39	32.72
	5	32-39	40-49	43.31
	6	40-49	50-59	53.21
High Multiplicity	1	40-49	50-59	53.21
	2	50-62	60-71	63.57
	3	63-72	72-82	75.27
	4	>72	>82	87.63

the low, medium and high values for each of the event shapes. The medium values are defined as the values between the isotropic and non-isotropic regions identified using the values from Table 5.8.3. For the Fox-Wolfram moments, red is used for the azimuthally isotropic events, while green is for everything else. In Figures 6.11, 6.13, 6.15 and 6.17, the efficiencies divided by the efficiency in the corresponding multiplicity bin are plotted. The bin ordering and the coloring convention is the same. For all the event shape observables, the efficiency at low transverse momenta is higher for "isotropic" events and lower at high p_T values. This behavior is in good agreement with the results from section 5.11. Events with low p_T particles are preferentially selected by the event shape observables. Either these events have a non-biased efficiency that would allow the event to be selected as uniform, or events containing higher p_T particles must have a low efficiency in that p_T region in order to lose those particles. A bias towards low transverse momenta can be achieved if the efficiency at high p_T is low and the particles with low p_T are well reconstructed. The argument can be mirrored for the "non-isotropic" events where the low momenta contribution is reduced by a low efficiency and the high momenta must have a high reconstruction probability. Similar to the results from section 5.11, the bias is smaller for high multiplicity bins.

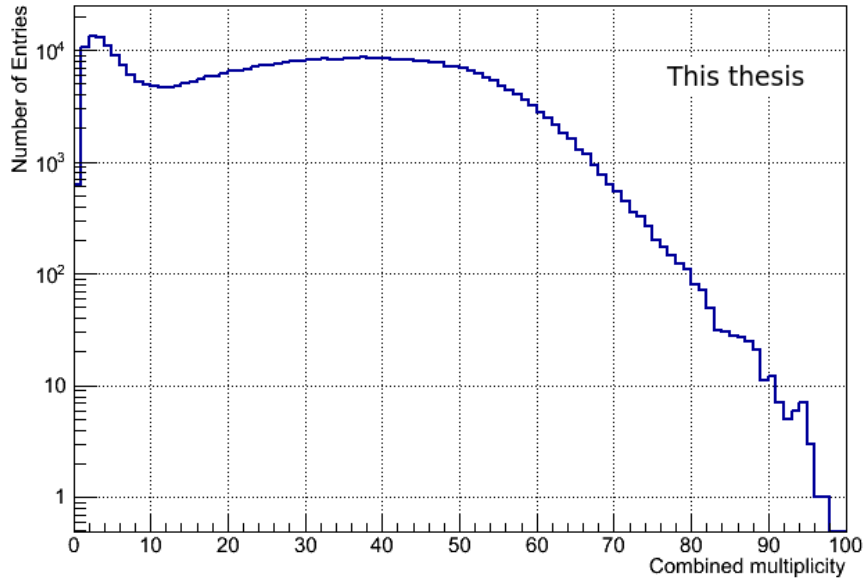


Figure 6.9: Flat multiplicity distribution.

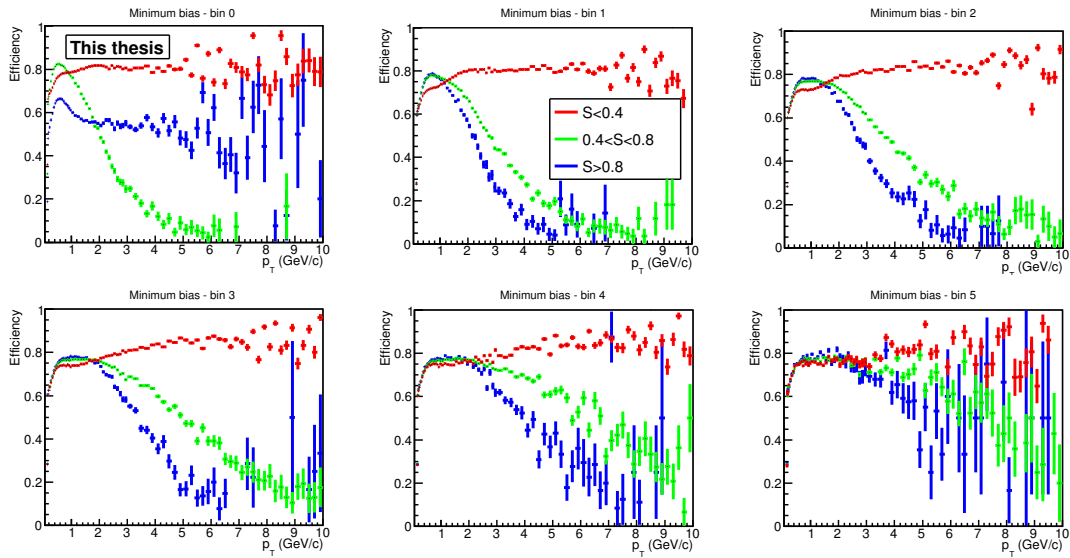


Figure 6.10: Efficiency in multiplicity bins for sphericity event selection. Isotropic events ($S > 0.8$) are plotted in blue. Green correspond to events with sphericity between 0.4 and 0.8. The efficiency for the pencil-like events with $S < 0.4$ is plotted in red.

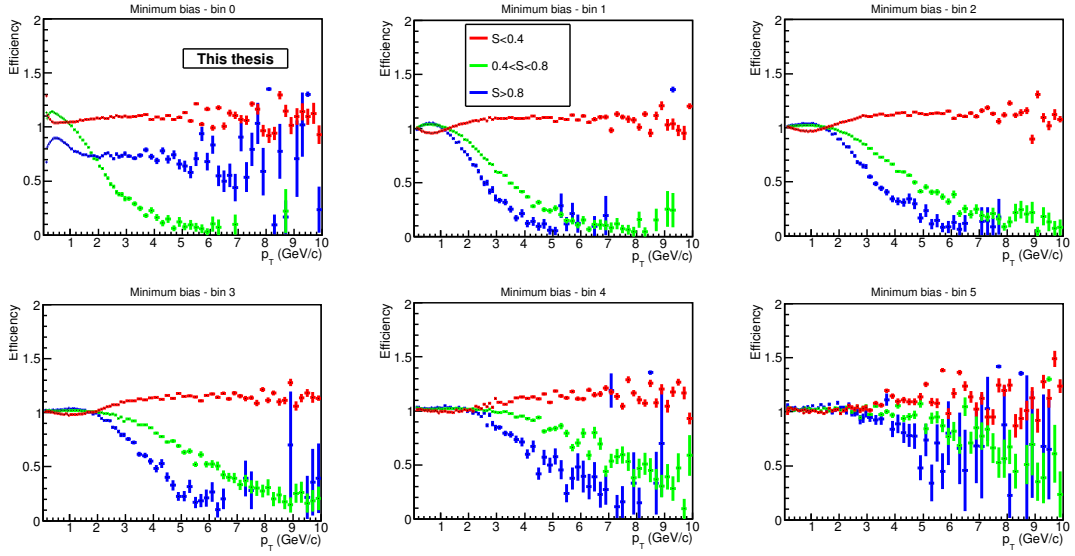


Figure 6.11: Efficiency in multiplicity bins for sphericity cuts relative to the efficiency in the corresponding multiplicity bin. Red, green and blue correspond to low, medium and high sphericity values.

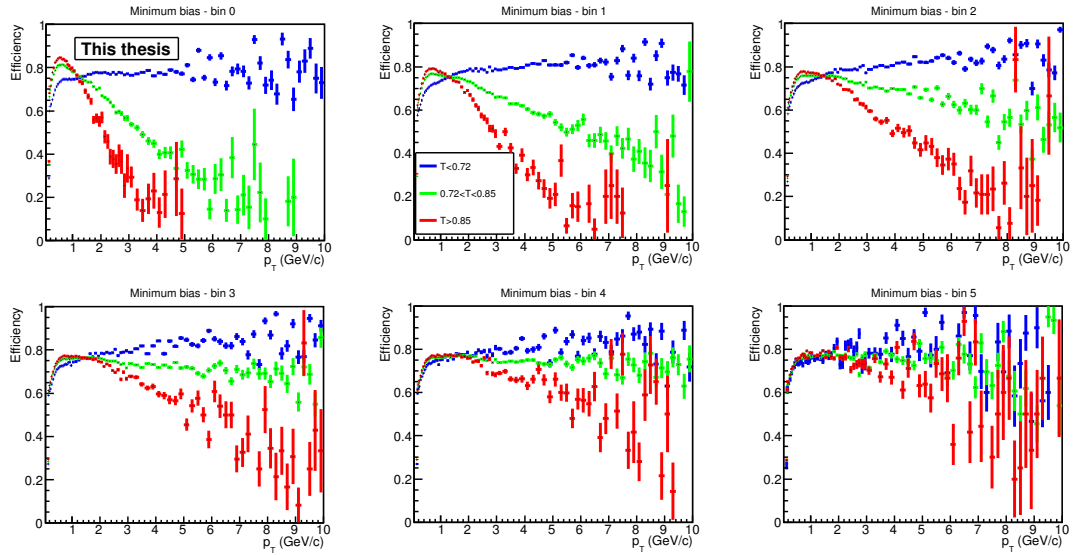


Figure 6.12: Efficiency in multiplicity bins for thrust cuts. Isotropic events ($T < 0.72$) are plotted in blue. Green correspond to events with thrust between 0.72 and 0.85. The efficiency for the pencil-like events with $T > 0.85$ is plotted in red.

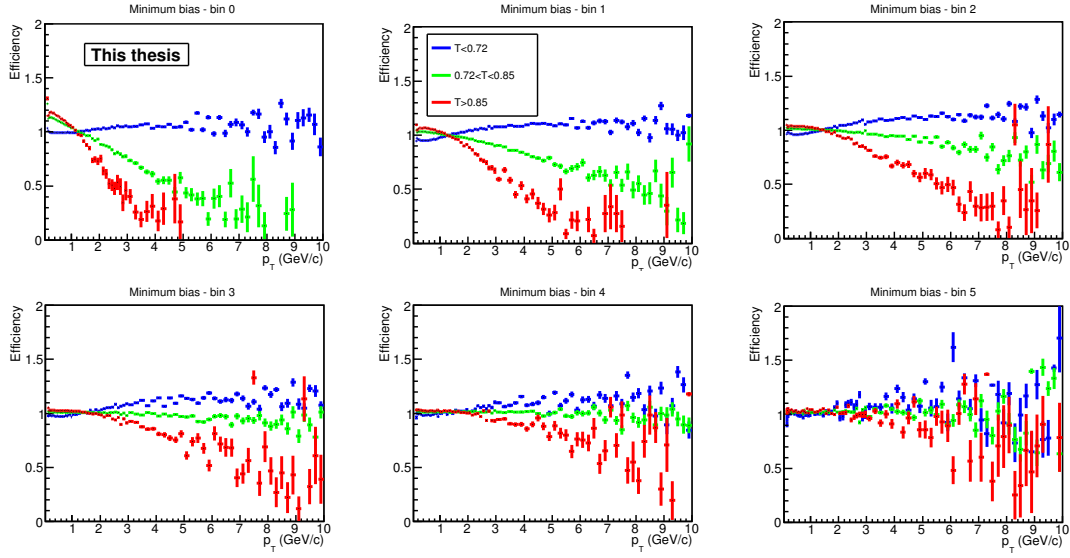


Figure 6.13: Efficiency in multiplicity bins for thrust cuts relative to the efficiency in the corresponding multiplicity bin. Red, green and blue correspond to low, medium and high thrust values.

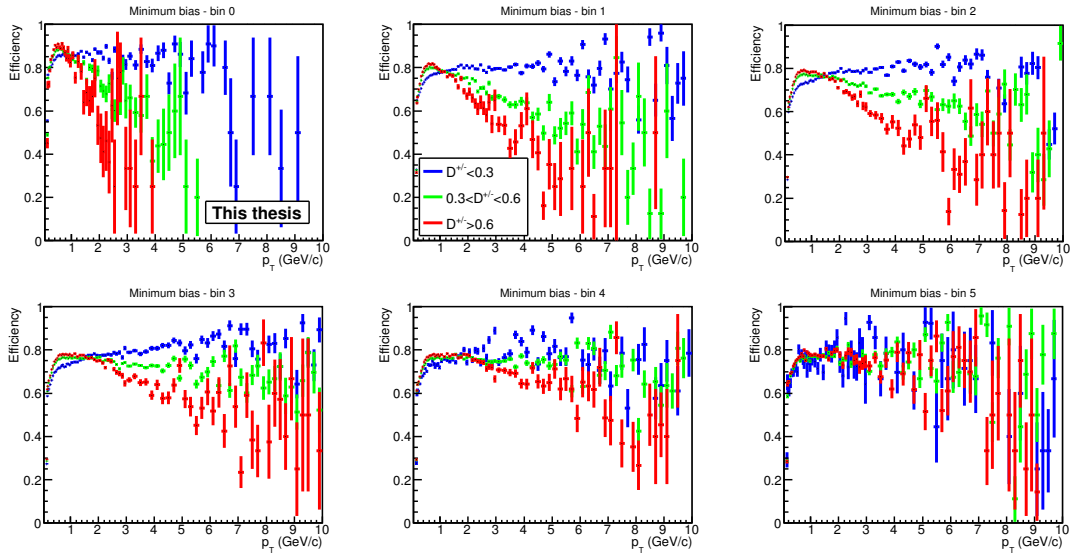


Figure 6.14: Efficiency in multiplicity bins for directivity cuts. The efficiency for isotropic events is plotted in red, the pencil-like events in blue, and events with medium directivity values in green.

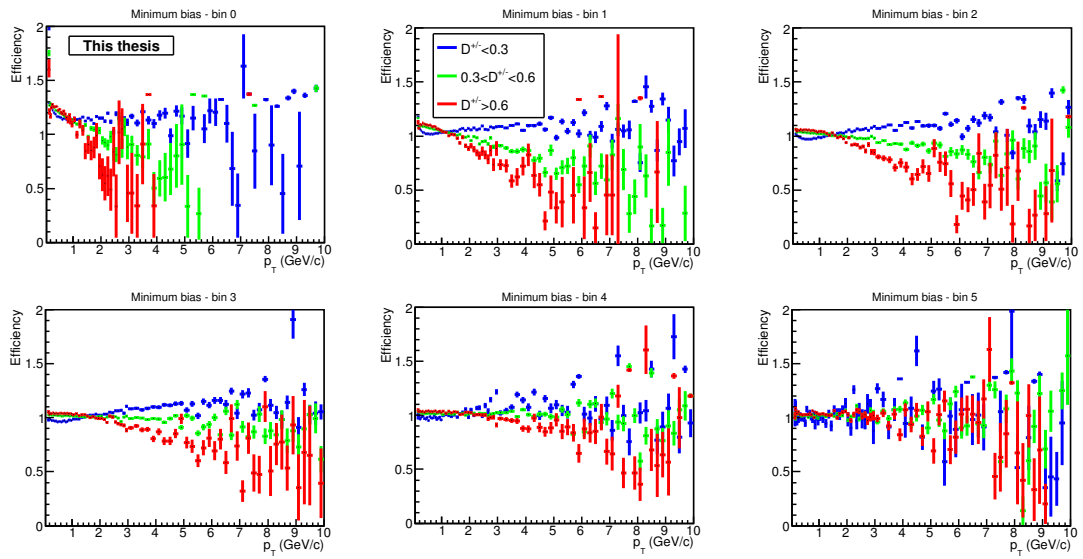


Figure 6.15: Efficiency in multiplicity bins for directivity cuts relative to the efficiency in the corresponding multiplicity bin. Red, green and blue correspond to low, medium and high thrust values.

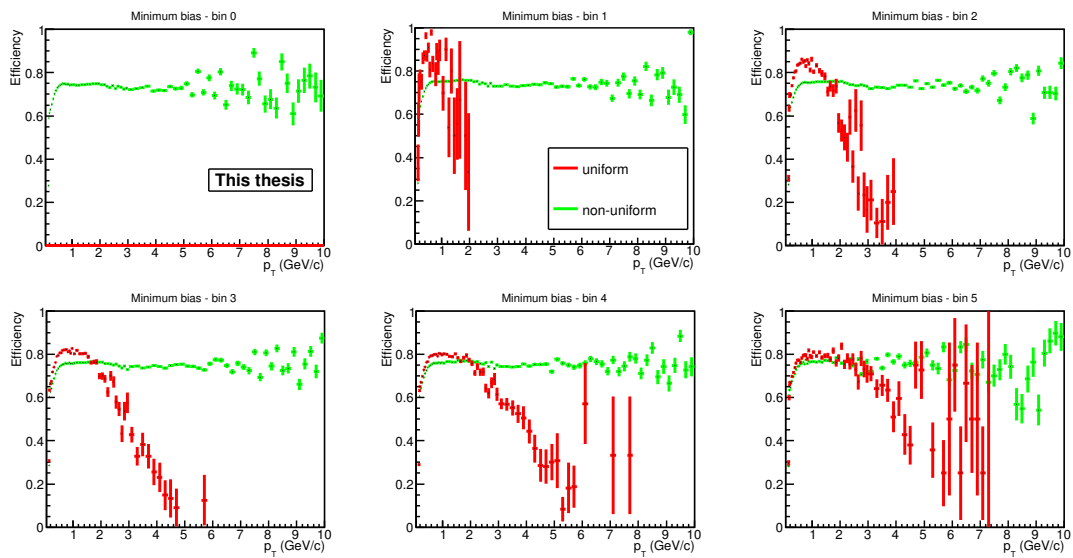


Figure 6.16: Efficiency for multiplicity bins using Fox-Wolfram cuts. In red, the azimuthally isotropic events are plotted. The efficiency for the rest of the events is plotted in green.

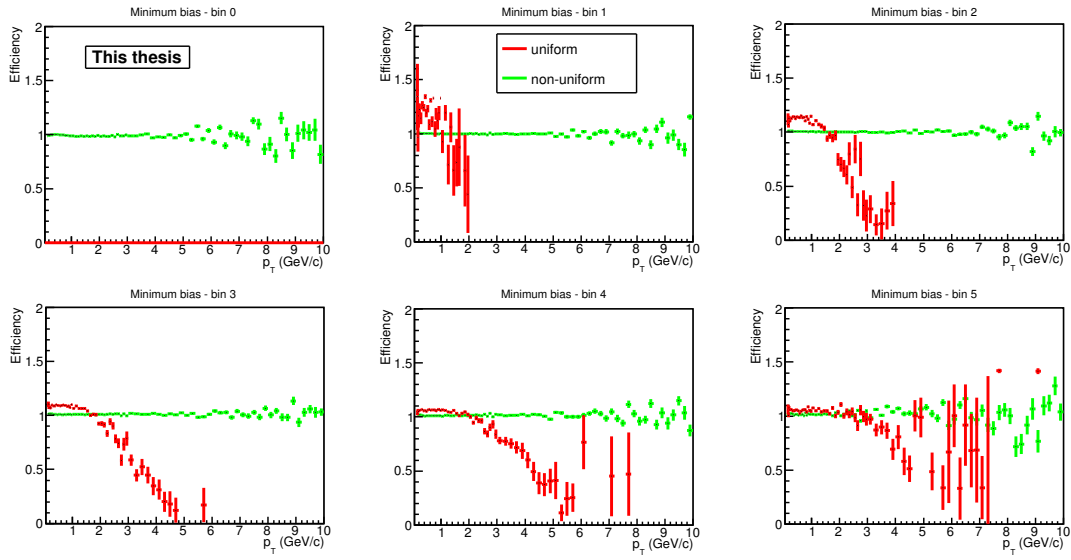


Figure 6.17: Efficiency for multiplicity bins using Fox-Wolfram cuts relative to the efficiency in the corresponding multiplicity bin. Isotropic events are plotted in red, while the rest of the events are plotted in green.

6.4 Feed down correction

Inside the detector not only primary particles are reconstructed, but also particles coming from weak decays or from interaction of the generated particles with the material of the detectors, mechanical framework or any other piece of equipment present in the experiment. These are the two main sources of contamination of the original particles and are called feed-down contamination.

6.4.1 Distance of closest approach studies

Secondary particles cannot be identified as non-primary on a track by track basis. Although some particles can be identified as secondaries, it is impossible to eliminate all the contaminations using standard track cuts. The method used to evaluate the feed-down correction is based on the DCA - Distance of Closest Approach - parameter of each of the reconstructed tracks [Andrei2012]. The DCA represents the minimum distance between the extrapolated trajectory of the track and the main vertex (see Figure 4.3). The DCA cuts in the z direction and the transverse plane, described in section 4.1.6, reduce the secondary particles contamination in the final spectra but cannot fully eliminate it as some secondary particles will have low DCA values and cannot be discriminated from the real primary particles.

The distributions of primary, weak decays and secondary interactions contributions are obtained using the same binning in p_T as used for the efficiency and raw spectra. The distributions of the DCA parameter for primary and secondary particles are plotted in Figure 6.18. These distributions show that it is impossible to eliminate all the secondary particles from the analyzed sample using a DCA cut applied track by track. Some secondary tracks will pass any DCA cut and the contamination is non-negligible. Instead, one can use these distributions to evaluate the feed-down correction in a global manner, as a fraction of the total particle yield in each p_T bin. The principle of this method is based on the different shape of the DCA distributions of the three types of particles. These three shapes can fit the DCA distribution from the data in a single p_T bin. One example of such a fit is shown in Figure 6.18. The data DCA distribution is fitted with primary, material and secondary particles distributions obtained from Monte Carlo simulations, each scaled with a corresponding free parameter of the fit. Once these parameters are found, they are used to evaluate the feed-down correction using the DCA distributions obtained in the corresponding p_T bin with the p_T dependent DCA track cut.

The feed-down correction was not evaluated directly from the Monte Carlo simulations because the strangeness yield is not correctly reproduced in the models. On the other hand, the DCA shape for weak decays and material interactions are well reproduced by the models. This is the reason why the shapes of the DCA distributions can be used for the fit. The amplitudes are the fit free parameters.

Similar to the tracking efficiency, the feed-down correction was also studied as a function of multiplicity. There were two reasons for this study:

- the multiplicity dependence of the efficiency was unexpected and it is a precaution to investigate any multiplicity dependence of the feed-down;

- strangeness yield variations with multiplicity might influence the final correction.

Multiplicity dependence of the feed-down correction is plotted in Figure 6.19. For both high p_T and high multiplicity bins, the statistics was insufficient and made the evaluation of the exact correction difficult [Andrei2012]. Also, at low p_T values, the corrections are ordered for the multiplicity bins. There are arguments to believe that this is nothing but an artifact from the actual fit. For example, the gap between bins was strongly reduced by adding more statistics to the analysis. Also, the distribution for the highest multiplicity bin was clearly lower than the other distributions for the whole p_T range and, again, the difference was reduced by adding more statistics. The explanation for this artifact is that low statistics will result in few histogram bins being filled for the material contamination and also for the extremities of the secondaries. This means that the fit will be done mostly using the peak in the primary particle distribution and the feed-down relative contribution will be reduced. Based on this considerations, the feed-down correction was calculated for the minimum bias events and applied to the spectra in each of the multiplicity bins. For high p_T values the correction was extrapolated using a constant value.

The difference in contamination between multiplicity bins is below 0.5% and is included in the systematic uncertainties. As mentioned, the difference was bigger for lower statistics and, therefore, may further decrease when the statistics is higher. The DCA analysis included all the runs available for the LHC10d period for data and Monte Carlo simulations.

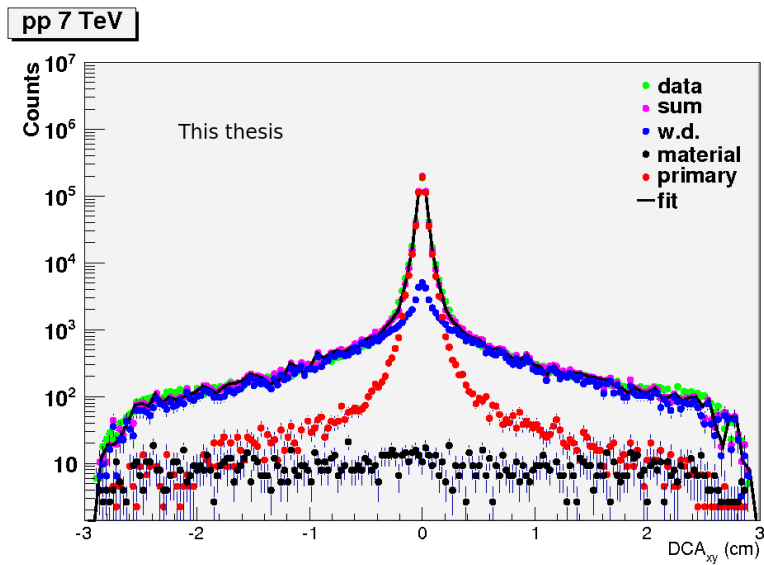


Figure 6.18: Feed-down contamination estimation in one p_T bin. The data are represented in gree, the simulated primary particles in red, the weak decays and material in blue and black, while the total sum is displayed in magenta. The fit result is represented by the black line.

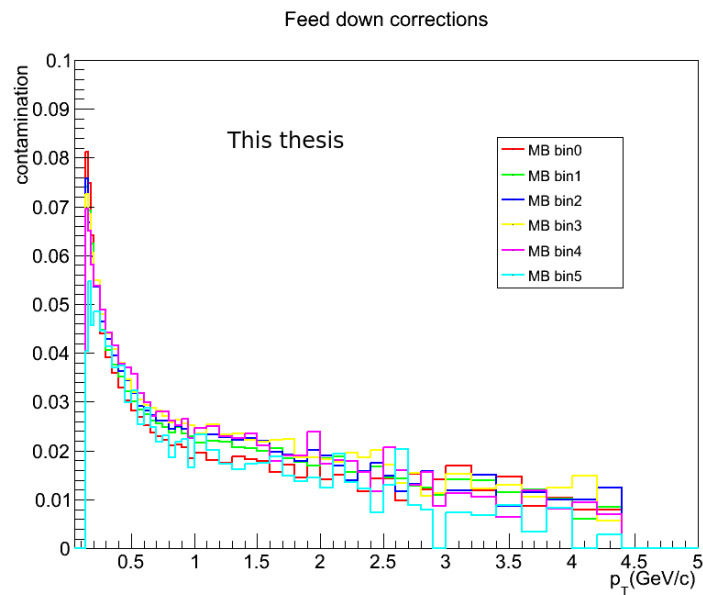


Figure 6.19: Multiplicity dependence of the feed-down correction.

6.5 Systematic uncertainties

6.5.1 Acceptance and tracking efficiency

Tracking efficiency - multiplicity dependence

In the case of multiplicity dependence of tracking efficiency, there is a small deviation from the minimum bias efficiency of $\approx \pm 2\%$ (see Figure 6.8). The systematic error was evaluated searching in each p_T bin for the largest deviation from minimum bias. In order to eliminate the effect of limited statistics, each efficiency ratio was fitted with a polynomial function of degree 9 and the extreme values were found using the fitting functions. The multiplicity bin number 5 was eliminated due to very large statistical fluctuations. The difference between the minimum and maximum deviations was averaged. For p_T values larger than ~ 9 GeV/c, the fluctuations in the final systematic effect were removed using a procedure similar to the one used for the DCA correction (i.e fit with quadratic function, in red). The initial and final (smoothed) distributions are plotted in Figure 6.20.

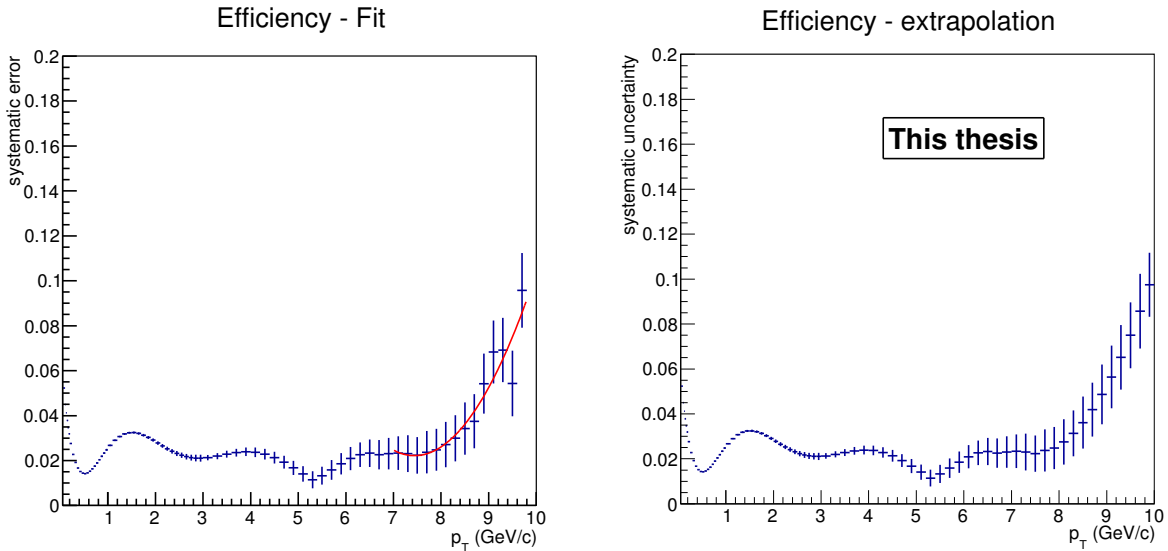


Figure 6.20: The systematic effect for the multiplicity cut.

Track cuts - parameter variation

The systematic uncertainties evaluated from the parameter variation method for the track cuts described in section 4.1.6. The influence of the cut variation is evaluated for the minimum bias spectrum using the efficiency and DCA correction obtained for each of the parameters. The track cuts values have been modified, one by one, according to table 6.2. The deviation from the standard minimum bias spectrum, as a function of p_T , is plotted in Figure 6.21. The fully corrected spectra, including the feed-down correction obtained for the same cut variation in each of the cases, were divided by the standard cut spectrum. The deviations for all the parameters are shown in Figure 6.21. For all parameters the relative variation is p_T dependent and below a few percents. To evaluate the final systematic uncertainty,

the difference between the deviations for each cut in absolute value is computed. All the values obtained for the cut parameters are considered in the final systematic uncertainty evaluation. The systematic error is at the level of a few percents for the number of TPC clusters. At low p_T values, i.e. below 1 GeV/c, the χ^2 per TPC cluster induces a deviation of almost 4%. All other cuts have associated errors smaller than 1% for the whole p_T range up to 10 GeV/c.

Table 6.2: Systematic errors associated to parameter variation.

Track cut parameter	low	standard value	high	associated error
No. of TPC clusters	60	70	80	$\lesssim 3\%$
χ^2 per TPC cluster	3	4	5	$\lesssim 4\%$
DCA_z [cm]	1	2	3	$\lesssim 2\%$
DCA_{xy}	6σ	7σ	8σ	$\lesssim 2.5\%$

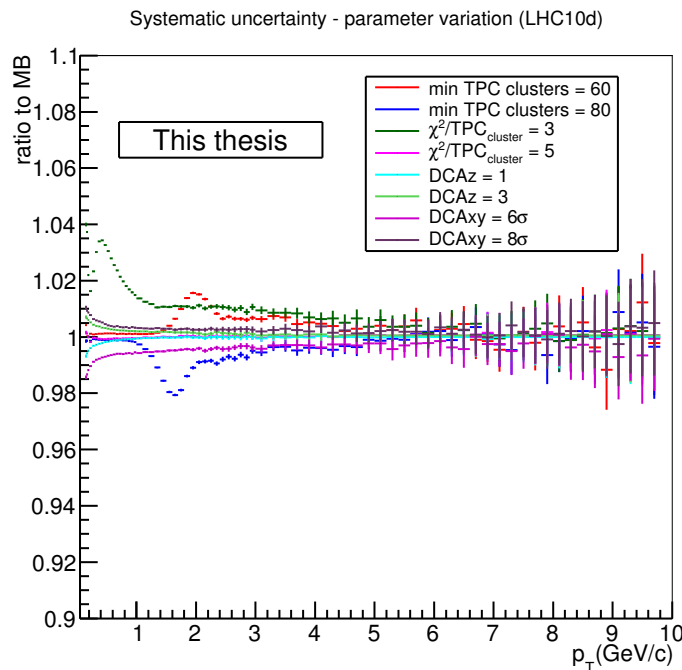


Figure 6.21: Systematic errors associated with parameter variation for each of the track cuts listed in the table 6.2. The variation is represented as a percentage of the minimum bias yield.

Tracking efficiency

The systematic error for the tracking efficiency in the central barrel of ALICE is evaluated at 4% for the charged particles.

6.5.2 Fake tracks and multiple track reconstruction

The fake tracks are defined as tracks that do not pass the requirement on the number of correctly assigned clusters [ALICE2006].

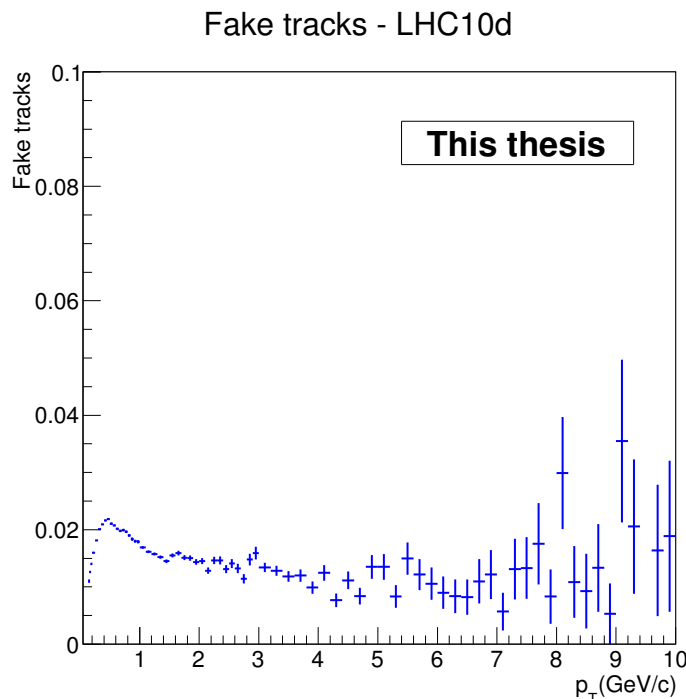


Figure 6.22: Fake tracks contamination for the charged particles.

6.5.3 Feed-down correction uncertainty

The DCA correction is, in most of the p_T bins, at the level of a few percents. There is a small difference between different multiplicity bins and is, most probably, coming from the limited statistics. Secondaries contamination is under-evaluated in low statistics samples due to the fit method described in section 6.4.1. This systematic effect could be eliminated by adding more statistics, both for data and for Monte Carlo simulations. In this analysis, all the available data samples were used.

The systematic error was evaluated as follows: in each p_T bin, the minimum and the maximum DCA correction are identified for all the multiplicity bins. After subtracting the lowest value from the higher one, the result is divided by the DCA correction for the minimum bias. The systematic effect for the feed down correction is below 0.6%, as depicted in Figure 6.23.

At high p_T values, in order to reduce the rather large statistical fluctuations, a fit with a quadratic function was used, as shown in Figure 6.23. For p_T values larger than 5 GeV/c, region where the available statistics is insufficient for DCA studies, the extrapolation was done using a constant value. This value is below 0.1%. Although the contamination decreases with the transverse momentum, a constant value was used for the extrapolation, based on a cautious approach.

Pileup

For the LHC10d period, the maximum value of the Poisson distribution parameter - μ , for the selected runs, is 0.054. Although pileup rejection was used in the analysis, events closer than the vertex resolution cannot be rejected. The pileup contribution to the final spectra was evaluated comparing runs with $\mu \leq 0.031$ and

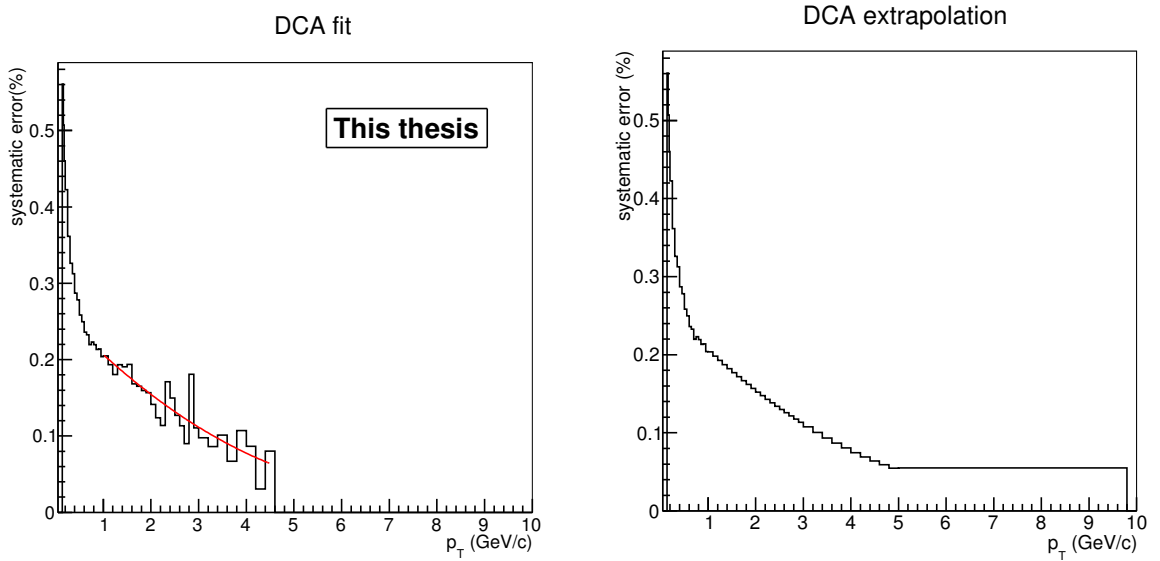


Figure 6.23: Systematic error associated with the DCA correction. In the left plot, the initial evaluation shows large fluctuations at high p_T . The result of fluctuation removal using a quadratic fit is plotted in the right side.

those with $\mu \geq 0.052$. The raw spectra normalized to the number of events for the two cases are plotted in Figure 6.24. In the right panel, the ratio between the spectra obtained for low and high pileup values is shown. A linear fit of the ratio shows that the ratio is close to 1. Therefore, no pileup systematic effect was considered in the final systematic uncertainty evaluation.

All the systematic errors previously described were added quadratically. The final result is plotted in Figure 6.25 as percentage of the yield in corresponding p_T bin. The main contribution is coming from the 4% tracking efficiency.

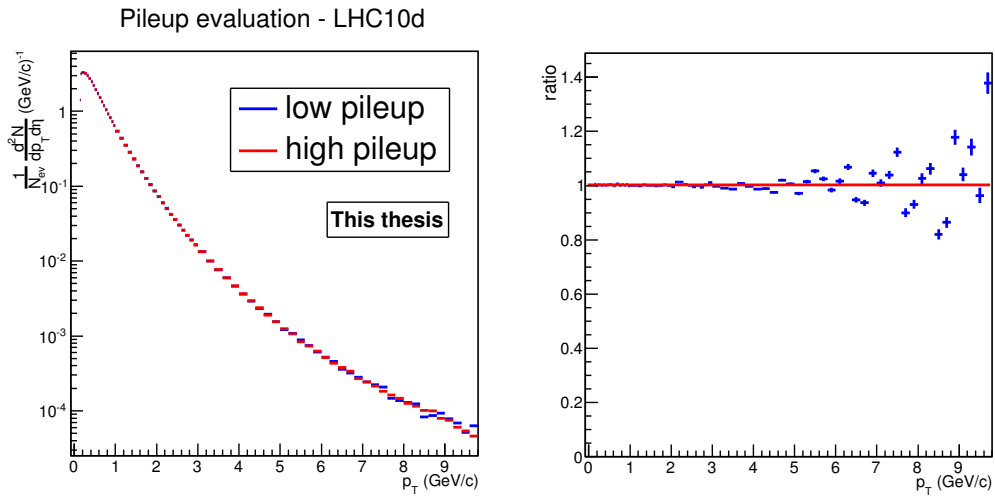


Figure 6.24: Comparison of raw transverse momentum spectra for low (blue) and high (red) pileup runs. The ratio between the two spectra is given in the right side of the plot.

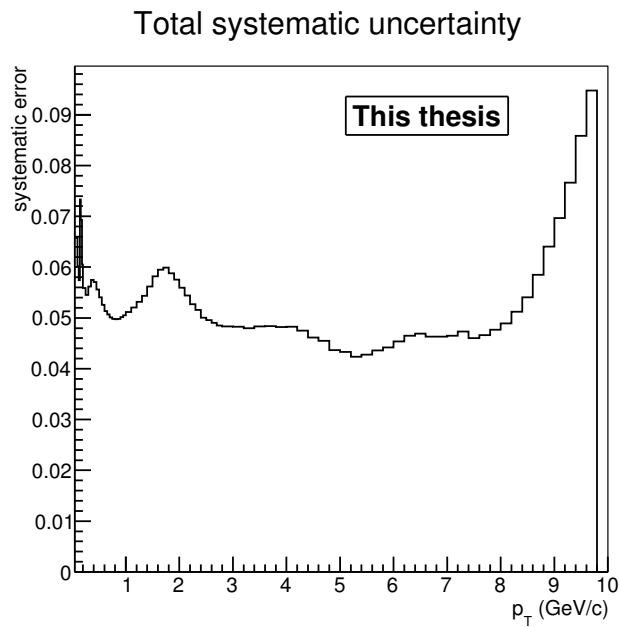


Figure 6.25: Total systematic uncertainty.

Chapter 7

Results

The results presented in this chapter are obtained using the standard cuts presented in Chapter 4. Transverse momentum spectra presented in this thesis were evaluated using the efficiency presented in the previous chapter.

7.1 Transverse momentum spectra

In this section, the transverse momentum spectra for the minimum bias, multiplicity bins and event shape cuts in all the multiplicity bins are presented. The minimum bias spectrum represents the invariant yield and it is normalized to the inelastic number of events. All the spectra for the multiplicity and event shape cuts in multiplicity bins are normalized to the number of events in the corresponding class.

The multiplicity wise transverse momentum spectra are corrected according to the formula:

$$\frac{d^2 N_{corrected}}{d\eta dp_T} = \frac{1}{N_{events}} \frac{1}{Eff_{acc \times track}} \frac{1}{Eff_{feed-down}} \frac{d^2 N_{raw}}{d\eta dp_T} \quad (7.1)$$

where $Eff_{acc \times track}$ is the acceptance and tracking efficiency and $Eff_{feed-down}$ is the feed-down correction.

7.1.1 Minimum Bias spectra

The efficiency and feed-down corrections used for the minimum bias spectra are plotted in Figure 7.1. The final corrected spectra is plotted in the left panel of Figure 7.2 in red. The black point are from another ALICE analysis [Otwiniowski]. The ratio between the two spectra obtained by two independent analysis is plotted in the right panel. The agreement at the level of $\approx 2\%$ and it is within the systematic errors. Here, the invariant yield is obtained by normalizing the spectrum to the inelastic number of events. This is evaluated taking into account the vertex and trigger efficiency. An additional factor of 0.852 was applied in order to correct for the inelastic cross section.

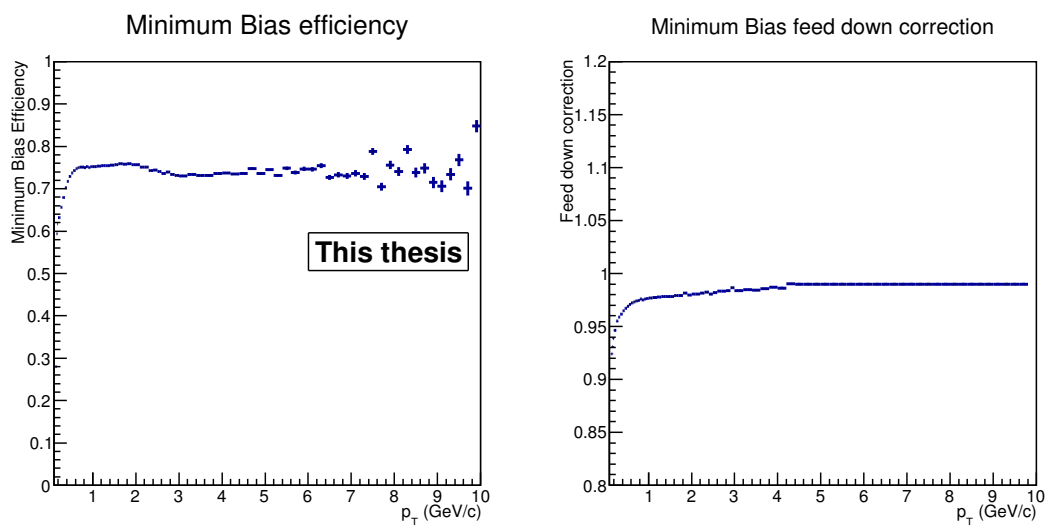


Figure 7.1: Minimum bias tracking efficiency (left panel) and feed down correction (right panel).

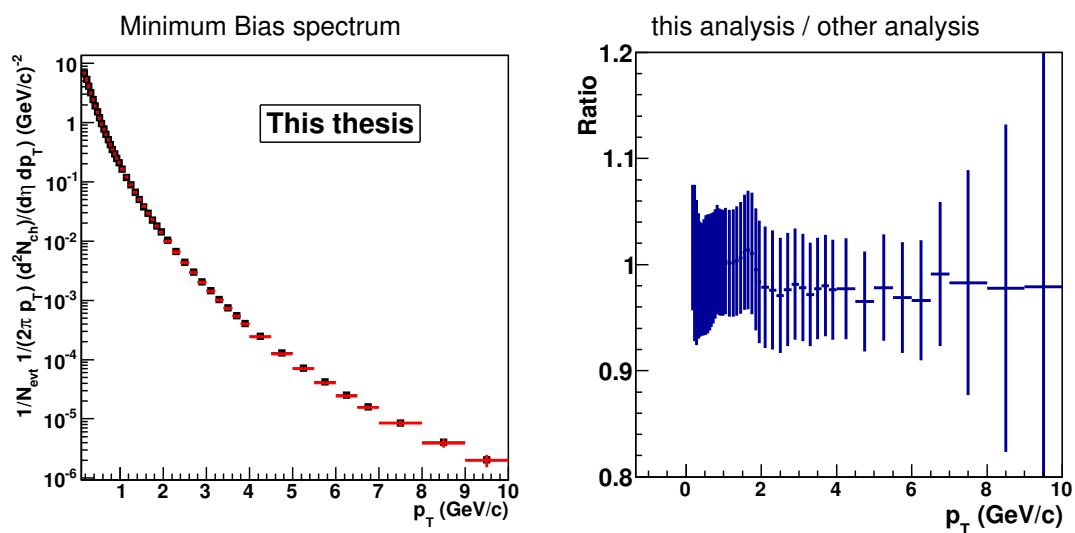


Figure 7.2: Transverse momentum spectra for minimum bias (left panel). Red points are the results of this analysis, while black points are obtained in another ALICE analysis. In the right panel, the ration between the two results is displayed.

7.1.2 Transverse momentum spectra - multiplicity dependence

The transverse momentum spectra in each of the multiplicity bins was corrected with the efficiency for the minimum bias. A comparison between the LHC10d and LHC10e period is plotted in left panel of Figure 7.3. The ratio between the efficiency for the LHC10d and LHC10e periods is plotted in the right panel. The ratio is relatively flat and indicates a higher efficiency for the LHC10d period of about 2.5%.

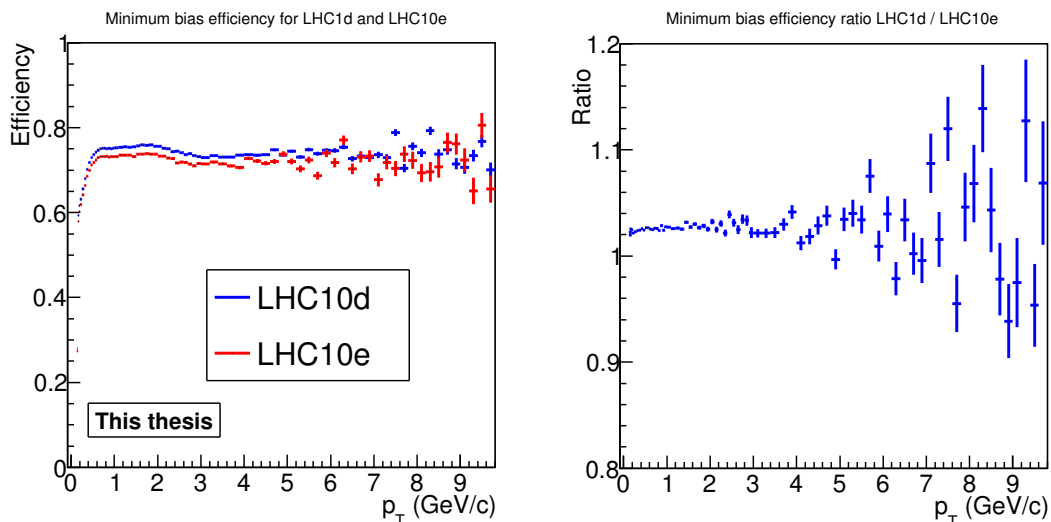


Figure 7.3: Minimum bias efficiency for LHC10d and LHC10e periods (left panel) and ratio between them (right panel).

The fully corrected transverse momentum spectra for all the multiplicity bins from the minimum bias and high multiplicity trigger are plotted in Figure 7.4. The high multiplicity bins are corrected with the efficiency from the LHC10d period due to lower statistical fluctuations. A 2.5% scaling factor has been applied to correct for the period bias shown in Figure 7.3.

7.2 Event Shape selected spectra

For all the multiplicity bins event shape cuts were applied according to the Table 6.2. The efficiency correction was done bin wise using the efficiencies from Figures 6.10, 6.14, 6.12, 6.16. The feed-down correction used was the one from minimum bias, the same as for the minimum bias multiplicity spectra.

7.2.1 Minimum Bias trigger

For the minimum bias multiplicity bins, the results for sphericity, directivity, thrust and Fox-Wolfram cuts are plotted in Figures 7.5, 7.6, 7.7 and 7.8. The multiplicity

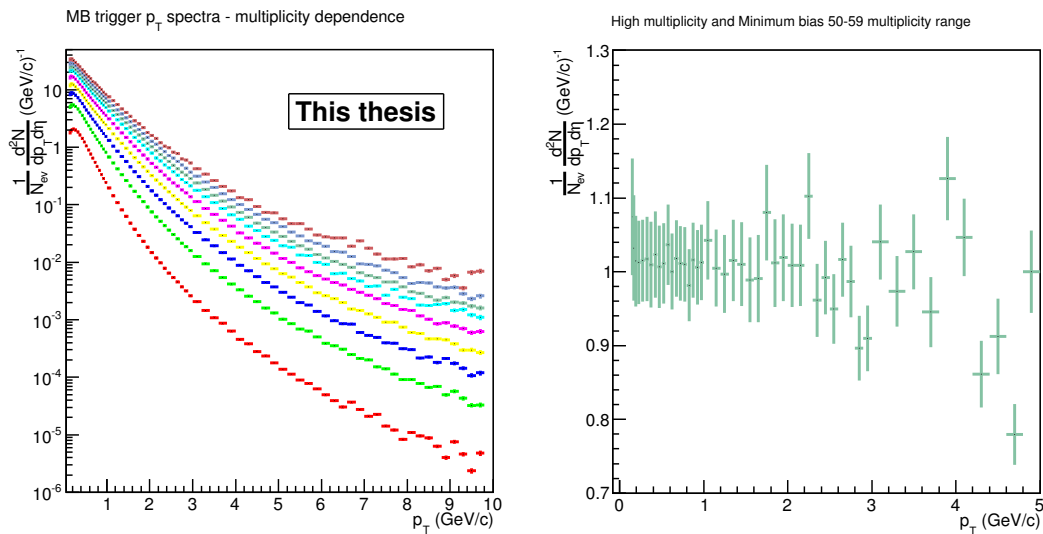


Figure 7.4: *Left panel*: transverse momentum spectra for the nine multiplicity bins listed in Table 6.1. Particle yield increases with the bin number. The lowest distribution (red) corresponds to bin 0 of minimum bias events. *Right panel*: ratio between the raw spectra in the same multiplicity range for the minimum bias and high multiplicity trigger.

bins are displayed as follows: the first three bins are plotted in order on the first row and the last three bin on the second row. All the spectra are normalized to the number of events analyzed in the corresponding class.

For all the event shape cuts, the spectra for “non-isotropic” events have long tails. The events labeled as “isotropic” have a “softer” shape.

7.2.2 High Multiplicity trigger

The same study was done on spectra selected with event shape cuts in high multiplicity bins. The results are shown in Figures 7.9-7.12

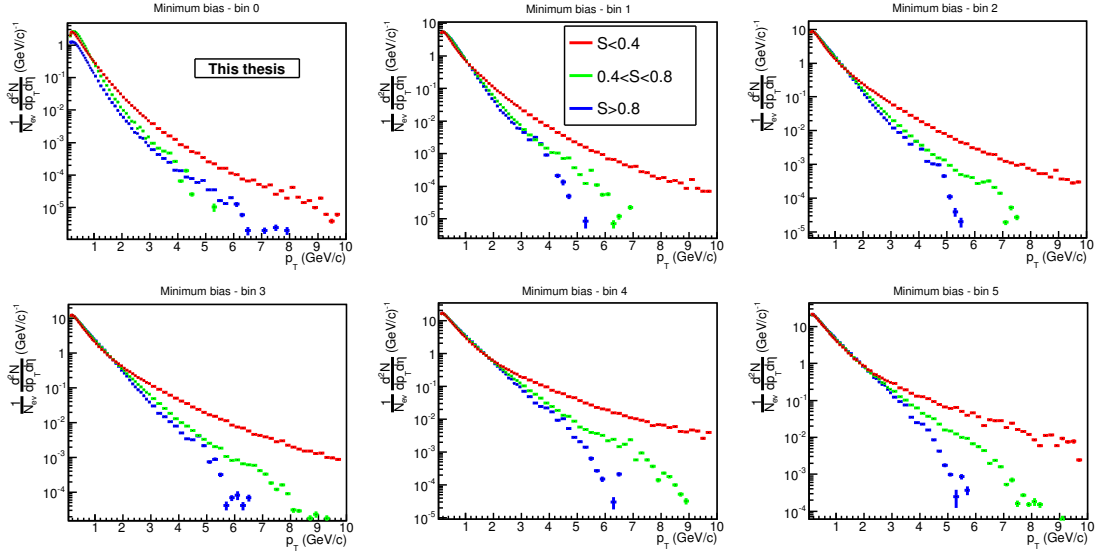


Figure 7.5: Transverse momentum spectra in six minimum bias bins and three sphericity cuts.

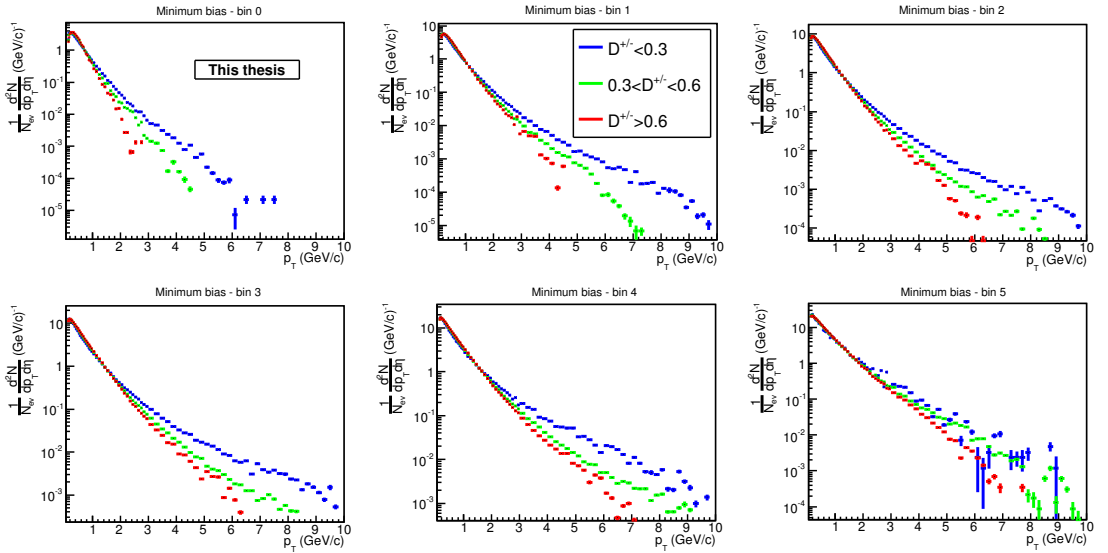


Figure 7.6: Transverse momentum spectra in six minimum bias bins and three directivity cuts.

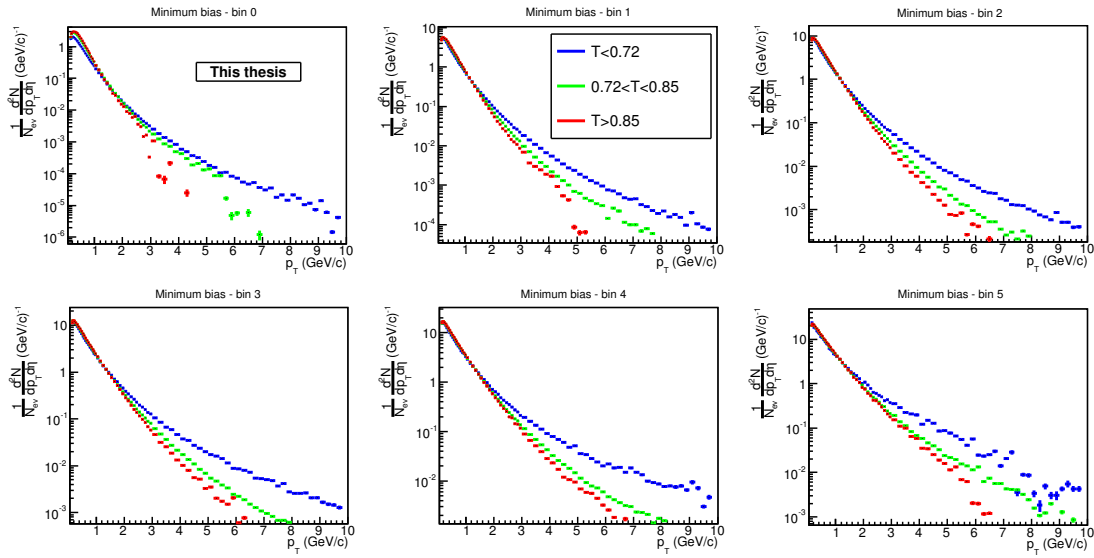


Figure 7.7: Transverse momentum spectra in six minimum bias bins and three thrust cuts.

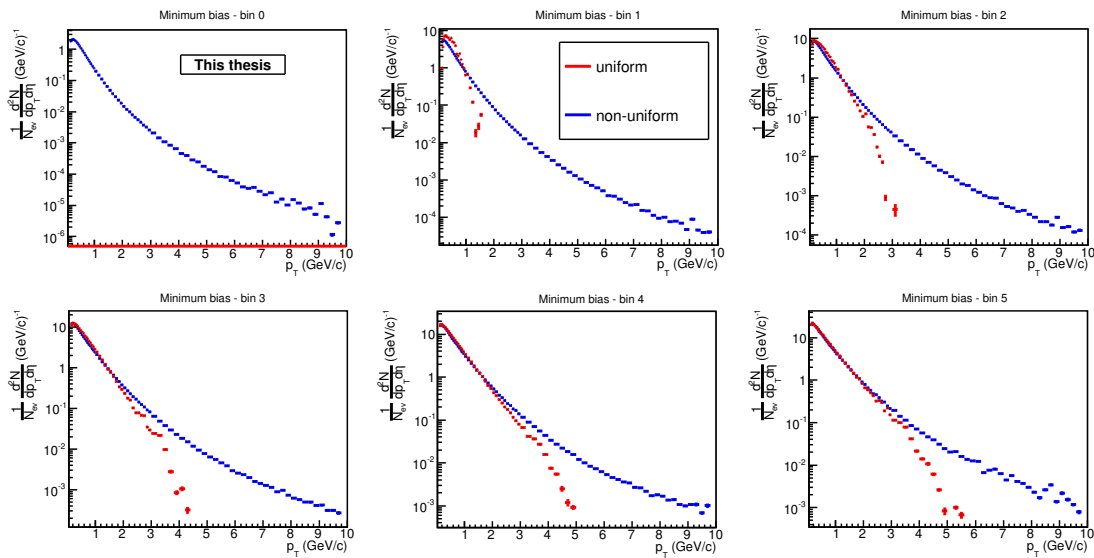


Figure 7.8: Transverse momentum spectra in six minimum bias bins and Fox-Wolfram moments cuts corresponding to isotropic and non-isotropic events.

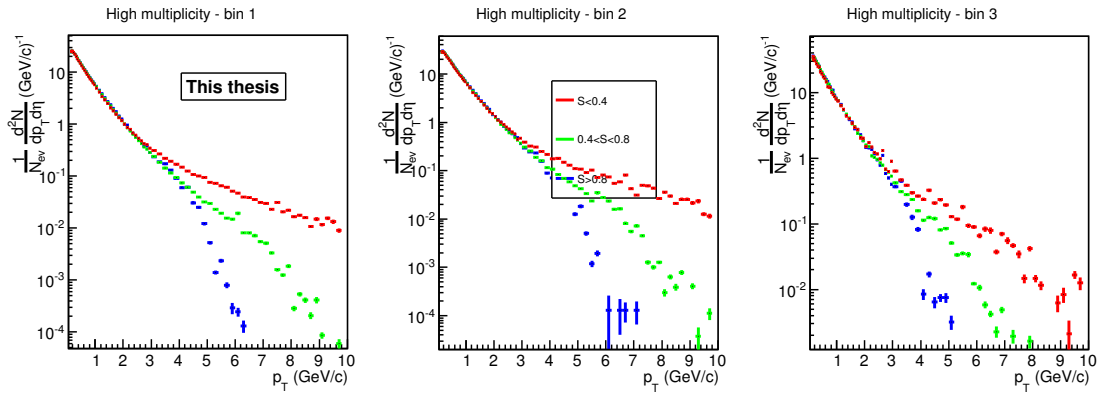


Figure 7.9: Transverse momentum spectra in three high multiplicity bins and three sphericity cuts.

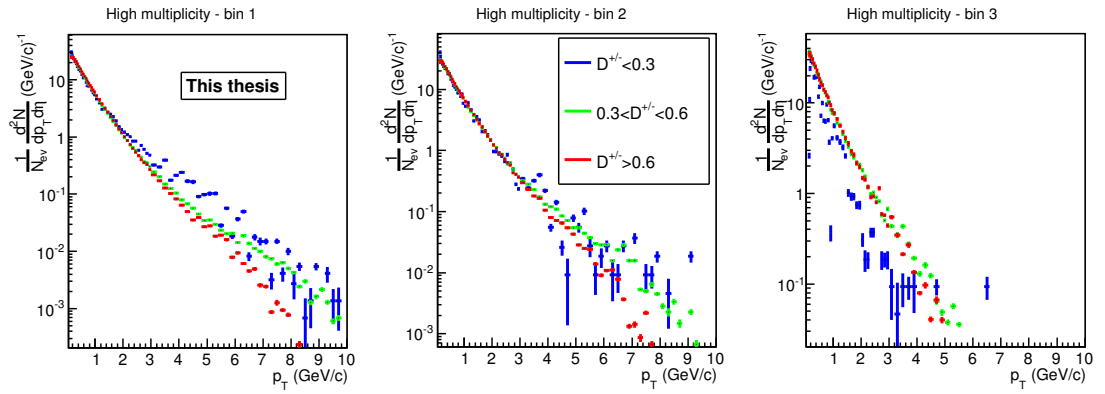


Figure 7.10: Transverse momentum spectra in three high multiplicity bins and three directivity cuts.

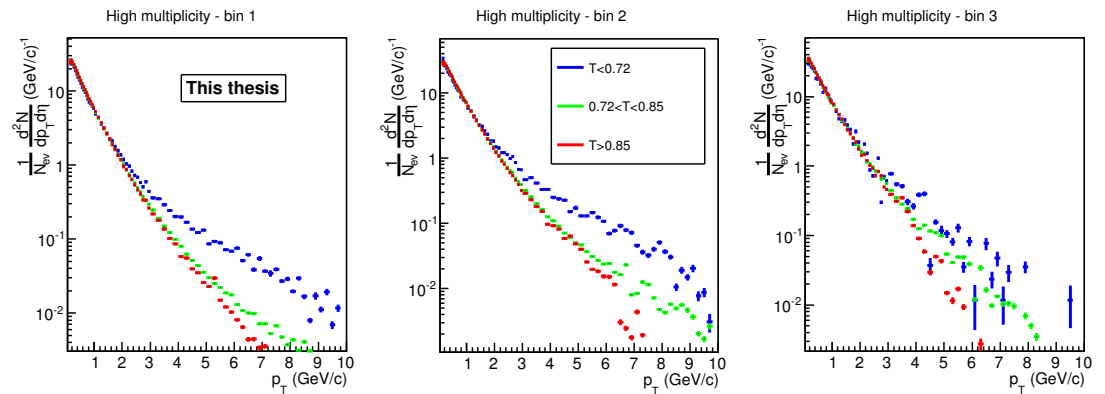


Figure 7.11: Transverse momentum spectra in three high multiplicity bins and three thrust cuts.

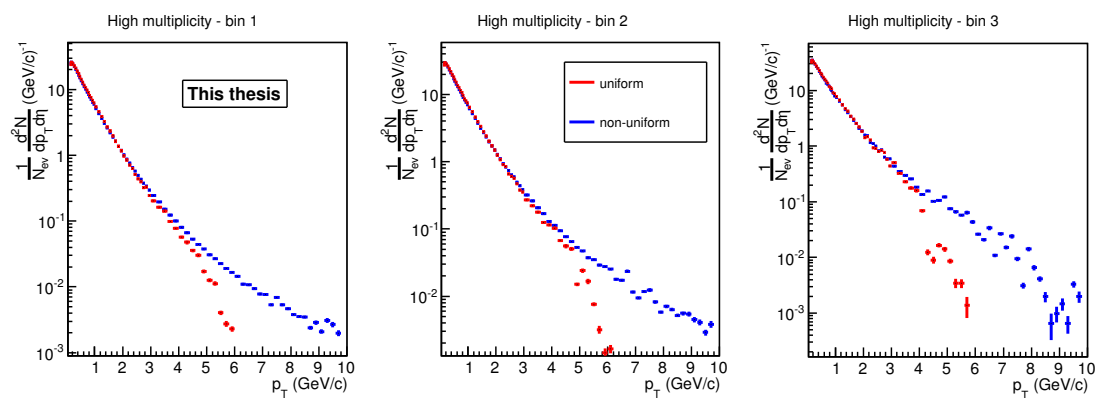


Figure 7.12: Transverse momentum spectra in three high multiplicity bins and Fox-Wolfram moments cuts corresponding to isotropic and non-isotropic events.

7.2.3 Mean transverse momentum - multiplicity dependence

The mean transverse momentum obtained using the Levy-Tsallis and Bylinkin fits, performed on two different ranges are plotted in the left panel of Figure 7.13. On the right panel, the mean p_T as a function of multiplicity from the fit using the Bylinkin - Rostovtsev parameterization is reported. The value of the mean p_T is evaluated on the fit range from 0 to 10 GeV/c. The systematic uncertainties are calculated using the difference between the mean p_T values obtained with the two fitting functions shown in the left panel on the same range (0-10 GeV/c).

Levy-Tsallis:

$$\frac{d^2 N}{dp_T d\eta} = p_T \frac{dN}{d\eta} \frac{(n-1)(n-2)}{nC(nC + m_0(n-2))} \left(1 + \frac{m_T - m_0}{nC}\right)^{-n} \quad (7.2)$$

Bylinkin and Rostovtsev:

$$\frac{d\sigma}{p_T dp_T} = A_e \exp(-E_T^{kin}/T_e) + \frac{A}{\left(1 + \frac{p_T^2}{T^2 \cdot n}\right)^n} \quad (7.3)$$

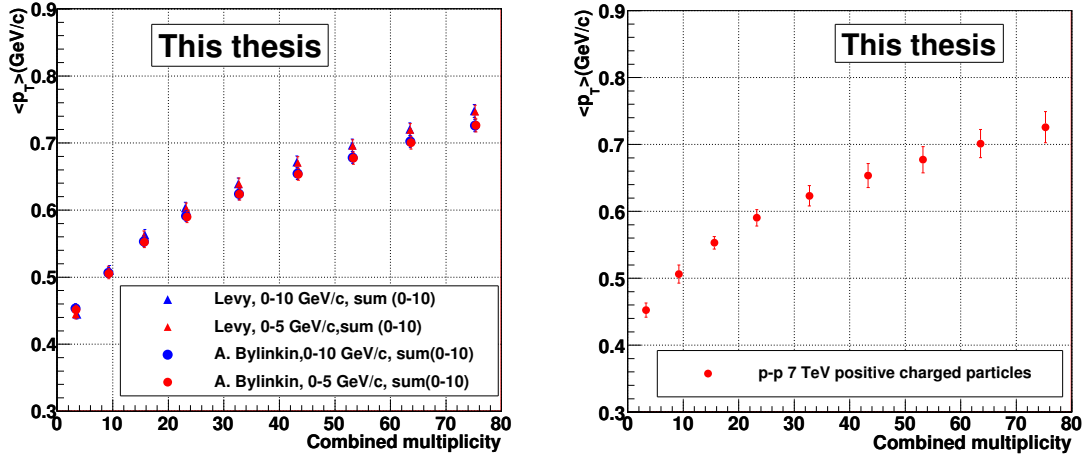


Figure 7.13: Mean transverse momentum for all multiplicity bins. The results are obtained from the fitting functions (see the text). On the right panel, the mean p_T obtained with the Bylinkin-Rostovtsev parameterization with the associated systematic errors is plotted.

The mean p_T for the minimum bias events is compared with the CMS results [CMS2010b] in Figure 7.15.

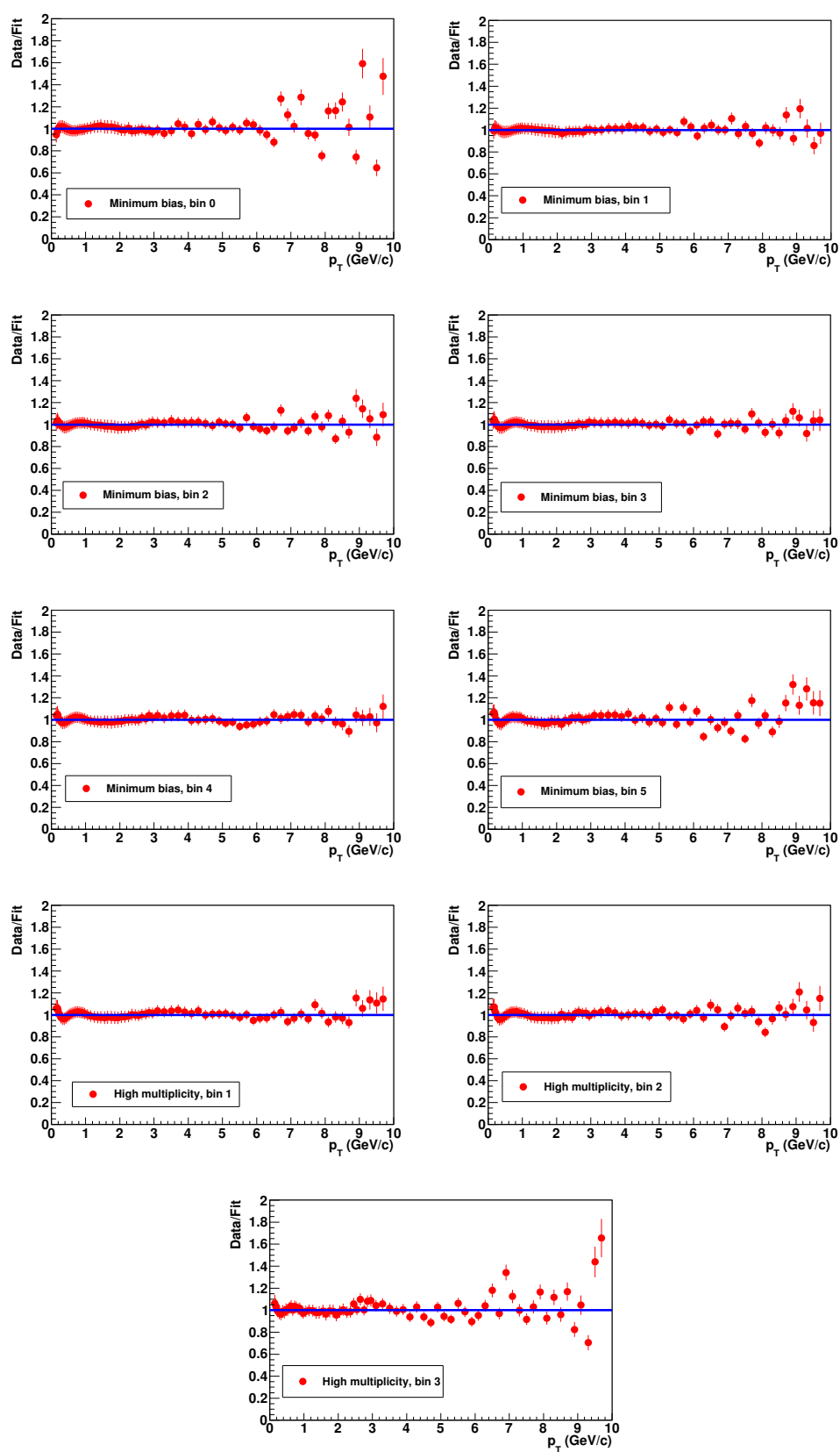


Figure 7.14: Fit quality for all six minimum bias and three high multiplicity bins.

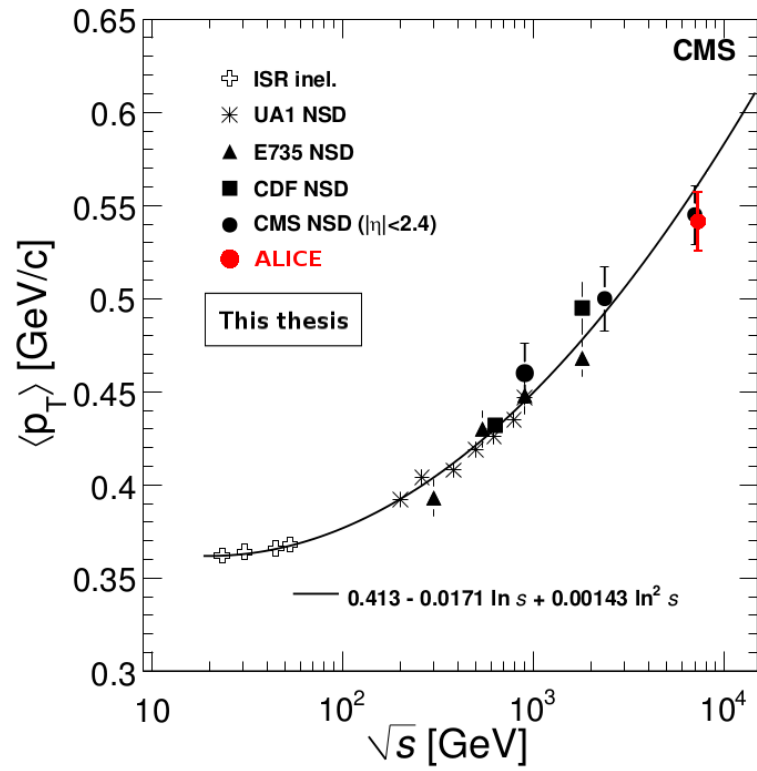


Figure 7.15: Mean transverse momentum for minimum bias events. The red point represents the result obtained in this analysis.

7.3 Towards isotropic events

The spectra for events close to azimuthal isotropy, selected with the sphericity, thrust, directivity and Fox-Wolfram moments are plotted in Figures 7.16 and 7.17. The slope of the transverse momentum distributions for the events selected in this way, is changing with the multiplicity. As it was shown in Chapter 5, Figure 5.31, based on Pythia model, the power law tails observed in Figure 7.4 where the p_T spectra for different multiplicity bins are presented, are drastically reduced in Figures 7.16 and 7.17 where nearly azimuthal isotropic events were selected.

Based on this observation, a fit of the p_T spectra for different multiplicities for events close to azimuthal isotropy using Boltzmann-Gibbs blast wave expression was done (eq. 2.5, the n parameter was fixed to 1). The fit quality in terms of data vs. fit ratios for different multiplicity bins can be followed in Figure 7.18. One could easily observe a clear improvement of the fit quality going from low to high multiplicity events.

The fit parameters are represented in a $T_{fo} - \langle \beta_T \rangle$ plot in the left panel of Figure 7.19. The range used for the fit is from 0 to 4 GeV/c. The fitting procedure is described in [Pop2013]. The results seems to indicate a decrease of the kinetic freeze-out temperature and an increase of the average expansion velocity with increasing multiplicity. This trend was observed in Au-Au collisions at RHIC energies and in Pb-Pb at 2.76 TeV at LHC (Figure 7.19, right panel). High multiplicity events selected as azimuthally isotropic by the transverse Fox-Wolfram moments have similar values for the kinetic freeze-out temperature and expansion velocity as observed for ultra-central Pb-Pb events.

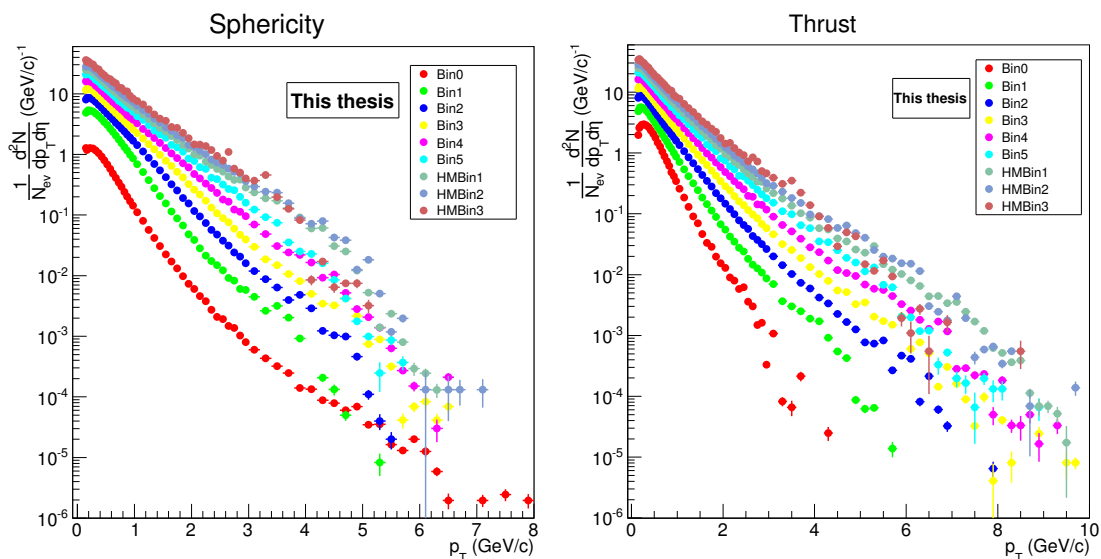


Figure 7.16: Transverse momentum spectra for minimum bias and high multiplicity events in multiplicity bins and sphericity (left panel) and thrust (right panel) selection for uniform events.

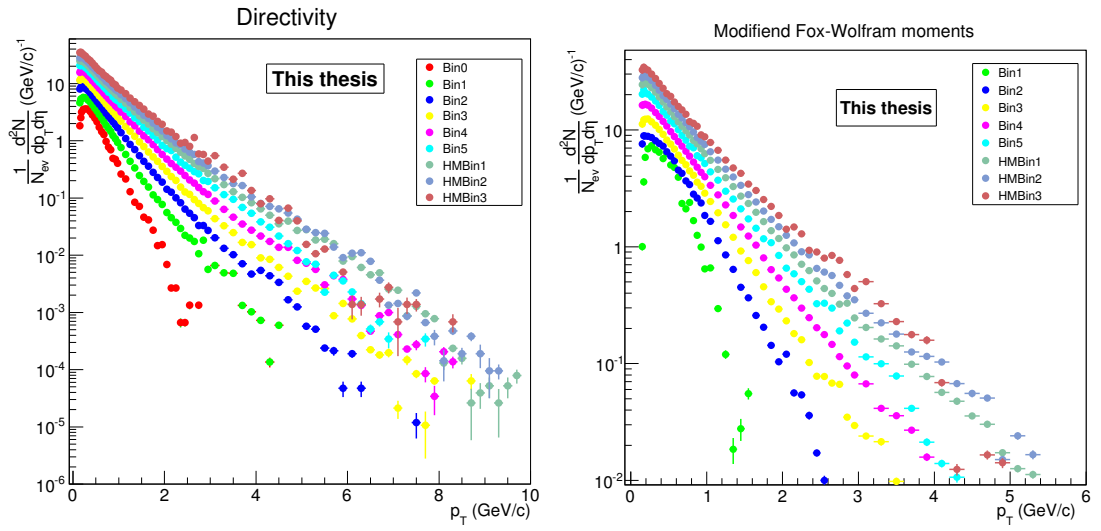


Figure 7.17: Transverse momentum spectra for minimum bias and high multiplicity events in multiplicity bins and directivity (left panel) and Fox-Wolfram moments (right panel) event selection for uniform events.

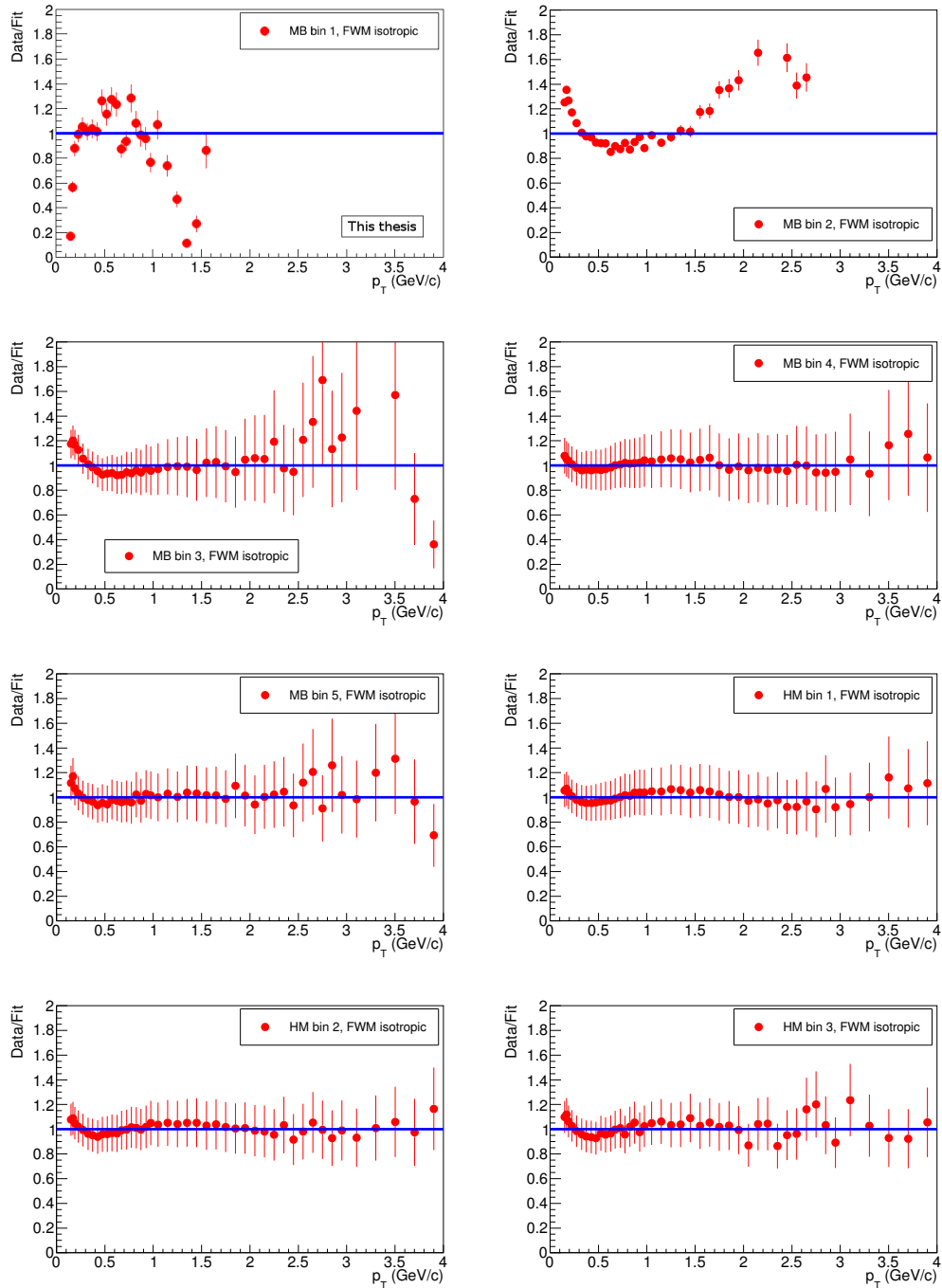


Figure 7.18: Fit quality in multiplicity bins plotted as the ratio between the data and the fit function for the Fox-Wolfram selected events.

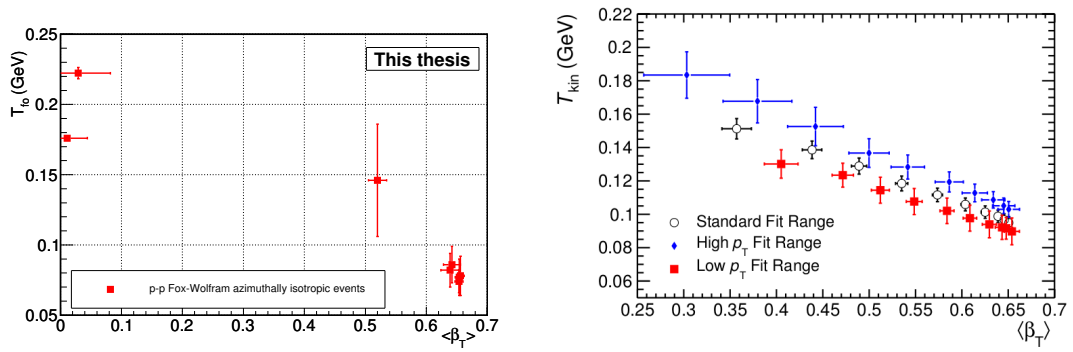


Figure 7.19: Freeze-out temperature vs. mean transverse velocity in Fox-Wolfram selected events (left panel). On the right panel, the results from balst wave fits of the Pb-Pb collisions at 2.76 TeV reported by ALICE collaboration [ALICE2013b].

Further investigations using the other global observables for selecting nearly azimuthal isotropic events and correlations with other type of studies, like small angle particle correlations, are mandatory in order to clarify the origin of the this trend observed in p-p collisions, similar with those observed in A-A, which were successfully explained by phenomenological models incorporating hydrodynamical expansion.

Chapter 8

Conclusions and perspectives

Transverse momentum of charged particles emerging from proton-proton collisions can reveal details on the underlying dynamics of the deconfined matter created during the collisions. Theoretical and experimental arguments towards the hydrodynamical behaviour of the partonic matter created in p-p collisions at high energies motivated the present studies and were presented in the second chapter. Multi-parton interactions followed by multiple partonic rescatterings may create the conditions needed for the hydrodynamical description to be used. Results from various studies showed a multiplicity scaling suggesting that the energy pumped into the system is strongly correlated with the multiplicity. Also, there are indications that the high multiplicity events suffer an expansion before hadronization phase. These considerations motivated the study of high multiplicity events.

The third chapter of the thesis briefly describes the experimental setup used for the acquisition of the analyzed data. First, the Large Hadron Collider is presented, followed by the ALICE experimental setup. The computational framework is also presented in this chapter.

The fourth chapter is dedicated to the analysis details. The data sample selection is discussed based on the trigger and pileup considerations. The event and track selection cuts used on the data and the Monte Carlo simulations are further presented. Two multiplicity estimators are introduced and their performance of estimating the generated multiplicity is evaluated through simulations. The combined multiplicity reproduces the simulated multiplicity with better accuracy than the global multiplicity estimator and was used for multiplicity bin selection in this thesis.

As it was argued in the Chapter 2, dedicated to the theoretical motivation, events can be labeled as "soft" and "hard" based on the momentum transfer between the interacting partons. The characteristics of these interactions are propagated to the final hadronic phase observed in the detector. The soft and hard components are characterized not only by different maximum transverse momentum values, but also by the azimuthal distribution of the particles. The hard events are less likely to be azimuthally isotropic since the jets are confined in a narrow region of space. On the other hand, the soft events should not manifest an anisotropy regarding the particle emission. In collectivity studies, based on the shape and the mean value of the transverse momentum spectra, the separation between soft and hard components

is mandatory. Several approaches found in the literature were investigated. The adopted strategy was to use several event shape observables due to their capabilities to characterize the energy distribution in the event. Event shape observables have been used in high energy physics for the past four decades across three orders of magnitude in the collision energy. The advantage of the event shape observables is that they are independent of the collision energy and do not have parameters to be tuned like in the case of jet finding algorithms.

In this thesis, sphericity, thrust, directivity and modified transverse Fox-Wolfram moments were selected and used for the event characterization. Their event selection performance was studied in the fifth chapter using Pythia simulations and also toy models. The performance of the event shape observables was evaluated using azimuthal distributions relative to the leading particle of the events and the thrust axis. Another criterion of evaluation was the capability to reject high momentum particles without introducing a spectra distortion. Thermal, Boltzmann blast wave and Tsallis distributions were used in the toy model. Spectra generation process used parameter values similar to those found in transverse momentum studies in proton-proton collisions at 7 TeV. The spectra simulated using the Tsallis distribution showed a good agreement with the experimental results found by ALICE in terms of mean sphericity, even if the used model is very simple. The selected spectra depend on the ESO used and on the event multiplicity. For all investigated observables, the spectra is less biased by the event shape selection toward high multiplicities.

The hard component is usually given by high energy jets. Experimental results from the ATLAS experiment show that the number of jets that may be present in an event decreases rapidly. Another toy model, used to evaluate how the jets can be eliminated from the data sample, by using the event shape observables, was studied in this thesis. When special requirements are fulfilled, events with three and four (simplified) jets can be identified as uniform by sphericity, thrust and directivity. Fox-Wolfram moments eliminate all such events in the used toy model.

Chapter 6 is dedicated to the efficiency and contamination estimation and systematic uncertainty evaluation. The efficiency was found to be multiplicity dependent when the global multiplicity estimator was used. For the combined multiplicity estimator, the multiplicity dependence of the efficiency is below 2% for the extreme bins. Similar results were obtained by using weighting functions based on the reconstructed multiplicity distribution.

The efficiency was also evaluated using events shape cuts in all the multiplicity bins. The efficiency is ESO dependent, but almost the same for all the event shape cuts for the high multiplicity events, at least in the low p_T region.

The final spectra were corrected also for the secondary products from weak decays and interaction with the material evaluated from DCA studies.

Chapter seven presents the obtained results for minimum bias, multiplicity and multiplicity combined with event shape selection. The p_T spectra for charged particles in p-p collisions at 7 TeV are presented up to 10 GeV/c, as a function of multiplicity. The multiplicity was estimated on $|\eta| < 0.8$, a rather large range of pseudo-rapidity, excluding in this way any autocorrelation bias. This explains the different behaviour of $\langle p_T \rangle$ as a function of multiplicity relative to similar studies made on rather narrow pseudo-rapidity range on which charge particle multiplicity

was considered. The minimum bias spectra is in good agreement with the results from another analysis group in ALICE. The $\langle p_T \rangle$ for minimum bias events obtained in this thesis is in very good agreement with the value reported by the CMS Collaboration.

The multiplicity dependent spectra show a clear shape modification from low to high multiplicity. Also, in every multiplicity bin, the obtained spectra for all the event shape cuts show different shapes.

Fits with Boltzmann-Gibbs Blast Wave (BGBW) expression, inspired by hydrodynamical models show a χ^2 which improves at large multiplicity. The fit quality and the trend of freeze out temperature - T_{fo} and β parameters in a two dimensional representation, similar with those obtained for Au+Au collisions at RHIC (200 A·GeV) and Pb+Pb collisions at LHC (2.76 A·TeV), can be considered as a signature of transverse flow in p+p collision at 7 TeV in high multiplicity events.

Preliminary results, in terms of p_T spectra using event shape selection indicate that indeed one could enhance the contribution of soft processes. This opens the perspective of continuing the studies presented in this thesis, aiming for new results which could unambiguously clarify the existence of deconfinement and subsequent collective type evolution already in p-p collisions at the LHC energies.

In the upcoming two years of the LHC technical shutdown, some of the ALICE data will be recalibrated and high statistics Monte Carlo runs will be produced. The combined multiplicity estimator will be available for LHC10b and LHC10c periods. These will increase the statistics and will allow better crosschecks on the pile-up effects and multiplicity efficiency dependence.

The LHC energy will increase after the technical shutdown to 14 TeV. The ALICE experiment will be upgraded in order to cope with higher luminosities. These changes will allow the usage of the high multiplicity trigger in high luminosity environment. Therefore, these studies will investigate with better accuracy more events close to azimuthal isotropy and higher multiplicity.

More studies must be performed in order to understand if the hydrodynamical approach can be used in high multiplicity proton-proton collisions. Statistical errors can be reduced if more data is reconstructed including the information on the combined multiplicity estimator. Also, for the high multiplicity period, full statistics for the Monte Carlo simulations will be useful in evaluating the efficiency using the anchored runs. Pileup effects, although very low, should be further investigated using a wider range of the μ parameter. More statistics will allow the analysis to be performed on even higher multiplicities.

The systematic uncertainty could be better evaluated, for example, by investigating the multiplicity dependence of the tracking efficiency. Also, the efficiency dependence on the event shape cut used in a given multiplicity bin must be investigated to see if spurious effects are not introduced by applying these cuts.

More realistic studies must be performed in order to understand the event selection based on the event shape observables. Two particle correlations studies of the event selection capabilities of the event shape observables must be extended for more event shape cut values.

Proving what is the mechanism behind the collectivity signals in proton-proton collisions is a challenge that must be addressed. Solving this problem will reveal

important insight on the phenomenology within the proton-proton collisions. The conclusions are extremely important for the interpretation of the heavy ion collisions. High multiplicity events, selected as azimuthally isotropic, were shown to be the most probable case to find collective behaviour in proton-proton collisions.

Bibliography

- [Aad2011] G. Aad et al. ATLAS Collaboration, A search for new physics in dijet mass and angular distributions in pp collisions at $\sqrt{s}=7$ TeV measured with the ATLAS detector, *New J. Phys.* **13** (2011) 053033; arXiv: 1012.5104 [hep-ex].
- [Aamodt2010] K. Aamodt et al. ALICE Collaboration, Transverse momentum spectra of charged particles in proton-proton collisions at $\sqrt{s}=900$ GeV with ALICE at the LHC, *Phys. Lett. B* **693** (2010) 53; K. Aamodt et al. ALICE Collaboration, Strange particle production in proton-proton collisions at $\sqrt{s}=0.9$ TeV with ALICE at the LHC. The ALICE Collaboration, *Eur. Phys. J. C* **71** (2011) 1594; K. Aamodt et al. ALICE Collaboration, Production of pions, kaons and protons in pp collisions at $\sqrt{s}=900$ GeV with ALICE at the LHC, *Eur. Phys. J. C* **71** (2011) 1655; arXiv: 1101.4110 [hep-ex].
- [Abbiendi2004] G. Abbiendi et al. OPAL Collaboration, Tests of models of color reconnection and a search for glueballs using gluon jets with a rapidity gap, *Eur. Phys. J. C* **35** (2004) 293-312; arXiv:0306021v1.
- [Abelev2007] B. I. Abelev et al. STAR Collaboration, Strange particle production in p+p collisions at $\sqrt{s} = 200$ GeV, *Phys. Rev. C* **75** (2007) 064901; arXiv:nucl-ex/0607033.
- [Acosta2002] D. Acosta et al. CDF Collaboration, Soft and hard interactions in ppbar collisions at $\sqrt{s}=1800$ and 630 GeV, *Phys. Rev. D* **65** (2002) 072005.
- [Adare2011] A. Adare et al. PHENIX Collaboration, Measurement of neutral mesons in p+p collisions at $\sqrt{s}=200$ GeV and scaling properties of hadron production, *Phys. Rev. D* **83** (2011) 052004;
- A. Adare et al., Identified charged hadron production in p+p collisions at $\sqrt{s} = 200$ and 62.4 GeV, *Phys. Rev. C* **83** (2011) 064903; arXiv: nucl-ex/0607033.
- [Affolder2002] A. A. Affolder et al. CDF Collaboration, Charged jet evolution and the underlying event in proton-antiproton collisions at 1.8 TeV, *Phys. Rev. D* **65** (2002) 092002.
- [Alard1992] J. P. Alard and the FOPI Collaboration, Midrapidity source of intermediate-mass fragments in highly central collisions of Au + Au at 150A MeV, *Phys. Rev. Lett.* **69** (1992) 889.

- [Alexopoulos1993] T. Alexopoulos et al. E735 Collaboration, Mass-identified particle production in proton-antiproton collisions at $\sqrt{s} = 300, 540, 1000,$ and 1800 GeV, Phys. Rev. D **48** (1993) 984.
- [ALICE1999] ALICE Collaboration, Technical Design Report of the Inner Tracking System (ITS), CERN / LHCC 9912, (1999).
- [ALICE2000] ALICE Collaboration, Technical Design Report of the Time Projection Chamber, CERN/LHCC 2000001 (2000).
- [ALICE2004] ALICE Collaboration. ALICE Physics Performance Report Volume I, J. Phys. G Nucl. Part. Phys., **30** (2004) 1517.
- [ALICE2006] Physics Performance Report, Volume II, J. Phys. G: Nucl. Part. Phys. **32** (2006) 1295.
- [ALICE2008] ALICE Collaboration, The ALICE experiment at the CERN LHC JINST **3** (2008).
- [ALICE2010] ALICE Collaboration, Charged-particle multiplicity measurement in proton-proton collisions at $\sqrt{s}=7$ TeV with ALICE at LHC, Eur. Phys. J. C **68** (2010) 345.
- [ALICE2011] K. Aamodt et al. ALICE Collaboration, Femtoscopy of pp collisions at $\sqrt{s} = 0.9$ and 7 TeV at the LHC with two-pion Bose-Einstein correlations, Phys. Rev. D **84** (2011) 112004.
- [ALICE2012a] ALICE Collaboration, Measurement of inelastic, single- and double-diffraction cross sections in proton-proton collisions at the LHC with ALICE, arxiv:1208.4968v1 [hep-ex] (2012).
- [ALICE2012b] ALICE Collaboration, Transverse sphericity of primary charged particles in minimum bias proton-proton collisions at $\sqrt{s}=0.9, 2.76$ and 7 TeV, Eur. Phys. C **72** (2012) 2124.
- [ALICE2013a] ALICE Collaboration, Measurement of the inclusive differential jet cross section in pp collisions at $\sqrt{s} = 2.76$ TeV, Phys. Lett. B Volume **722** (2013) Pages 262272.
- [ALICE2013b] ALICE Collaboration, Centrality Dependence of π, K, p Production in PbPb Collisions at $\sqrt{s_{NN}} = 2.76$ TeV, arXiv:1303.0737v1 [hep-ex].
- [AliEn] AliEn Framework <http://alien2.cern.ch/>
- [AliRoot] AliRoot environment <http://aliceinfo.cern.ch/Offline>
- [Alme2010] J. Alme et al., The ALICE TPC, a large 3-dimensional tracking device with fast readout for ultra-high multiplicity events, NIM A **622** (2010).
- [Alner1985] G. J. Alner et al. UA5 Collaboration, Kaon production in pp reactions at a centre-of-mass energy of 540 GeV, Nucl. Phys. B **258** (1985) 505.

- [Alver2010] B. Alver, G. Roland, Collision-geometry fluctuations and triangular flow in heavy-ion collisions, *Phys. Rev. C* **81** 054905 (2010); arxiv:1003.0194v3 [nucl-th].
- [Andrei2009] C. Andrei, I. Berceanu, A. Herghelegiu, M. Petrovici, A. Pop, C. Schiaua, Azimuthal isotropic expansion in highly central collisions, ALICE Week Oct 2009. <https://indico.cern.ch/getFile.py/access?contribId=12&resId=1&materialId=slides&confId=70834>
- [Andrei2012] C. Andrei, I. Berceanu, A. Bercuci, A. Herghelegiu, F. Noferini, M. Petrovici, A. Pop Transverse momentum distributions of pions, kaons and protons for high multiplicity and close to azimuthal isotropic events in 7 TeV pp collisions with the ALICE experiment at the LHC material and weak decays contamination ALICE Internal Note https://twiki.cern.ch/twiki/pub/ALICE/PWGLFPAGSPECTRAMultiplicityEventShapePP7/coll_ph_pp_ALICE_internal_note_3_04042012.pdf
- [Ansari1987] R. Ansari et al., *Z. Phys. C* **36** (1987) 175.
- [Ansorge1986] R. E. Ansorge et al. (UA5 Collaboration), *Phys. Lett. B* **167** (1986) 476.
- [ATLAS2011a] ATLAS Collaboration, Measurement of the Inelastic Proton-Proton Cross-Section at $\sqrt{s}=7$ TeV with the ATLAS Detector, *Nat. Commun.* **2** (2011) 463, arxiv:1104.0326 [hep-ex].
- [ATLAS2011b] ATLAS Collaboration, Measurement of multi-jet cross sections in proton-proton collisions at a 7 TeV center-of-mass energy, *Eur. Phys. J. C* **71** (2011) 1763.
- [ATLAS2012] ATLAS Collaboration, Observation of a new particle in the search for the Standard Model Higgs boson with the ATLAS detector at the LHC, *Phys. Lett. B* **716** (2012) 1-29;
- [Banderlik1979] R. Banderlik et al. TASSO Collab., Evidence for planar events in e^+e^- annihilation at high energies, *Phys. Lett. B* **86** (1979) 243;
- [Banfi2004] A. Banfi, Resummed event shapes at hadron-hadron colliders, *JHEP* **0408** (2004) 062, arXiv:hep-ph/0407287v3.
- [Banfi2010] A. Banfi, Phenomenology of event shapes at hadron colliders, arXiv:1001.4082 [hep-ph] (2010).
- [Barber1979] D. P. Barber et al. MARK-J Collab., Discovery of Three-Jet Events and a Test of Quantum Chromodynamics at PETRA, *Phys. Rev. Lett.* **43** (1979) 830;
- [Bartalini2011] P. Bartalini et al., Multi-Parton Interactions at the LHC, arxiv:1111.0469v2 (2011).

- [Bartel1980] W. Bartel et al. JADE Collab., Observation of planar three-jet events in e^+e^- annihilation and evidence for gluon bremsstrahlung, *Phys. Lett. B* **91** (1980) 142.
- [Beck2002] C. Beck, Non-additivity of Tsallis entropies and fluctuations of temperature, *Europhys. Lett.* **57** (3) (2002) 329; C. Beck, E. G. D. Cohen, Superstatistics, *Physica A* **322** (2003) 267.
- [Beckmann1987] P. Beckmann et al., Collective Azimuthal Alignment in Relativistic Heavy Ion Reactions, *Mod. Phys. Lett. A* **2**, 163 (1987);
- [Berger1979] Ch. Berger et al. PLUTO Collab., Evidence for gluon bremsstrahlung in e^+e^- annihilations at high energies, *Phys. Lett. B* **86** (1979) 418;
- [Bernaciak2013] C. Bernaciak et al., Fox-Wolfram moments in Higgs physics, *Phys. Rev. D* **87** (2013) 073014, arXiv:1212.4436 [hep-ph]
- [Bjorken1970] J.D. Bjorken and S.J. Brodsky, Statistical Model for Electron-Positron Annihilation into Hadrons, *Phys. Rev.* **D1** (1970) 1416.
- [Bjorken1983] J. D. Bjorken, Highly relativistic nucleus-nucleus collisions: The central rapidity region, *Phys. Rev. D* **27** 140 (1983).
- [Bozek2010] P. Bozek, Observation of the collective flow in proton-proton collisions, *Acta Phys. Pol. B* **41** (2010) 837.
- [Brandt1964] S. Brandt, Ch. Peyrou, R. Sosnowski and A. Wroblewski, The principal axis of jets – an attempt to analyse high-energy collisions as two-body processes, *Phys. Lett.* **12** (1964) 57;
- [Broniowski2009] W. Broniowski et al., GLISSANDO: GLauber Initial-State Simulation AND m0re, *Comp. Phys. Comm.* **180** (2009) 69, arXiv:0710.5731v3 [nucl-th].
- [Butterworth2012] J. M. Butterworth, G. Dissertori and G. P. Salam, Hard Processes in Proton-Proton Collisions at the Large Hadron Collider, *Annu. Rev. Nucl. Part. Sci.* **62** 2012 387405.
- [Bylinkin2010] A. A. Bylinkin and A. A. Rostovtsev, Systematic studies of hadron production spectra in collider experiments, arXiv:1008.0332 [hep-ph] (2010).
- [Bylinkin2012] A. A. Bylinkin, A. A. Rostovtsev, An analysis of charged particles spectra in events with different charged multiplicity, arXiv:1205.4432v1 [nucl-th] (2012).
- [Cacciari2011] M. Cacciari et al., FastJet user manual arXiv:1111.6097 [hep-ph].
- [Chatrchyan2011] S. Chatrchyan et al. CMS Collaboration, Charged particle transverse momentum spectra in pp collisions at $\sqrt{s} = 0.9$ and 7 TeV, *JHEP* **08** (2011) 086.

- [Claymans2012] J. Claymans, The Tsallis Distribution at the LHC, arXiv:1210.7464v1 [hep-ph] (2012).
- [CMS2010a] CMS Collaboration, Observation of Long-Range Near-Side Angular Correlations in Proton-Proton Collisions at the LHC, JHEP **9** (2010) 091, arxiv:1009.4122v1 [hep-ex].
- [CMS2010b] CMS Collaboration, Transverse-momentum and pseudorapidity distributions of charged hadrons in pp collisions at $\sqrt{s} = 7$ TeV, arXiv:[hep-ex]1005.3299v1 (2010).
- [CMS2012] CMS Collaboration, Observation of a new boson at a mass of 125 GeV with the CMS experiment at the LHC, Phys. Lett. B **716** (2012) 30.
- [CMS2013] CMS Collaboration, Measurement of the inelastic proton-proton cross section at $\sqrt{s} = 7$ TeV, Phys. Lett. B **722** (2013) 5, arxiv:1210.6718v2 [hep-ex].
- [Cooper1974] F. Cooper, G. Frye, Single-particle distribution in the hydrodynamic and statistical thermodynamic models of multiparticle production, Phys. Rev. D **10**, 186 (1974).
- [Dreascher2001] H. J. Dreascher et al., Parton-based Gribov-Regge theory, Phys. Rept. **350** (2001) 93-289.
- [Engel1996] R. Engel, PHOJET manual (program version 1.05c, June 96), <http://www-ik1.fzk.de/~engel/phojet.html>
- [Fahri1977] E. Fahri, Phys. Quantum Chromodynamics Test for Jets, Rev. Lett. **39** (1977) 1587.
- [Fermi1951] E. Fermi, Angular Distribution of the Pions Produced in High Energy Nuclear Collisions, Phys. Rev. **81** (1951) 683.
- [Filed1997] R. D. Field et al., Topological analysis of the top quark signal and background at hadron colliders, Phys. Rev. D **55** (1997) 5685.
- [Florkowski2010] W. Florkowski, Phenomenology of Ultra-Relativistic Heavy-Ion Collisions, ed. World Scientific Publishing (2010).
- [Fox-Wolfram1979] G.C. Fox and S. Wolfram, Event shapes in e^+e^- annihilation, Nucl. Phys. **B149** (1979) 413.
- [Gale2013] C. Gale, S. Jeon, B. Schenke, Hydrodynamic Modeling of Heavy-Ion Collisions, Int. J. Mod. Phys. A **28** (2013) 1340011; arXiv:1301.5893 [nucl-th].
- [Geant4] <http://geant4.cern.ch/>
- [Glauber1959] R. J. Glauber, Lectures in Theoretical Physics ed. W. E. Brittin and L. G. Dunham (New York: Interscience) (1959) p 315;
R. J. Glauber, High Energy Physics and Nuclear Structure, ed. G. Alexander (Amsterdam: North-Holland) (1967) p 311;

- R. J. Glauber, High Energy Physics and Nuclear Structure ed. S. Devons (New York: Plenum) (1970) p 207.
- [Gribov1983] L.V. Gribov et al., Semihard processes in QCD, Phys. Rep. **100** (1983) 1.
- [Hagedorn1971] R. Hagedorn Nuovo Cim. Suppl **3**, 147 (1965); R. Hagedorn: Thermodynamics of strong interactions, report CERN 71-12 (1971);
R. Hagedorn Riv. Nuovo Cim. Vol. **6** (1983) 1.
- [Hanson1975] G. Hanson et al. SLAC-LNL Collab., Evidence for jet structure in hadron production by e^+e^- annihilation, Phys. Rev. Lett. **35** (1975) 1609.
- [Herghelegiu2012] A. Herghelegiu for NIHAM working group, Transverse momentum distributions of pions, kaons and protons for high multiplicity and close to azimuthal isotropic events in 7 TeV pp collisions with the ALICE experiment at the LHC - Multiplicity dependence of the efficiency correction, ALICE Internal Note https://twiki.cern.ch/twiki/pub/ALICE/PWGLFPAGSPECTRAMultiplicityEventShapePP7/coll_ph_pp_ALICE_analysis_note_4_04042012_v2.pdf
- [Huovinen2006] P. Huovinen, P.V. Ruuskanen, Hydrodynamic Models for Heavy Ion Collisions Annual Review of Nuclear and Particle Science, **56** (2006) 163-206.
- [Kagiama1989] S. Kagiama et al., A Signal of Hydrodynamical Transverse Flow in High Energy Hadronic Collisions, Progr. Theor. Phys. **81** (1989) 266.
- [Kalweit2008] A. Kalweit. Energy Loss Calibration of the ALICE Time Projection Chamber, Master thesis, University of Darmstadt (Germany), 2008.
- [Karsch2000] F. Karsch, E. Laermann, A. Peikert, C. Schmidt, S. Stickan, QCD thermodynamics with 2 and 3 quark flavors, arXiv:0010027 [hep-lat] (2000).
- [Khachatryan2010] V. Khachatryan et al. CMS Collaboration, Transverse-Momentum and Pseudorapidity Distributions of Charged Hadrons in pp Collisions at $\sqrt{s} = 7$ TeV, JHEP **02** (2010) 041 and Phys. Rev. Lett. **105** (2010) 022002; arXiv: 1102.4282 [hep-ex].
- [Lacey2009] Roy A. Lacey, 25th Winter Workshop on Nuclear Dynamics, Big Sky Feb. 1-8, 2009.
- [Landau1953] L. D. Landau, Izv. Akad. Nauk SSSR **17** (1953) 51.
- [Landau1955] S. Z. Belenkij and L. D. Landau, Usp. Fiz. Nauk **56** (1955) 309; Nuovo Cimento Suppl. **3** (1956) 15.
- [Leeuwen2011] Marco van Leeuwen for the ALICE collaboration, (Low momentum) Hadron-Nucleus interactions in ALICE, LHC Detector Simulation workshop 6-7 October 2011.

- [LHC] <http://home.web.cern.ch/about/accelerators/large-hadron-collider>
- [Monalisa] <http://pcalimonitor.cern.ch>
- [Ortiz2013] A. Ortiz Velasquez et al., Color reconnection and flow-like patterns in pp collisions, arXiv:1303.6326 [hep-ph] (2013).
- [Otwinowski] private communication with from Jacek Otwinowski.
- [Paic2005] G. Paic, P. Skowronski, Effect of hard processes on momentum correlations in pp and pbar p collisions, J. Phys. G **31** (2005) 1045.
- [PDG] J. Beringer et al. (Particle Data Group), Review of Particle Physics, Phys Rev. D **86** (2012) 010001.
- [Petrovici2009] M. Petrovici, A. Pop, Collective Phenomena in Heavy Ion Collisions, arXiv:0904.3666 (2009).
- [Pierog2013] T. Pierog et al., EPOS LHC: test of collective hadronization with LHC data, arXiv:1306.0121v1 [hep-ph] (2013).
- [Pop2013] A. Pop, C. Andrei, I. Berceanu, A. Bercuci, A. Herghelegiu, M. Petrovici, Boltzmann Blast Wave (BBW) fits, Spectra working group, March 1, 2013, <https://indico.cern.ch/getFile.py/access?contribId=3&sessionId=0&resId=0&materialId=slides&confId=238899>
- [Reisdorf1999] W. Reisdorf et al. FOPI Collaboration, Clusters and nuclear flow, Presented at CLUSTER '99, Rab, Island of Rab, June 14-19, 1999.
- [Schenke2012] B. Schenke et al., Fluctuating Glasma Initial Conditions and Flow in Heavy Ion Collisions, Phys. Rev. Lett. **108** (2012) 252301; arXiv:1202.6646 [nucl-th].
- [Schneidermann1993] E. Schneidermann et al. Thermal phenomenology of hadrons from 200A GeV S+S collisions, Phys. Rev. C **48** (1993) 2462.
- [Shahoyan] R. Shahoyan, ALICE internal communication <https://indico.cern.ch/getFile.py/access?contribId=0&sessionId=0&resId=1&materialId=slides&confId=145707>
- [Siemens1979] P. J. Siemens. J. O. Rasmussen, Evidence for a Blast Wave from Compressed Nuclear Matter, Phys. Rev. Lett. **42** (1979) 880.
- [Sjöstrand1987] T. Sjöstrand et al., A multiple-interaction model for the event structure in hadron collisions, Phys. Rev. D **36** (1987) 2019.
- [Sjöstrand2004] T. Sjöstrand, P. Z. Skands, Multiple Interactions and the Structure of Beam Remnants, JHEP **0403** (2004) 053; arXiv:hep-ph/0402078v2.

- [Sjöstrand2008] [http://home.thep.lu.se/~\sim\\$torbjorn/Pythia.html](http://home.thep.lu.se/~\sim$torbjorn/Pythia.html); T. Sjostrand, S. Mrenna, P. Skands, A Brief Introduction to PYTHIA 8.1, *Comput. Phys. Commun.* **178** (2008) 852, arxiv:0710.3820v1 [hep-ph].
- [Sterman2004] G. Sterman, QCD and Jets, arxiv:0412013v1 [hep-ph] (2004).
- [Tang2009] Z. Tang et al., Spectra and radial flow at RHIC with Tsallis statistics in a Blast-Wave description, *Phys. Rev. C.* **79** (2009) 051901, arxiv:0812.1609v2 [nucl-th].
- [Tsallis1988] C. Tsallis, Possible generalization of Boltzmann-Gibbs statistics, *J. Stat. Phys.* **52** (1988) 479;
C. Tsallis, Nonadditive entropy: The concept and its use, *Eur. Phys. J. A* **40** (2009) 257.
- [Walker2004] W. D. Walker, Multiparton interactions and hadron structure, *Phys. Rev. D* **69** (2004) 034007.
- [Wang1989] X. Wang, R. C. Hwa, Effect of jet production on the multiplicity dependence of average transverse momentum, *Phys. Rev. D* **39** (1989) 187.
- [Werner2011] K. Werner, I. Karpenko, T. Pierog, M. Bleicher, and K. Mikhailov, Evidence for hydrodynamic evolution in proton-proton scattering at 900 GeV, *Phys. Rev. C* **83** (2011) 044915.
- [Wilk2009] G. Wilk et al., Power laws in elementary and heavy-ion collisions. A story of fluctuations and nonextensivity?, *Eur. Phys. J. A* **40** (2009) 299; arXiv:0810.2939.
- [Wong2012] C. Y. Wong, Tsallis Fits to p_T Spectra for pp Collisions at LHC, *Acta Physica Polonica B* **42** (2012) 2047, arxiv:1210.3661v3 [hep-ph];

List of Figures

1.1	Phase space diagram of strongly interacting matter.	2
2.1	Initial energy density estimation in a central Au-Au collision. On the z axis, the energy density is represented. The calculation was performed based on the Glauber model [Schenke2012].	6
2.2	Mean transverse momentum as a function of \sqrt{s} . The results at 300, 450, 1000 and 1800 GeV are reported by E735 Collaboration [Alexopoulos1993].	7
2.3	Mean transverse momentum as a function of incident energy for pions (circles) and kaons (triangles). Calculations for solid lines include collective expansion. Dashed line is the theoretical prediction without transverse velocity [Kagiyama1989].	8
2.4	Schematic view of a double parton-parton interaction. Picture from [Sjöstrand2004].	9
2.5	Multi-parton cross section as a function of collision energy. σ_1 , σ_2 and σ_3 represent the cross section for one, two and three multiplarton interactions. Picture from [Walker2004]. Quality of the picture has been enhanced for clarity.	10
2.6	Transverse momentum in "soft" (left panel) and "hard" (right panel) events obtained by the CDF collaboration [Acosta2002]. Two energies are shown: 630GeV (full symbols) and 1800GeV (empty symbols). . .	12
2.7	Mean transverse momentum in "soft" (left panel) and "hard" (right panel) events obtained by the CDF collaboration [Acosta2002] at 630 GeV (full symbols) and 1800 GeV (empty symbols). Multiplicity scaling can be observed only for the soft events.	13
2.8	Moments of the spherical decomposition of correlation functions for events with $12 < N_{ch} < 16$ with $0.3 < k_T < 0.4$ GeV/c. Collisions at 0.9 TeV are plotted with open simbols; the closed symbols are used for 7 TeV collisions. Figure from [ALICE2011].	15
2.9	Parton ladder mechanism for elementary hadron interaction in EPOS LHC model (left panel). Space time evolution of a hadronic interaction in EPOS (right panel). Pictures from [Pierog2013].	18
2.10	Pion, kaon and proton mean transverse momentum vs. multiplicity in Pythia 8 with and without color reconnection (full and, respectively, empty symbols). Picture from [Ortiz2013].	19
3.1	Schematic view of the LHC accelerator system. Picture from [LHC]. .	22

3.2	Schematic view of the ALICE experimental setup.	23
3.3	Schematic view of the ALICE Inner Tracking System.	24
3.4	Schematic view of the ALICE Time Projection Chamber.	26
3.5	Energy loss versus momentum in the ALICE TPC for 7 TeV pp collisions. The lines are the theoretical Bethe-Bloch predictions for dE/dx . Figure ALI-PERF-4849 from ALICE figure repository.	27
3.6	General view of data main processing stages in AliRoot.	28
3.7	General view of the AliRoot Virtual Monte Carlo. The independence of the users code on the packages used can be observed.	29
4.1	Minimum Bias (in blue) and High Multiplicity (in red) trigger combined multiplicity distributions (left panel) and their ratio (right panel).	34
4.2	Vertex distribution along the beam axis - z for Pythia anchor runs (blue) and data (red) for the LHC10d period. The two distributions are normalized to the corresponding highest value.	35
4.3	Definition of the DCA - distance of closest approach.	36
4.4	Correlation matrix for the Global Multiplicity estimator. Generated multiplicity represents the primary particle multiplicity obtained from Monte Carlo generator. Global multiplicity is estimated after the reconstruction of the simulated events.	37
4.5	Combined multiplicity estimation algorithm.	38
4.6	Correlation matrix for the Combined Multiplicity estimator.	39
4.7	Bin limit estimation for the combined multiplicity estimator.	39
5.1	Directivity for particles with negative η vs. directivity for positive η for Minimum Bias trigger (left panel) and High Multiplicity trigger (right panel).	43
5.2	Linear sphericity versus sphericity for MB (left) and HM (right) triggers.	45
5.3	Example of a high multiplicity event ($n_{ch} = 42$) with uniform particle distribution.	49
5.4	Example of a jet-like event with $n_{ch} = 55$	50
5.5	Reconstructed values for Sphericity, Thrust, Directivity and Recoil vs. the simulated values in the same Pythia events.	51
5.6	Multiplicity dependence of sphericity, thrust, directivity and recoil. With red lines, the profiles (on x axis) of the distributions are shown.	52
5.7	Profiles for Minimum Bias (blue) and High Multiplicity trigger (red) for sphericity, thrust, directivity and recoil.	53
5.8	Sphericity, thrust and directivity profile ratio (for Minimum Bias) between data and Pythia simulations.	54
5.9	Fox-Wolfram moments multiplicity dependence.	55
5.10	Fox-Wolfram moments yields in different multiplicity bins.	56
5.11	Particle distribution relative to the thrust axis \vec{n}_T for sphericity, thrust and directivity azimuthally isotropic selected events. All the distributions are normalized.	57
5.12	Particle distribution relative to the leading particle for minimum bias events.	59

5.13 Particle distribution relative to the leading particle for high multiplicity events ($N_{ch} > 40$).	60
5.14 Particle distribution relative to the leading particle for high multiplicity events ($N_{ch} > 40$) and Fox-Wolfram moments selection.	60
5.15 Sphericity and thrust (left) and FWM(right) for N equidistant particles.	61
5.16 Directivity selection on random thermal simulated distribution. The rows correspond to multiplicity values of 5, 10, 20, 40 and 60 from top to bottom.	63
5.17 Thrust selection on random thermal simulated distribution. The rows correspond to multiplicity values of 5, 10, 20, 40 and 60 from top to bottom.	64
5.18 Sphericity selection on random thermal simulated distribution. The rows correspond to multiplicity values of 5, 10, 20, 40 and 60 from top to bottom.	65
5.19 Fox-Wolfram moments selection on random thermal simulated distribution. The rows correspond to multiplicity values of 5, 10, 20, 40 and 60 from top to bottom.	66
5.20 Directivity selection on random Boltzmann-Gibbs blast wave simulated distribution. The rows correspond to multiplicity values of 5, 10, 20, 40 and 60 from top to bottom.	67
5.21 Thrust selection on random Boltzmann-Gibbs blast wave simulated distribution. The rows correspond to multiplicity values of 5, 10, 20, 40 and 60 from top to bottom.	68
5.22 Sphericity selection on random Boltzmann-Gibbs blast wave simulated distribution. The rows correspond to multiplicity values of 5, 10, 20, 40 and 60 from top to bottom.	69
5.23 Fox-Wolfram moments selection on random Boltzmann-Gibbs blast wave simulated distribution. The rows correspond to multiplicity values of 5, 10, 20, 40 and 60 from top to bottom.	70
5.24 Directivity selection on random Tsallis simulated distribution. The rows correspond to multiplicity values of 5, 10, 20, 40 and 60 from top to bottom.	71
5.25 Thrust selection on random Tsallis simulated distribution. The rows correspond to multiplicity values of 5, 10, 20, 40 and 60 from top to bottom.	72
5.26 Sphericity selection on random Tsallis simulated distribution. The rows correspond to multiplicity values of 5, 10, 20, 40 and 60 from top to bottom.	73
5.27 Fox-Wolfram moments selection on random Tsallis simulated distribution. The rows correspond to multiplicity values of 5, 10, 20, 40 and 60 from top to bottom.	74
5.28 Mean sphericity (left), thrust (middle) and directivity (right) for all (black), soft (blue) and hard (red) events. The soft and hard events are identified according to the leading particle transverse momentum.	75

5.29	Mean sphericity for “soft” (left), “hard” (middle) and all events (right). The soft and hard are identified according to the leading particle transverse momentum. Picture from [ALICE2012b].	76
5.30	Mean transverse momentum as a function of multiplicity for isotropic and non-isotropic events selected with sphericity, thrust, directivity and Fox-Wolfram moments.	77
5.31	Pythia simulation of p_T spectra for uniform and jet-like events for all event shape observables. The cuts used are listed in Table 5.8.3.	78
5.32	ATLAS results on multi-jet cross-section. In the left panel, the ratio between the cross-section for n and $n+1$ jets is plotted. Figures from [ATLAS2011b].	79
5.33	Sphericity, thrust and $H_{2,3,4,6}$ for the 3 jets toy model.	80
5.34	Schematic view of the toy models used for event shape selection performance.	80
5.35	Sphericity, thrust, second and fourth Fox-Wolfram moments as a function of the angle between the two pairs of jets and the fraction of the momentum relative to the largest one. The results are obtained for the four jets toy model.	81
6.1	Tracking efficiency as a function of vertex position along the z axis (left panel). In the right panel the ratio of the efficiency for events with the vertex position near the center of the detector and events with the reconstructed vertex position between 9 and 10 cm from the center is plotted	86
6.2	Generated bin mixing for a given reconstructed multiplicity bin. The reconstructed multiplicity distribution is displayed in black. The red, green and blue lines represent three consecutive generated multiplicity bins. This example is shown for illustration purpose only. It does not represent an experimental case.	88
6.3	Global multiplicity bins - efficiency dependence.	89
6.4	Bin by bin ratio for the global multiplicity.	89
6.5	Minimum Bias efficiency for Pythia and Flat Pythia simulations.	90
6.6	Global multiplicity bin by bin ratio for the efficiency of Pythia and Flat Pythia runs.	91
6.7	Tracking efficiency for combined multiplicity bins for MB and HM trigger.	92
6.8	Tracking efficiency for minimum bias combined multiplicity bins (left panel). The ratio of the efficiency in each multiplicity bin and the minimum bias efficiency is plotted on the right panel.	92
6.9	Flat multiplicity distribution.	94
6.10	Efficiency in multiplicity bins for sphericity event selection. Isotropic events ($S > 0.8$) are plotted in blue. Green correspond to events with sphericity between 0.4 and 0.8. The efficiency for the pencil-like events with $S < 0.4$ is plotted in red.	94

6.11	Efficiency in multiplicity bins for sphericity cuts relative to the efficiency in the corresponding multiplicity bin. Red, green and blue correspond to low, medium and high sphericity values.	95
6.12	Efficiency in multiplicity bins for thrust cuts. Isotropic events ($T < 0.72$) are plotted in blue. Green correspond to events with thrust between 0.72 and 0.85. The efficiency for the pencil-like events with $T > 0.85$ is plotted in red.	95
6.13	Efficiency in multiplicity bins for thrust cuts relative to the efficiency in the corresponding multiplicity bin. Red, green and blue correspond to low, medium and high thrust values.	96
6.14	Efficiency in multiplicity bins for directivity cuts. The efficiency for isotropic events is plotted in red, the pencil-like events in blue, and events with medium directivity values in green.	96
6.15	Efficiency in multiplicity bins for directivity cuts relative to the efficiency in the corresponding multiplicity bin. Red, green and blue correspond to low, medium and high thrust values.	97
6.16	Efficiency for multiplicity bins using Fox-Wolfram cuts. In red, the azimuthally isotropic events are plotted. The efficiency for the rest of the events is plotted in green.	97
6.17	Efficiency for multiplicity bins using Fox-Wolfram cuts relative to the efficiency in the corresponding multiplicity bin. Isotropic events are plotted in red, while the rest of the events are plotted in green.	98
6.18	Feed-down contamination estimation in one p_T bin. The data are represented in green, the simulated primary particles in red, the weak decays and material in blue and black, while the total sum is displayed in magenta. The fit result is represented by the black line.	101
6.19	Multiplicity dependence of the feed-down correction.	101
6.20	The systematic effect for the multiplicity cut.	102
6.21	Systematic errors associated with parameter variation for each of the track cuts listed in the table 6.2. The variation is represented as a percentage of the minimum bias yield.	103
6.22	Fake tracks contamination for the charged particles.	104
6.23	Systematic error associated with the DCA correction. In the left plot, the initial evaluation shows large fluctuations at high p_T . The result of fluctuation removal using a quadratic fit is plotted in the right side.	105
6.24	Comparison of raw transverse momentum spectra for low (blue) and high (red) pileup runs. The ratio between the two spectra is given in the right side of the plot.	106
6.25	Total systematic uncertainty.	106
7.1	Minimum bias tracking efficiency (left panel) and feed down correction (right panel).	108
7.2	Transverse momentum spectra for minimum bias (left panel). Red points are the results of this analysis, while black points are obtained in another ALICE analysis. In the right panel, the ration between the two results is displayed.	108

7.3	Minimum bias efficiency for LHC10d and LHC10e periods (left panel) and ratio between them (right panel).	109
7.4	<i>Left panel:</i> transverse momentum spectra for the nine multiplicity bins listed in Table 6.1. Particle yield increases with the bin number. The lowest distribution (red) corresponds to bin 0 of minimum bias events. <i>Right panel:</i> ratio between the raw spectra in the same multiplicity range for the minimum bias and high multiplicity trigger.	110
7.5	Transverse momentum spectra in six minimum bias bins and three sphericity cuts.	111
7.6	Transverse momentum spectra in six minimum bias bins and three directivity cuts.	111
7.7	Transverse momentum spectra in six minimum bias bins and three thrust cuts.	112
7.8	Transverse momentum spectra in six minimum bias bins and Fox-Wolfram moments cuts corresponding to isotropic and non-isotropic events.	112
7.9	Transverse momentum spectra in three high multiplicity bins and three sphericity cuts.	113
7.10	Transverse momentum spectra in three high multiplicity bins and three directivity cuts.	113
7.11	Transverse momentum spectra in three high multiplicity bins and three thrust cuts.	113
7.12	Transverse momentum spectra in three high multiplicity bins and Fox-Wolfram moments cuts corresponding to isotropic and non-isotropic events.	114
7.13	Mean transverse momentum for all multiplicity bins. The results are obtained from the fitting functions (see the text). On the right panel, the mean p_T obtained with the Bylinkin-Rostovtsev parameterization with the associated systematic errors is plotted.	115
7.14	Fit quality for all six minimum bias and three high multiplicity bins.	116
7.15	Mean transverse momentum for minimum bias events. The red point represents the result obtained in this analysis.	117
7.16	Transverse momentum spectra for minimum bias and high multiplicity events in multiplicity bins and sphericity (left panel) and thrust (right panel) selection for uniform events.	118
7.17	Transverse momentum spectra for minimum bias and high multiplicity events in multiplicity bins and directivity (left panel) and Fox-Wolfram moments (right panel) event selection for uniform events.	119
7.18	Fit quality in multiplicity bins plotted as the ratio between the data and the fit function for the Fox-Wolfram selected events.	120
7.19	Freeze-out temperature vs. mean transverse velocity in Fox-Wolfram selected events (left panel). On the right panel, the results from balst wave fits of the Pb-Pb collisions at 2.76 TeV reported by ALICE collaboration [ALICE2013b].	121
A.1	ALICE coordinate system.	145

List of Tables

4.1	Summary of the 2010 LHC periods investigated in this analysis. . . .	32
5.1	The first eight Fox-Wolfram moments for different ideal event shape events.	47
5.2	Cut values for each of the event shape observables used.	54
5.3	The parameters used for p_T distribution random generation.	61
6.1	The correspondence between global and combined multiplicity bin limits.	93
6.2	Systematic errors associated to parameter variation.	103

Chapter 9

Acknowledgements

*“The mediocre teacher tells. The good teacher explains.
The superior teacher demonstrates.
The great teacher inspires.”
William Arthur Ward*

The work performed for this thesis was financially supported by the University of Bucharest through the ”Suport financiar pentru studii doctorale privind complexitatea din natură, mediu și societatea umană POSDRU 6/1.5/S/24” project, in the period 2008-2011.

I am thankful to my supervisor for giving me the opportunity to be part of the ALICE Collaboration. To all the people in the analysis task from within the NIHAM group and the people in the Spectra working group for all the useful suggestions. I thank Alex Bercuci for helping me with too many programming mistakes. Claudiu Schiaua was kind to enable the local fast and reliable preliminary tests of the analysis tasks presented in this thesis.

I cannot appreciate enough the support of my family and friends during this period of my life. Without them, I couldn't follow my passion.

I am thankful to many faculty professors. Here, I will mention especially Ion Lucian and Octavian Sima due to countless times when I solved a problem and I instantly remembered the moment they thought me what was necessary in order to solve that particular problem. Not only that the information I received from them was useful, their way of approaching problems was extremely helpful. Their example is a lesson that goes beyond what can be found in the textbooks.

If it were to select one person to thank, I would immediately choose my professor from high school - Tiberiu Țugui. He singlehandedly had the most important and decisive contribution to my scientific career and would also be the most disappointed of the outcome of this thesis. His efforts in teaching me mathematics and physics, amplified by the pedagogical talent gave me an example and a strong motivation. I am increasingly wondering on how he managed to have such a great impact on such a short time and I am constantly hoping that someday I will be able to help someone in the same manner he did with me.

I am grateful to all the persons who contributed to the development of the ALICE computational framework, unknowingly contributing to my thesis. I thank all the people involved in the analysis framework for making my life easier in what concerns the installation of AliRoot, leaving me more time available for the analysis.

This part of the acknowledgements is rather unusual. Throughout my scientific carrier I have used many softwares that made my life easy. Fedora, Ubuntu, Linux Mint, Root, SLURM, Kate, gedit, Gummi, TexMaker, Open/Libre Office. The Internet had become a handy source of information over the years. Too many times I have found, with the help of the almighty Google, great physics and computational documentation resources on the web, not only on the dedicated sites or Wikipedia, but also on Youtube.

I would also like to mention Anton Andronic for many short but extremely useful discussions. During this period, I had also a wonderful time while taking part to the TRD supermodule installations. For this I thank to Ken, Kai, Joerg and Dariusz.

Appendix A

ALICE coordinate system

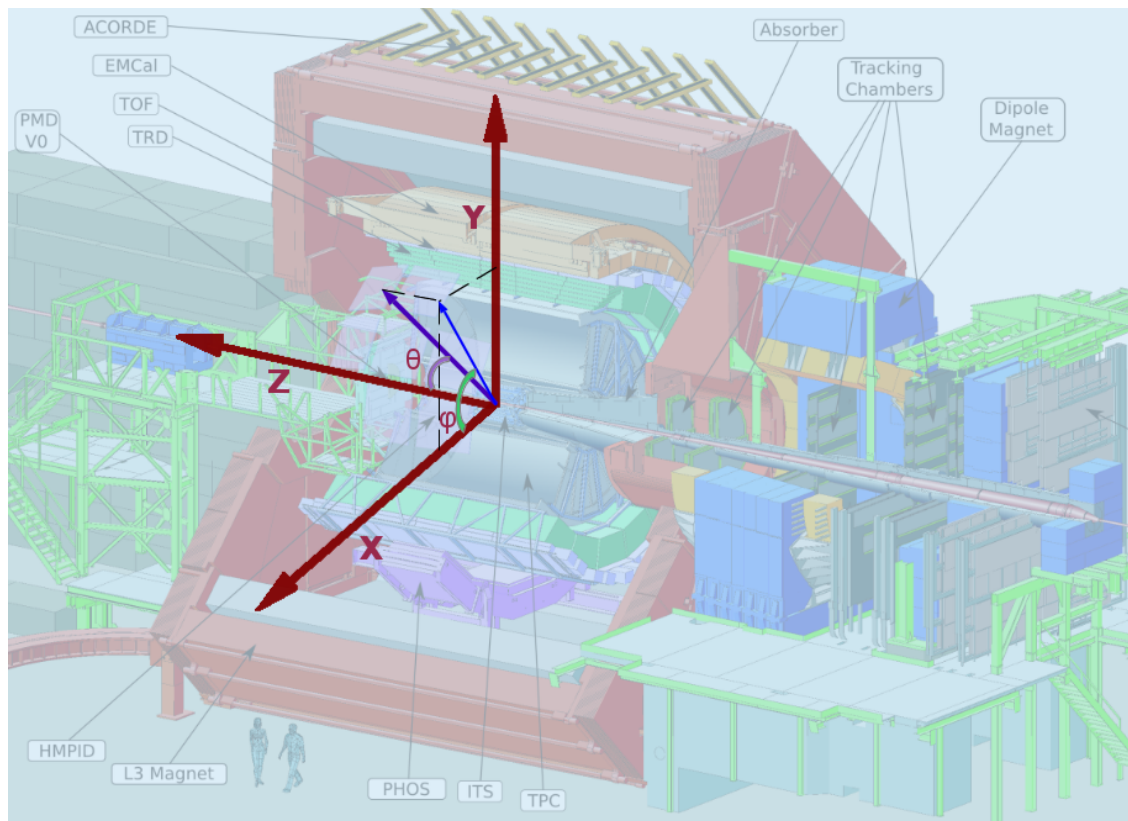


Figure A.1: ALICE coordinate system.